WAVELENGTH-DIVISION-MULTIPLEXED TRANSMISSION USING SEMICONDUCTOR OPTICAL AMPLIFIERS AND ELECTRONIC IMPAIRMENT COMPENSATION

by

XIAOXU LI
B.S. Peking University, CHINA, 1999
M.E. Peking University, CHINA, 2002

A dissertation submitted in partial fulfillment of requirements
for the degree of Doctor of Philosophy in Optics
in CREOL, The College of Optics and Photonics
at the University of Central Florida
Orlando, Florida

Fall Term
2009

Major Professor: Guifang Li

ABSTRACT

Over the last decade, rapid growth of broadband services necessitated research aimed at increasing transmission capacity in fiber-optic communication systems. Wavelength division multiplexing (WDM) technology has been widely used in fiber-optic systems to fully utilize fiber transmission bandwidth. Among optical amplifiers for WDM transmission, semiconductor optical amplifier (SOA) is a promising candidate, thanks to its broad bandwidth, compact size, and low cost.

In transmission systems using SOAs, due to their large noise figures, high signal launching powers are required to ensure reasonable optical signal-to-noise ratio of the received signals. Hence the SOAs are operated in the saturation region and the signals will suffer from SOA impairments including self-gain modulation, self-phase modulation, and inter-channel crosstalk effects such as cross-gain modulation, cross-phase modulation, and four-wave mixing in WDM. One possibility to circumvent these nonlinear impairments is to use constant-intensity modulation format in the 1310 nm window where dispersion is also negligible. In this dissertation, differential phase-shift keying (DPSK) WDM transmission in the 1310 nm window using SOAs was first considered to increase the capacity of existing telecommunication network. A WDM transmission of 4 × 10 Gbit/s DPSK signals over 540 km standard single mode fiber (SSMF) using cascaded SOAs was demonstrated in a recirculating loop.

In order to increase the transmission reach of such WDM systems, those SOA impairments must be compensated. To do so, an accurate model for quantum-dot (QD) SOA

must be established. In this dissertation, the QD-SOA was modeled with the assumption of overall charge neutrality. Static gain was calculated. Optical modulation response and nonlinear phase noise were studied semi-analytically based on small-signal analysis. The quantitative studies show that an ultrafast gain recovery time of ~0.1 ps can be achieved when QD-SOAs are under high current injection, which leads to high saturation output power. However more nonlinear phase noise is induced when the QD-SOAs are used in the transmission systems operating at 10 Gbit/s or 40 Gbit/s.

Electronic post-compensation for SOA impairments using coherent detection and digital signal processing (DSP) was investigated next in this dissertation. An on-off keying transmission over 100 km SSMF using three SOAs at 1.3 μm were demonstrated experimentally with direct detection and SOA impairment compensation. The data pattern effect of the signal was compensated effectively. Both optimum launching power and Q-factor were improved by 8 dB.

For advanced modulation formats involving phase modulation or in transmission windows with large dispersion, coherent detection must be used and fiber impairments in WDM systems need to be compensated as well. The proposed fiber impairment compensation is based on digital backward propagation. The corresponding DSP implementation was described and the required calculations as well as system latency were derived. Finally joint SOA and fiber impairment compensations were experimentally demonstrated for an amplitude and phase-shift keying transmission.

To my wife, my parents, and my family

ACKNOWLEDGMENTS

I would like to express my deepest appreciation to my advisor, Prof. Guifang Li, for his optimism and allowing me the freedom to explore things on my own. Without his guidance and persistent help, this dissertation would never have been completed.

I would also like to acknowledge my fellow group members, Xiaobo Xie, Eduardo Mateo, Fatih Yaman, Likai Zhu, and former group members, Cheolhwan Kim, Inwoong Kim, Yan Han, Zhihong Li, Xin Chen, Gilad Goldfarb, and Kevin Croussore, for their valuable suggestions, support and cooperation throughout the most unforgettable years of my life.

Thanks to my wife, Mengfei, who always stands behind me to support my every move and gave me her blessings to this undertaking.

TABLE OF CONTENTS

ABSTRACT iii

ACKNOWLEDGMENTS vi

TABLE OF CONTENTS vii

LIST OF FIGURES x

LIST OF TABLES xiv

1. INTRODUCTION 1

1.1 Increasing Communication Capacity 1

1.2 Increasing Communication Reach 4

1.3 Dissertation Outline 7

1.4 References 8

2. WDM TRANSMISSION IN 1310 NM WINDOW 13

2.1 Introduction 13

2.1.1 Differential Phase-Shift Keying 14

2.1.2 1.3 μm Semiconductor Optical Amplifier 16

2.2 Experiment 18

2.3 References 25

3. STUDY ON QUANTUM DOT-SEMICONDUCTOR OPTICAL AMPLIFIERS 28

3.1 Introduction 28

3.2 Theory of QD-SOA 29

3.2.1 Rate Equation Model for QD-SOA 29
3.2.2 Overall Charge Neutrality of QD-SOA 32
3.2.3 Steady-State Solution 33
3.2.4 Small-Signal Analysis 34
3.2.5 Nonlinear Phase Fluctuation (Noise) through Saturated QD-SOA 38
3.3 Simulations 39
3.3.1 Low Current Injection Level 41
3.3.2 High Current Injection Level 44
3.4 Discussions and Conclusions 48
3.5 References 50
4. ELECTRONIC POST-COMPENSATION OF SOA IMPAIRMENTS 53
4.1 Introduction 53
4.2 Principle of SOA Impairment Compensation 54
4.3 Impairment Compensation for Single SOA 58
4.4 Transmission Experiment of OOK Signal with SOA IC 64
4.5 Discussions and Conclusions 68
4.6 References 70
5. ELECTRONIC POST-COMPENSATION OF FIBER IMPARIMENTS 71
5.1 Introduction 71
5.2 Post-Compensation Based on Backward Propagation 72
5.3 DSP Implementation for Backward Propagation 75
5.3.1 Signal Up-sampling 75
5.3.2 Parallel Implementation for Backward Propagation 76

5.4 Simulations 82
5.5 Discussions and Conclusions 86
5.6 References 88
6. ELECTRONIC JOINT SOA AND FIBER IMPAIRMENT COMPENSATION 91
6.1 Introduction 91
6.2 Principle of Joint SOA and Fiber Impairment Compensation 92
6.3 Transmission Experiment of APSK signal with SOA and Fiber IC 94
7. FUTURE WORK 99
7.1 WDM Transmission with Joint SOA and Fiber IC 99
7.2 Parallel DSP Implementation of SOA IC 100

LIST OF FIGURES

Figure 1-1: (a) loss and (b) chromatic dispersion of SSMF (G.652) fiber 2

Figure 1-2: A typical point-to-point optical transmission system. OM: optical modulator; OA: optical amplifier; OR: optical receiver 4

Figure 2-1: Symbol constellation and electric field of OOK, (a) & (c); and DPSK, (b) & (d) 14

Figure 2-2: Schematic illustration of a binary DPSK system with DMZI 15

Figure 2-3: (a) ASE spectrum of 1.3 μm SOA; (b) gain and output power vs. input power 17

Figure 2-4: Experimental setup for WDM transmission in a re-circulating loop. PM: phase modulator; PC: polarization controller; SW: optical switch; BPF: band-pass filter; Attn.: Attenuator; DMZI: delayed Mach-Zehnder interferometer; CDR: clock and data recovery 18

Figure 2-5: Transmission spectrum of the inline optical filter (RBW=0.05nm) 20

Figure 2-6: Transmission spectrum of the demultiplexing filter (RBW=0.02nm) 20

Figure 2-7: Optical spectra of the WDM signals at the back-to-back and after transmissions of 60 km, 180 km, 360 km and 540 km (RBW= 0.05 nm) 21

Figure 2-8: The eye diagrams of the channel 1 signal at (a) back-to-back and after transmission of (b) 60 km, (c) 180 km, (d) 360 km and (e) 540 km 22

Figure 2-9: Q-factor of the channel 1 after transmission vs. launching power 24

Figure 3-1: Optical gain and output power of QD-SOAs as functions of input power with (a) charge neutrality for whole device; (b) charge neutrality in GS only 40

Figure 3-2: Electron occupation probability in GS (f_1), ES (f_2), CS (f_c) and hole occupation

probability in GS (h_1) (top); electron occupation probability in WL (f_w) (middle) and optical power (bottom) as a function of the normalized QD-SOA length at I = 50 mA and $\overline{P}(0)$ = 12.2 dBm 42

Figure 3-3: Optical modulation response of QD-SOA at I = 50 mA and (a) $\overline{P}(0)$ = 12.2 dBm; (b) $\overline{P}(L)$ = 13.4 dBm. The contributions to the total modulation response (solid line) due to WL, CS, ES and GS are represented by diamond, circle, triangle and square, respectively 43

Figure 3-4: Electron occupation probability in GS (f_1), ES (f_2), CS (f_c) and hole occupation probability in GS (h_1) (top); electron occupation probability in WL (f_w) (middle) and optical power (bottom) as a function of the normalized QD-SOA length at I = 2.5 A and $\overline{P}(0)$ = 10.2 dBm 45

Figure 3-5: Optical modulation response of QD-SOA at I = 2.5 A and (a) $\overline{P}(0)$ = 10.2 dBm; (b) $\overline{P}(L)$ = 27.2 dBm. The contributions to the total modulation response (solid line) due to WL, CS, ES and GS are represented by diamond, circle, triangle and square, respectively 46

Figure 3-6: Frequency response of the accumulated nonlinear phase fluctuation through the saturated QD-SOA. I=2.5A, $\overline{P}(0)$=10.2dBm and $\Delta\overline{P}(0)/\overline{P}(0)$ = 0.1 47

Figure 4-1: Diagram of a single SOA impairment compensation. Optical path: black line; Electrical path: blue line 54

Figure 4-2: Constellation of 16QAM signal a) before SOA; b) after SOA without IC; c) after SOA with IC 57

Figure 4-3: Experimental setup for a single SOA IC. VOA: variable optical attenuator; BPF: band-pass filter 58

Figure 4-4: Measured output power and SOA gain vs. input power 59

Figure 4-5: Q-factor of the NRZ signal after SOA IC vs. effective carrier lifetime 61

Figure 4-6: Optimized effective carrier lifetime for SOA IC vs. input power of the NRZ signal 61

Figure 4-7: Eye diagrams of the NRZ signal a) before SOA; b) after SOA without SOA IC; c) after SOA with SOA IC 62

Figure 4-8: Q-factor of the NRZ signal vs. input signal power 63

Figure 4-9: Experimental setup of 1310 nm transmission with SOA IC. VOA: variable optical attenuator; BPF: band-pass filter 64

Figure 4-10: Eye diagrams of a) the received NRZ signal and the signal after IC for b) one SOA; c) two SOAs; d) three SOAs 66

Figure 4-11: Q-factor and OSNR vs. launching power 67

Figure 5-1: WDM system with fiber dispersion and nonlinearity compensation using coherent detection and DSP. Optical path: black line; Electrical path: blue line; OM: optical modulator; EDFA: Erbium-doped fiber amplifier 73

Figure 5-2: Diagram of backward propagation for a multi-span fiber link. *L*: span number; *N*: step number per span 74

Figure 5-3: Block diagram of parallel implementation for backward propagation using DSP technique. The hollow arrows represent multiple inputs or outputs and the solid arrows represent single input or output 78

Figure 5-4: Block diagram of the sub-unit M_k in the *k*th branch in backward propagation. The inputs and outputs terminated by a circle may interface with other branches. The dashed lines only apply to some modules. $p \cdot T$ is the delay of FIR filter, and $q \cdot T$ is the delay of *inverse nonlinear operator 1* 79

Figure 5-5: Eye diagrams of the 5th WDM channel: (a) at back-to-back, (b) after 500 km

transmission over DSF without ENLC, (c) after 500 km transmission over DSF with ENLC, (d) after 800 km transmission over DSF with ENLC 84

Figure 5-6: Calculated Q-factor of the 5th WDM channel vs. the average launching power 85

Figure 6-1: Fiber-optic transmission using SOAs and electronic post-compensation of SOA and fiber impairments 92

Figure 6-2: Experimental setup of 4-APSK transmission with SOA and fiber impairments compensation. AWG: arbitrary waveform generator; VOA: variable optical attenuator; OBPF: optical band-pass filter; SSMF: standard single-mode fiber..... 94

Figure 6-3: Eye diagram of the 4-APSK signal a) at back-to-back; b) after SOA and 75 km SSMF without fiber and SOA ICs; after SOA and 75 km SSMF c) with only fiber IC; d) with only SOA IC; e) with both fiber and SOA ICs..... 96

Figure 6-4: a) Q-factor and b) optimized τ_c and α_H vs. input power to SOA..... 98

Figure 7-1: WDM transmission with joint SOA and fiber ICs. OM: optical modulator; Optical path: black line; Electrical path: blue line..... 99

Figure 7-2: The function diagram of the 4th order Runge-Kutta method for SOA IC 100

Figure 7-3: The function diagram of #1…#4 in Figure 7-2..... 100

LIST OF TABLES

Table 4-1: Parameters Values Used for Simulated SOA 56

1. INTRODUCTION

1.1 Increasing Communication Capacity

Over the last decade, the rapid growth in the demand of novel broadband services such as remote medical consultations and video on demand necessitated research aimed at increasing the transmission capacity in fiber-optic communication. Wavelength division multiplexing (WDM) technique, appeared in the 1970s [1], has been widely used in fiber-optic communication systems to expand the transmission bandwidth (capacity) by multiplexing signals on multiple optical carriers with different wavelengths (colors) in a single optical fiber [2-4]. The deployed WDM systems nowadays are making use of the third transmission window of silica fiber, e.g. standard single mode fiber (SSMF) or G.652 fiber around 1550 nm, where the fiber has minimum loss (shown in Figure 1-1(a)), and broadband optical amplifiers such as erbium doped fiber amplifier (EDFA) are available. The WDM or dense WDM (DWDM) transmission systems working in the 1550 nm window (C-band and L-band) have been standardized and commercially available in products such as Cisco ONS 15454 Multiservice Platform. Such systems can provide a wavelength (channel) count up to 112 with joint use of C-band and L-band through the same fiber when a channel spacing of 100 GHz (~0.8 nm) is used. The typical data rate carried by each wavelength is 10 Gbit/s or 40 Gbit/s by commonly used on-off keying (OOK) modulation

format. The transmission capacity through a single wavelength can be further increased by using higher spectral-efficiency modulation formats such as quadrature phase-shift keying (QPSK) and quadrature amplitude modulation (QAM) [5-7]. Such systems require more complicated modulation and detection techniques such as coherent detection, which introduce extra complexities and cost.

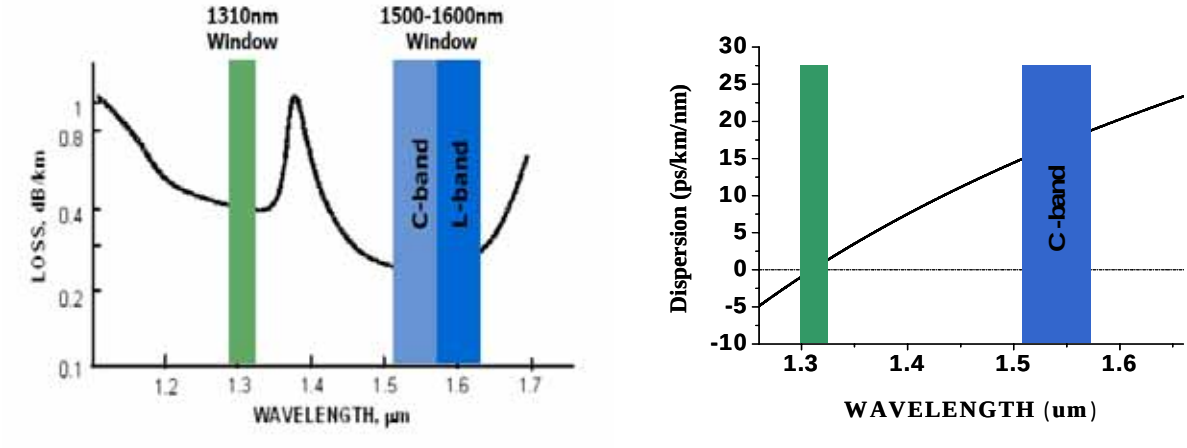

(a) (b)

Figure 1-1: (a) loss and (b) chromatic dispersion of SSMF (G.652) fiber

To make better use of the transmission bandwidth, optical transmissions in the second transmission window of the silica fiber around 1310 nm have been studied. The transmission capacity of the existing telecommunication network can be upgraded without the need of installing new types of fibers by utilizing this 1310 nm transmission window. At 1310 nm, the chromatic dispersion of SSMF is nearly zero, hence the dispersion-limited transmission distance can be 10 times greater than that in the 1550 nm window (shown in Figure 1-1(b)). However, the

SSMF has higher attenuation of ~0.4 dB/km at 1310 nm compared with 1550 nm window, as shown in Figure 1-1(a). Moreover, EDFA does not work in that window. In order to compensate the fiber losses and thus increase the transmission distance, optical amplifiers are necessary. Among the optical amplifiers available in the 1310 nm window [8-11], semiconductor optical amplifier (SOA) is the most promising candidate because of its mature technology, compact size, and low cost.

Earlier 1310 nm transmission experiments were primarily demonstrated using OOK in non-return-to-zero (NRZ) and return-to-zero (RZ) systems operating at 10 Gbit/s [12-14]. In 1996 [12], a 10 Gbit/s RZ transmission at 1309 nm over a straight 420 km SSMF link was demonstrated using 12 cascaded multiple quantum well SOAs (MQW-SOAs) at intervals of ~38 km, achieving a transmission capacity of 4200 Gbit · km/s. The first field trial experiment of 10 Gbit/s RZ transmission over 210 km SSMF was demonstrated at 1314 nm with in-line optical amplification provided by SOAs [13]. To further increase the transmission capacity, 4 × 10 Gbit/s NRZ transmission in the 1310 nm window over 80 km SSMF with channel spacing of 300 GHz was demonstrated in [14] to study the feasibility of SOA cascade for WDM applications. In these OOK transmission systems using cascaded SOAs, the system performance was mainly limited by the accumulated amplified spontaneous emission (ASE) noise, the signal pattern effect, and the associated spectral walk-off [15,16]. In WDM applications, system performance such as channel spacing is also limited by the four-wave mixing (FWM) effect of the WDM signals in SSMF and saturated SOAs. Nevertheless, by using differential phase-shift keying

(DPSK) modulation format, some harmful effects such as data pattern effect and inter-channel crosstalk could be mitigated because the phase-modulated signals have equal amount of energy in every bit slot, i.e., constant intensity profile [17]. In this dissertation, WDM transmission in the 1310 nm transmission window using DPSK format and SOAs will be studied to investigate the feasibility of increasing communication capacity.

1.2 Increasing Communication Reach

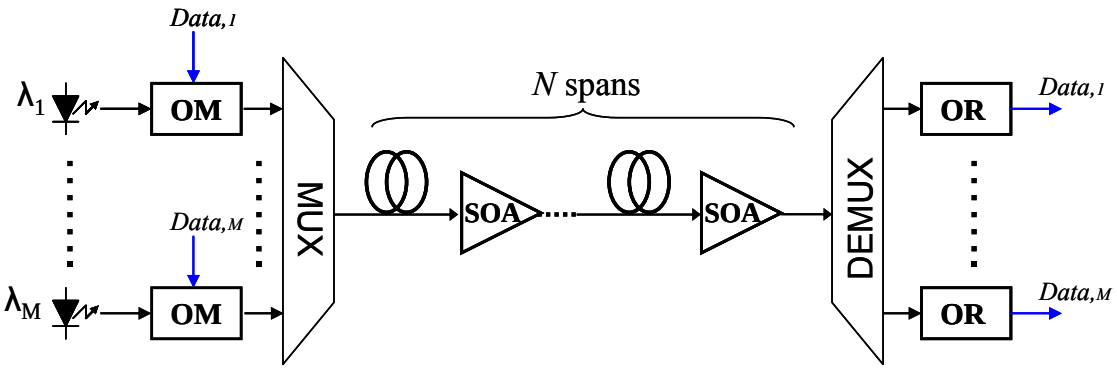

Figure 1-2: A long haul WDM transmission system using SOAs. OM: optical modulator; SOA: semiconductor optical amplifier; OR: optical receiver

The pursuit for further communication reach becomes the next logical step after the communication capacity has been accommodated. A long-haul WDM transmission system consists of laser sources, optical modulators, optical MUX/DEMUX, optical fibers, optical amplifiers and optical receivers, as shown in Figure 1-2. When an optical signal (channel) travels in such a system, optical signal-to-noise ratio (OSNR) of the signal is degraded by the

accumulated ASE noise of the optical amplifiers and thus transmission reach is limited. To achieve a higher OSNR for longer transmission reach, higher signal (launching) power is desired. However SOAs will be operated in the saturation region and the signal will suffer from SOA nonlinearities including data pattern effect, self-gain modulation (SGM) effect, self-phase modulation (SPM) effect, and inter-channel crosstalk effects such as cross-gain modulation (XGM), cross-phase modulation (XPM) and FWM. In addition, the signal with high power will also be distorted by fiber dispersion and fiber Kerr nonlinearity such as SPM effect, and inter-channel crosstalk effects such as XPM and FWM [18-20]. In order to maximize the SNR of the received signal while maintaining system performance, both SOA and fiber impairments must be compensated.

Fiber impairment compensations have been widely studied in optical domain. Dispersion compensating fiber (DCF) is commonly used to compensate chromatic dispersion [21]. However it will introduce extra loss and nonlinearity. WDM systems suffer from both intra- and inter-channel nonlinearities such as XPM and FWM. These effects can be suppressed using dispersion management [22-23]. A few optical nonlinearity compensation schemes have been demonstrated such as lumped compensation of SPM [24] and optical phase conjugation for the compensation of both chromatic dispersion and Kerr nonlinearity in fibers [25].

Fiber impairment compensations in electrical domain have received significant attention in recent years due to the advanced digital signal processing (DSP) technique. Several electronic pre-compensation schemes have been demonstrated to compensate chromatic dispersion or/and

nonlinearity in single-channel and WDM system [26-29]. These schemes pre-distorted the transmitted signals using arbitrary waveform generators. Pre-distortion was calculated using optical phase conjugation or backward propagation, i.e., the signal was distorted by virtual fiber while compensated through the real fiber transmission. Electronic post-compensation using coherent detection and DSP has been shown to be effective in chromatic dispersion compensation [30] and intra-channel nonlinearity compensation [31]. Post-compensation offers great flexibility since adaptive compensation can be incorporated in this scheme. However, there have been no reports to date on integrated post-compensation of chromatic dispersion, intra- and inter-channel nonlinearities in WDM transmission.

Compared to various fiber impairment compensation schemes, no effective SOA impairment compensation scheme has been reported to date. The conventional methods have been focused on suppressing, instead of compensating, the SOA nonlinearities. Data pattern effect removal techniques have been demonstrated for SOA-based wavelength conversion [32-34]. Those techniques require an extra optical band-pass filter and the center wavelength of the filter needs to be tuned according to the signal power into the SOAs. Pattern-effect free amplifications have also been demonstrated using novel quantum-dot SOAs (QD-SOAs) due to their ultrafast gain recovery time and high saturation output power [35-38]. However the QD-SOAs are highly polarization-sensitive and thus not feasible for real optical transmission. Recently maximum likelihood sequence estimation (*MLSE*) receiver has been employed to increase signal tolerance to SOA nonlinearities [39, 40]. The *MLSE* method requires a Viterbi

decoding procedure whose computation complexity increase exponentially with the accumulated SOA impairments and not practical for high spectral efficiency modulation format such as QAM.

1.3 Dissertation Outline

This dissertation is outlined as follows. In Chapter 2, WDM transmission of DPSK signals is demonstrated in the 1310 nm transmission window using SOAs and a re-circulating loop to investigate the feasibility of increasing the transmission capacity of the existing telecommunication network. In Chapter 3, QD-SOA is studied theoretically to investigate its possible applications for optical transmission. A modified rate equation model is presented, taking into account the overall charge neutrality of the device. Both static and dynamic characteristics of QD-SOAs are simulated. Chapter 4 presents an electronic post-compensation scheme for SOA impairments. Transmission experiment of OOK signal with SOA impairment compensation is demonstrated. In Chapter 5, an electronic post-compensation scheme is proposed to compensate the fiber dispersion and nonlinearity. A DWDM transmission system with fiber impairment compensation is simulated. In Chapter 6, an amplitude and phase-shift keying (APSK) transmission with joint fiber and SOA impairment compensations is demonstrated. In Chapter 7, the future work is depicted.

1.4 References

[1] O. E. Delange, “Wideband optical communication systems, Part 11-Frequency division multiplexing,” *hoc. IEEE*, vol.58, pp.1683, 1970.

[2] H. M. Ishio and K. J. Nosu, “Review and status of wavelength-division-multiplexing technology and its application,” *J. Lightwave Technol.*, vol.2, pp.448-463, 1984.

[3] M. X. Ma *et al.*,“240-km repeater spacing in a 5280-km WDM system experiment using 8×2.5 Gb/s NRZ transmission,” *IEEE Photon. Technol. Lett.*, vol.10, pp.893-895, 1998.

[4] M. I. Hayee and A. E. Willner, “NRZ versus RZ in 10-40-Gb/s dispersion-managed WDM transmission systems,” *IEEE Photon. Technol. Lett.*, vol.11, pp.991-993, 1999.

[5] K. Kikuchi *et al.*, “Unrepeated 210-km transmission with coherent detection and digital signal processing of 20-Gb/s QPSK signal,” *OFC’2005*, paper OTuL4, 2005.

[6] T. Pfau *et al.*, “First real-time data recovery for synchronous QPSK transmission with standard DFB lasers,” *IEEE Photon. Technol. Lett.*, vol.18, pp.1907-1909, 2006.

[7] J. Hongo *et al.*, “1-Gsymbol/s 64-QAM Coherent Optical Transmission Over 150 km,” *IEEE Photon. Technol. Lett.*, vol.19, pp.638-640, 2007.

[8] T. Sakamoto *et al.*, “1300 nm-band WDM transmission employing PDFAs,” *OATA’1999*, paper SN2, pp.250-253, 1999.

[9] T. N. Nielson *et al.*, “10-Gbit/s repeaterless transmission at 1.3μm with 55.1-dB power budget using Raman post- and preamplifier,” *OFC’1998*, paper TuI4, pp.52-53, 1998.

[10]L. F. Tiemeijer *et al.*, "Progress in 1.3 μm polarization insensitive multiple quantum well laser amplifers," *OATA'1994*, pp.34-36, 1994.

[11]L. F. Tiemeiier *et al.*, "27-dB gain unidirectional 1300-nm polarization-insensitive multiple quantum well laser amplifier module," *IEEE Photon. Technol. Lett.*, vol.6, pp.1430-1432, 1994.

[12]P. I. Kuindersma *et al.*, "10 Gbit/s RZ transmission at 1309 nm over 420 km using a chain of multiple quantum well semiconductor optical amplifier modules at 38 km intervals," *ECOC'1996*, paper TuD.2.1, pp.165-168, 1996.

[13]J. J. E. Reid *et al.*, "High bitrate 1.3 μm optical transmission in the field using cascaded semiconductor optical amplifiers," *ECOC'1997*, pp.83-86, 1997.

[14]J. G. L. Jennen *et al.*, "4 × 10 Gbit/s NRZ transmission over 80 km of standard single mode fiber using semiconductor optical amplifiers," *ECOC'1998*, pp.235-236, 1998.

[15]M. Settembre *et al.*, "Evaluation of 10 Gbit/s@1.3 μm signal transmission in fiber link using semiconductor optical amplifiers," *ECOC'1997*, pp.75-78, 1997.

[16]A. Shipulin *et al.*, "Spectral walk-off in high-bit-rate standard fiber transmission systems with semiconductor optical amplifiers," *OFC'1998*, paper Th06, pp.323-324, 1998.

[17]C. Xu *et al.*, "Differential phase-shift keying for high spectral efficiency optical transmissions," *IEEE J. Sel. Topics Quantum Electron.*, vol.10, pp.281-293, 2004.

[18]R. H. Stolen and C. Lin, "Self-phase modulation in silica optical fibers," *Phys. Rev. A*, vol.17, pp.1448-1451, 1978.

[19]K. Inoue, “Four-wave mixing in an optical fiber in the zero-dispersion wavelength region,” *IEEE J. Lightwave Technol.*, vol.10, pp.1553-1561, 1992.

[20]S. Ten *et al.*, “Comparison of four-wave mixing and cross phase modulation penalties in dense WDM systems,” *OFC’1999*, paper ThC4, pp.43-45, 1999.

[21]A. M. Vengsarkar and W. A. Reed, “Dispersion-compensating single mode fiber: Efficient designs for first- and second-order compensation,” *Opt. Lett.*, vol.18, pp.924-926, 1993.

[22]C. Kurtzke, “Suppression of fiber nonlinearities by appropriate dispersion management,” *IEEE Photon. Technol. Lett.*, vol.5, pp.1250-1253, 1993.

[23]K. Nakajima *et al.*, “Design of dispersion managed fiber and its FWM suppression performance,” *OFC’1999,* paper ThG3, 1999.

[24]X. Liu *et al.*, “Improving transmission performance in differential phase-shift-keyed systems by use of lumped nonlinear phase-shift compensation,” *Opt. Lett.*, vol.27, pp.1616-1618, 2002.

[25]S. Watanabe and M. Shirasaki, “Exact compensation for both chromatic dispersion and Kerr effect in a transmission fiber using optical phase conjugation,” *IEEE J. Lightwave Technol.*, vol.14, pp.243-248, 1996.

[26]R. I. Killey *et al.*, “Electronic dispersion compensation by signal predistortion using digital processing and a dual-drive Mach-Zehnder modulator,” *IEEE Photon. Technol. Lett.*, vol.17, pp.714-716, 2005 .

[27]S. L. Woodward *et al.*, “Demonstration of an electronic dispersion compensation in a 100-km 10-Gb/s ring network,” *IEEE Photon. Technol. Lett.*, vol.15, pp.867-869, 2003.

[28]K. Roberts *et al.*, “Electronic precompensation of optical nonlinearity,” *IEEE Photon. Technol. Lett.*, vol.18, pp.403-405, 2006.

[29]E. Yamazaki *et al.*, “Compensation of interchannel crosstalk induced by optical fiber nonlinearity in carrier phase-locked WDM system,” *IEEE Photon. Technol. Lett.*, vol.19, pp.9-11, 2007.

[30]M. G. Taylor, “Coherent detection method using DSP for demodulation of signal and subsequent equalization of propagation impairments,” *IEEE Photon. Technol. Lett.*, vol.16, pp.674-676, 2004.

[31]K. Kikuchi, “Phase-diversity homodyne detection of multilevel optical modulation with digital carrier phase estimation,” *IEEE J. Sel. Topics Quantum Electron.*, vol.12, pp.563-570, 2006.

[32]Y. Liu *et al.*, “Error-free all-optical wavelength conversion at 160 Gb/s using a semiconductor optical amplifier and an optical bandpass filter,” *IEEE J. Lightwave Technol.*, vol.24, pp.230-236, 2006.

[33]J. Leuthold *et al.*, “All-optical wavelength conversion using a pulse reformatting optical filter,” *IEEE J. Lightwave Technol.*, vol.22, pp.186-192, 2004.

[34]J. Wang *et al.*, “Pattern effect removal technique for semiconductor-optical-amplifier-based wavelength conversion,” *IEEE Photon. Technol. Lett.*, vol.19, pp.1955-1957, 2007.

[35]A. V. Uskov *et al.*, "Theory of pulse-train amplification without pattern effects in quantum-dot semiconductor optical amplifiers," *IEEE J. Quantum Electron.*, vol. 40, pp.306-320, 2004.

[36]T. Akiyama *et al.*, "Pattern-effect-free semiconductor optical amplifier achieved using quantum dots," *Electron. Lett.*, vol.38, pp.1139-1140, 2002.

[37]M. Sugawara *et al.*, "Quantum-dot semiconductor optical amplifiers for high-bit-rate signal processing up to 160 Gb/s and a new scheme of 3R regenerators," *Meas. Sci. Technol.*, vol. 13, pp.1683-1691, 2002.

[38]T. Akiyama *et al.*, "An ultrawide-band (120 nm) semiconductor optical amplifier having an extremely-high penalty free output power of 23 dBm realized with quantum-dot active layers," *OFC'2004,* paper PDP12, 2004.

[39]J. D. Downie and J. Hurley, "Performance of an MLSE-EDC receiver with SOA-induced nonlinear impairments," *IEEE Photon. Technol. Lett.*, vol.20, pp.1326-1328, 2008.

[40]J. D. Downie *et al.*, "10.7 Gb/s uncompensated transmission over a 470 km hybrid fiber link with in-lin SOAs using MLSE and duobinary signals," *Opt. Exp.*, vol.16, pp.15759-15764, 2008.

2. WDM TRANSMISSION IN 1310 NM WINDOW

2.1 Introduction

Utilizing the 1310 nm transmission window, the transmission capacity of the existing telecommunication network can be upgraded using the installed SSMF [1]. Among the optical amplifiers available in 1310 nm window such as praseodymium-doped fiber amplifiers (PDFAs), Raman amplifiers, etc.[2-4], the SOA is the most promising candidate thanks to its mature technology, low cost, and compact size. Earlier 1310 nm transmission experiments were primarily demonstrated in NRZ- and RZ-OOK systems operating at 10 Gbit/s [5-7]. The performance in such systems is mainly limited by the accumulated ASE noise as well as data pattern effects and inter-channel crosstalk from SOAs nonlinearity. However, using DPSK as the modulation format not only offers a 3-dB improvement in receiver sensitivity by balanced detection but also mitigates harmful effects such as data pattern effects and inter-channel crosstalk since the phase-modulated signal has equal amount of energy in every bit slot, i.e., constant intensity profile [8]. A single channel transmission of 10 Gbit/s NRZ-DPSK was demonstrated at 1310 nm over SSMF using a re-circulating loop and cascaded SOAs with an error-free transmission up to 500 km [9]. In this chapter, a WDM transmission of NRZ-DPSK signals in the 1310 nm transmission window is demonstrated for the first time, to our knowledge,

using cascaded SOAs and a re-circulating loop.

2.1.1 Differential Phase-Shift Keying

The studies on the phase-shift keying (PSK) for optical coherent communications can date back to around 1990, aiming to obtain good receiver sensitivity [10-11]. However, the interests in PSK receded between mid-1990s and 2001 due to two factors: 1) the difficulty in implementing the precise alignment of the transmitter and demodulator center frequencies; 2) the advent and deployment of EDFA, which shifts the research and development focus to amplitude-shift keying (ASK), especially OOK. With the pursuit of high channel data rate, high system spectral efficiency and long system reach, PSK regains researchers' interests and becomes popular since 2002 because of its better receiver sensitivity and tolerance to the fiber nonlinearity in long haul optical transmission systems [12-14].

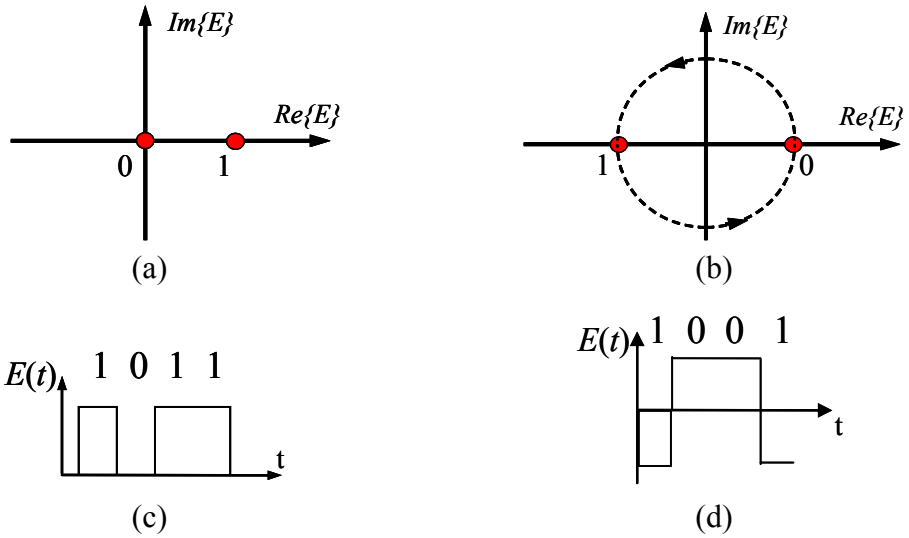

Figure 2-1: Symbol constellation and electric field of OOK, (a) & (c); and DPSK, (b) & (d)

Compared to the coherent detection of PSK signal, the direct detection of DPSK with a delayed Mach-Zehnder interferometer (DMZI) is more practical to implement. DPSK is the modulation technique that codes information by using the phase difference between two neighboring symbols [8]. Figure 2-1(a) and 2-1(b) represent the symbol constellations of conventional OOK and DPSK formats, respectively. In contrast to conventional OOK (shown in Figure 2-1(a)), bit 0 in DPSK modulation leaves the signal phase alone while bit 1 introduces a π-phase change to the signal. Consequently the bit set of {0, 1} is mapped into the symbol set of $\{e^{j0}, e^{j\pi}\}$, i.e.{1, -1}, as shown in Figure 2-1(b). The electric field amplitudes of NRZ-OOK and NRZ-DPSK signals with certain pattern are shown in Figure 2-1 (c) and 2-1(d), respectively. Compared with OOK signal, DPSK signal has a constant or periodic intensity profile, which leads to many advantages over OOK signal such as better nonlinear tolerance.

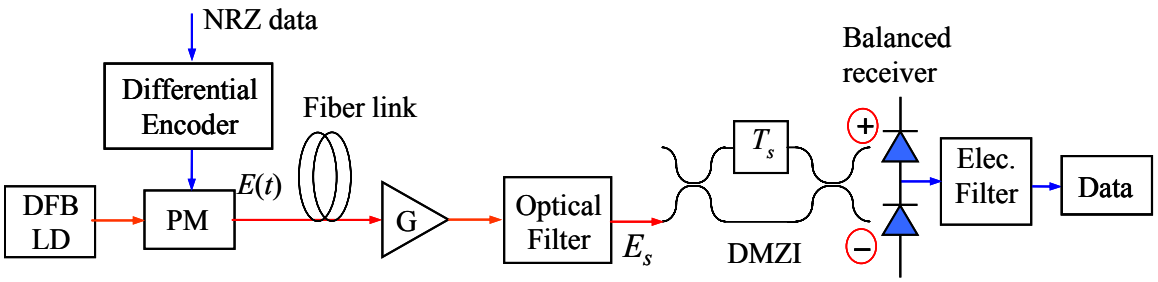

Figure 2-2: Schematic illustration of a binary DPSK system with DMZI

Figure 2-2 illustrates a generic binary DPSK system. Compared with the OOK system, a MZI with 1-bit delay is employed for direct detection and converts the incoming phase-modulated signal into intensity-modulated signals. The signals at the two outputs of DMZI,

complementary in intensity, are differentially detected by balanced photodiodes and the bit error rate (BER) is eventually measured on the regenerated data. Aided by DMZI and balanced detection, DPSK requires approximately 3-dB lower optical signal-to-noise ratio (OSNR) than OOK for the same BER, i.e., DPSK has 3-dB improvement in receiver sensitivity compared with OOK.

2.1.2 1.3 μm Semiconductor Optical Amplifier

To utilize the presently installed SSMF for 10 Gbit/s local area network (LAN) or metro area network (MAN) applications in the second optical window, 1.3 μm SOAs have been studied extensively [15-17]. Other than using these SOAs as in-line amplifiers to compensate the fiber loss [18, 19], they can be employed as power boosters to increase the transmitter output power and optical preamplifiers to improve the receiver sensitivities as well [20-22].

Figure 2-3(a) shows the measured ASE spectra of a commercial bulk SOA operating around 1.3 μm at different driving currents. This SOA acts as the optical preamplifier in the following experiments. At the current of 140 mA, the SOA has a gain peak around 1290 nm and 3-dB gain bandwidth of 46 nm. This broad gain bandwidth is a major advantage of SOA and favorable for WDM applications. The measured gain ripple around 1310nm is less than 0.2 dB, which is from the imperfect anti-reflection coatings on both ends of the SOA. Figure 2-3(b) represents the dependence of SOA gain and output power on the input power of a continuous wave (CW) signal centered around 1310 nm. At the driving current of 140 mA, the SOA

provides a fiber-to-fiber gain up to 24 dB and 3-dB saturation output power of 10 dBm. Moreover the SOA shows a polarization dependent gain less than 0.8 dB, which is desirable in the practical systems. It is also noted that this SOA has a noise figure of less than 6 dB, which is comparable with the widely used EDFAs working in the 1550 nm window.

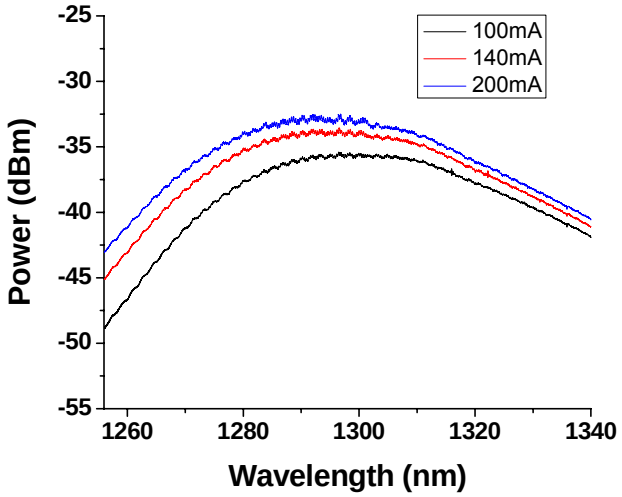

(a)

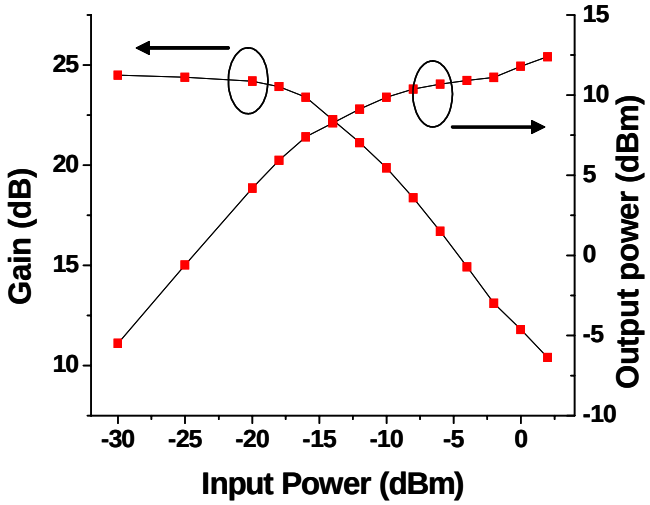

(b)

Figure 2-3: (a) ASE spectrum of 1.3 μm SOA; (b) gain and output power vs. input power

2.2 Experiment

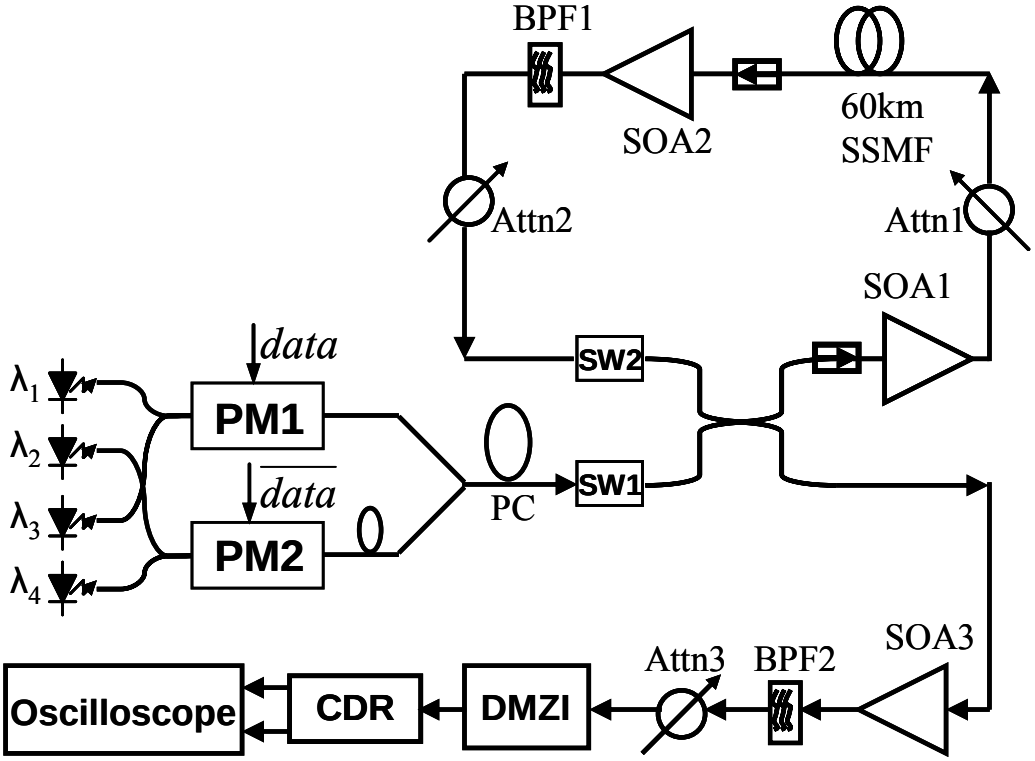

Figure 2-4: Experimental setup for WDM transmission in a re-circulating loop. PM: phase modulator; PC: polarization controller; SW: optical switch; BPF: band-pass filter; Attn.: Attenuator; DMZI: delayed Mach-Zehnder interferometer; CDR: clock and data recovery

Figure 2-4 shows the experimental setup for the 1310 nm transmission of 4 × 10 Gbit/s NRZ-DPSK signals over SSMF using SOAs and re-circulating loop. Four 1310 nm DFB lasers comprised the sources for channels 1, 2, 3 and 4, respectively. Channel 1&3 and channel 2&4 were combined by two 3-dB couplers and then input to two phase modulators (PM1 and PM2), respectively. PM1 and PM2 were driven by 10 Gbit/s NRZ $data$ and $\overline{data}$, respectively, and an optical delay line was placed after PM2 for decorrelation. The two branches of signals were

combined by another 3-dB coupler to produce the WDM signals. A re-circulating loop was built for long distance transmission. The loop consists of two SOAs and one SSMF spool of 60 km. The SOA1 worked as a power booster when the WDM signals were filled into the loop and a power amplifier to compensate the extra loop loss other than the SSMF, which were mainly from the BPF1, Attn2, SW2 and the 3-dB coupler when the WDM signals were transmitted in the loop. The Attn1 was used to control the launching power into the SSMF. The 60 km SSMF has negligible chromatic dispersion and ~22 dB loss at 1310 nm. The SOA2 worked as an inline amplifier to compensate the fiber loss. An optical band-pass filter (BPF1) was placed after the SOA2 to remove the ASE noise outside the WDM signals bandwidth. The optical filter had a low insertion loss of 1 dB and flat transmission of 9 nm around the center wavelength, as shown in Figure 2-5. The Attn2 was used to equalize the loop gain and loss. It is noted that an optical isolator was used before each SOA to assure the unidirectional transmission in the loop. At the receiver side, an optical preamplifier (SOA3) was used before demodulation and photo-detection. At the injection current of 140 mA, it provides a small signal gain of 24 dB and a saturation output power of 10 dBm. Another optical band-pass filter (BPF2) with 3-dB bandwidth of 0.2 nm was used to select the measured channel from the WDM signals. The measured transmission spectrum is shown in Figure 2-6. A variable optical attenuator was then used to control the received optical power. A 1-bit DMZI was employed to convert the phase modulation to amplitude modulation. Finally a 10G CDR module was used to recover clock for the sampling oscilloscope. The signal waveforms were observed and Q-factors were calculated.

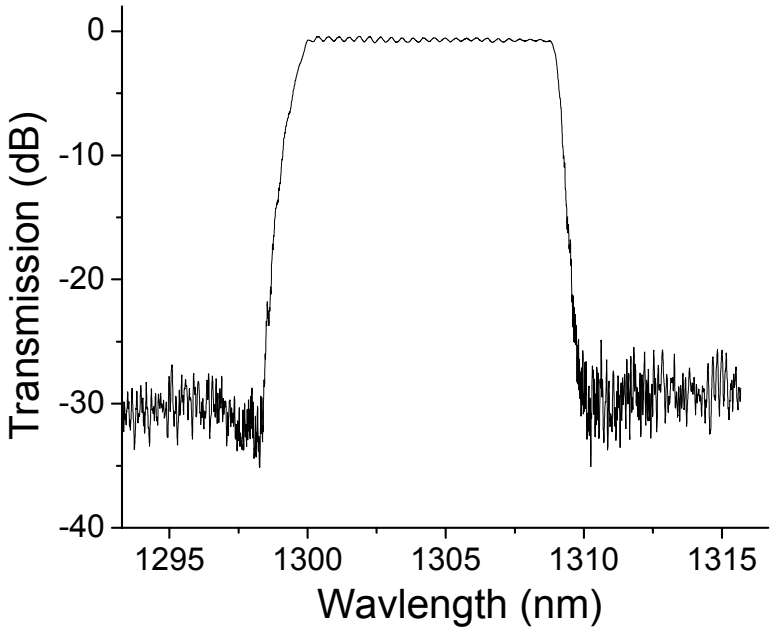

Figure 2-5: Transmission spectrum of the inline optical filter (RBW=0.05nm)

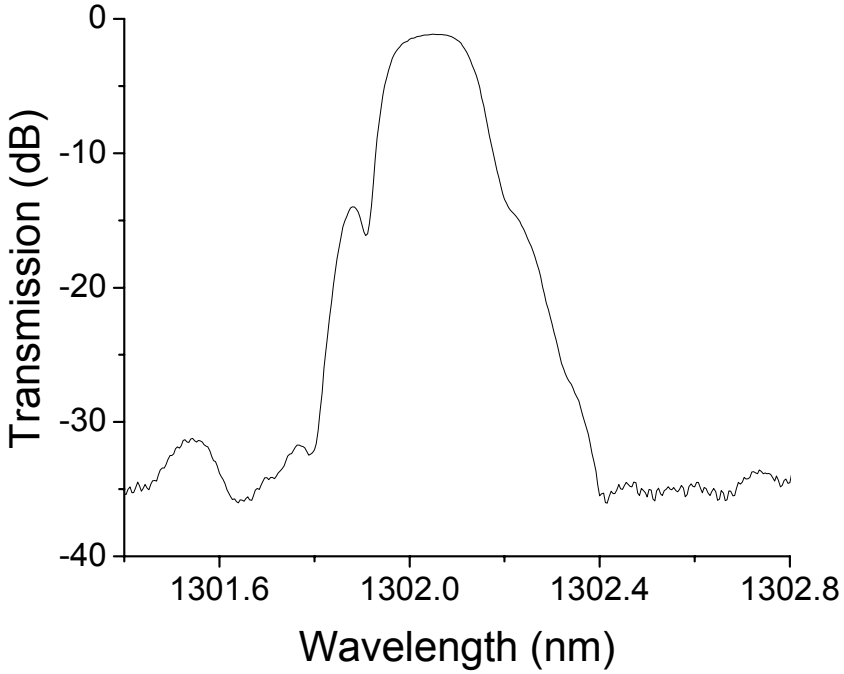

Figure 2-6: Transmission spectrum of the demultiplexing filter (RBW=0.02nm)

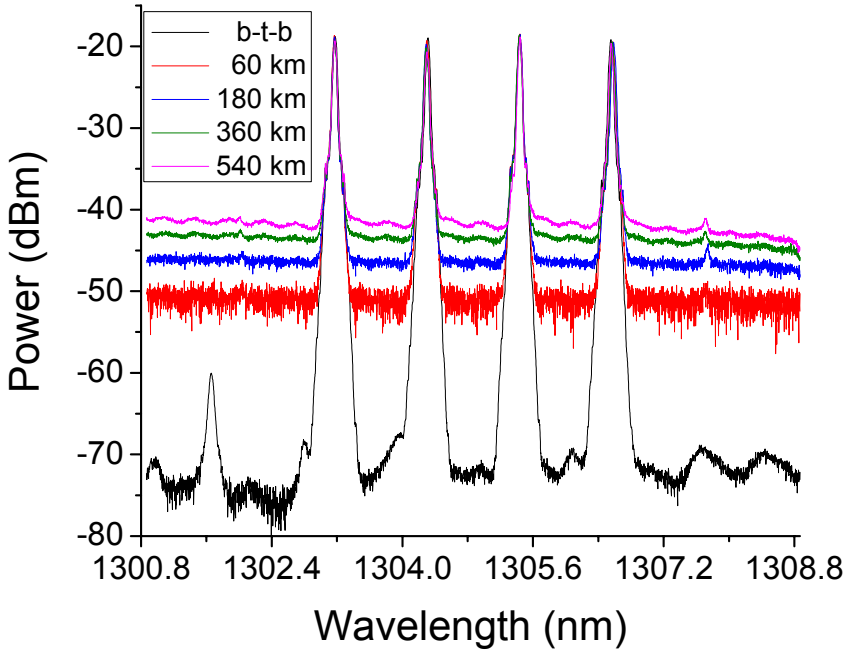

Figure 2-7: Optical spectra of the WDM signals at the back-to-back and after transmissions of 60 km, 180 km, 360 km and 540 km (RBW= 0.05 nm)

The optical spectra of the WDM signals at back-to-back and after transmission of different loops (distance) were shown in Figure 2-7. The total launching power into the SSMF was 9 dBm or 3 dBm/channel. The four channels had an equal channel spacing of 1.14 nm, i.e. 200 GHz. In the spectrum at back-to-back, shown in black line, the small peak to the left of channel 1 was due to the imperfect side mode suppression of channel 1. In the spectra after each transmission span, the background noise level was increased due to the accumulated ASE noise of SOAs. Compared to the straight-line transmission, the OSNR of the WDM signals degraded more rapidly in the re-circulating loop experiment because of the higher loop loss which was not only from the 60 km SSMF but also from other loop components such as optical switch, 3-dB

coupler, etc. It is noted that no significant four-wave mixing (FWM) was observed due to the large channel spacing and polarization scrambling among the WDM signals during the loop transmissions.

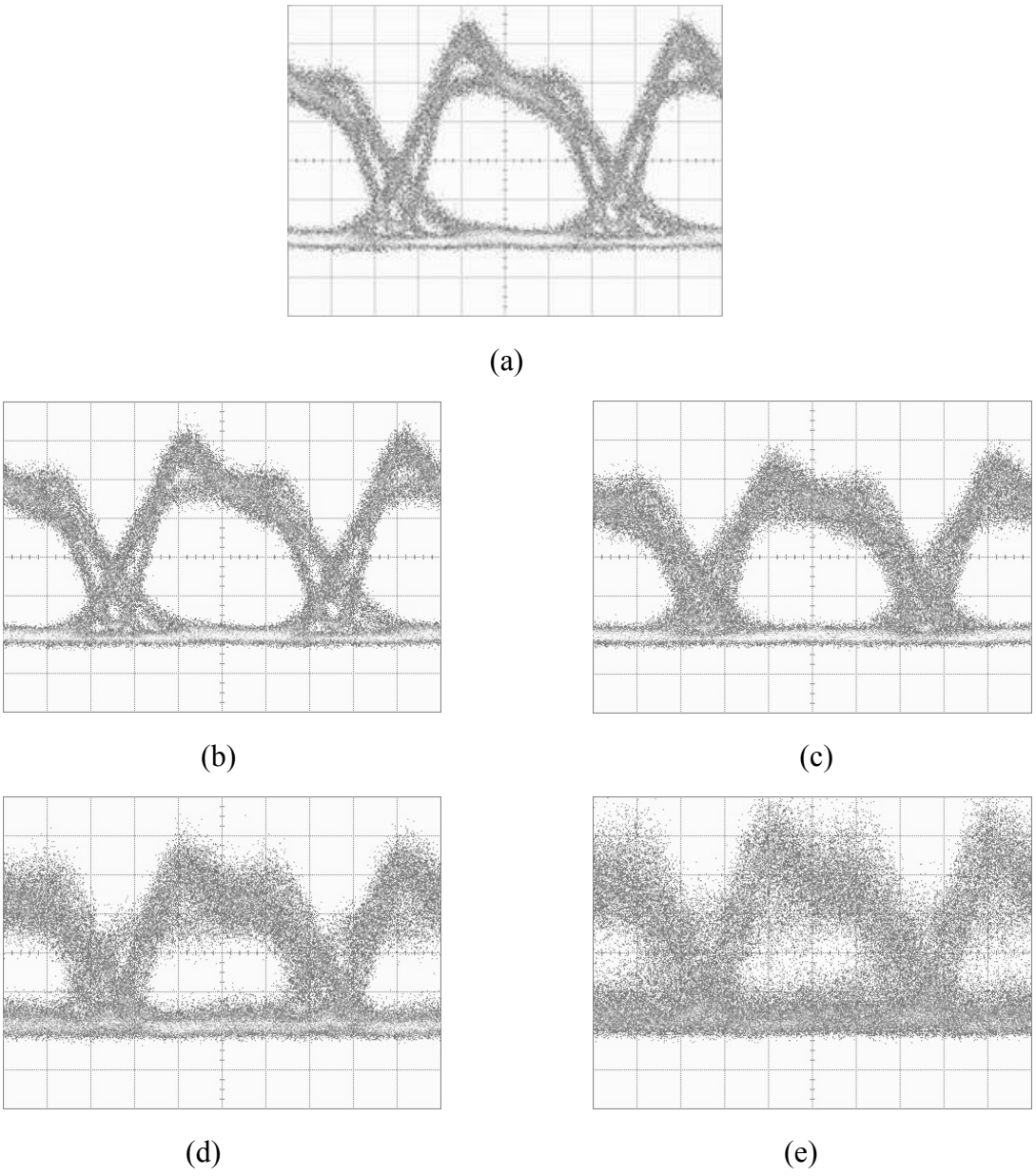

(a)

(b)

(c)

(d)

(e)

Figure 2-8: The eye diagrams of the channel 1 signal at (a) back-to-back and after transmission of (b) 60 km, (c) 180 km, (d) 360 km and (e) 540 km

Figure 2-8 shows the eye diagrams of the channel 1 signal at the back-to-back and after transmission of 60 km, 180 km, 360 km and 540 km, respectively. The launching power was 3 dBm/channel. At the back-to-back, the signal was distorted from the ideal NRZ format, seen in Figure 2-8(a), because the demultilpexing filter had a narrow and asymmetric transmission spectrum (Figure 2-6). The calculated Q-factor was 12.4. After transmission of 60 km SSMF, the signal had almost identical eye diagram to the back-to-back, shown in Figure 2-8(b). The calculated Q-factor was 11.4. The accumulated ASE became apparent in the signal after 180 km transmission, shown in Figure 2-8(c), and the calculated Q-factor was degraded to 8.6. The ASE noise was more significant after transmission of 360 km, shown in Figure 2-8(d). The Q-factor was 5.4. After 540km transmission, the eye of the signal was almost closed with the Q-factor of 3.2. It is noted that the eye diagrams of the signal after transmission were not distorted significantly from that at back-to-back except the accumulated ASE noise. This implies that the WDM signals were not suffering greatly from the fiber and SOA nonlinearities, e.g. FWM, and the transmission system was dominated by the accumulated ASE noise. This is consistent with the observed spectrum of the WDM signals in Figure 2-7.

The dependence of the calculated Q-factors of the channel 1 signal on the launching power at different transmission distance was plotted in Figure 2-9. At each launching power, the Q-factor of the signal decreases with increasing transmission distance due to the accumulated ASE noise and corresponding degraded OSNR. At each transmission distance, the Q-factor of the signal increases with the increasing launching power since the current system is dominated

by the ASE noise. This is also because that the inline SOA in the re-circulating loop was indeed working in the linear or slight saturation region to compensate the fiber loss of 22 dB. The signal distortion due to the SOA nonlinearities was observed when the 60 km SSMF was replaced by a shorter one, e.g. 40 km SSMF and the inline SOA was thus working in the saturation region. The reduced Q-factor of the signal after transmission of 360 km when the launching power was increased from -3 dBm to -1 dBm arises from the power fluctuations in the looped signals. Moreover, the inline optical filter in the experiment had a bandwidth (9 nm) much larger than that of the WDM signals (4.5 nm) therefore the OSNR of the signals degraded more rapidly. To improve the Q-factors of the transmitted signals, an inline optical filter with matching bandwidth for the WDM signals need to be used.

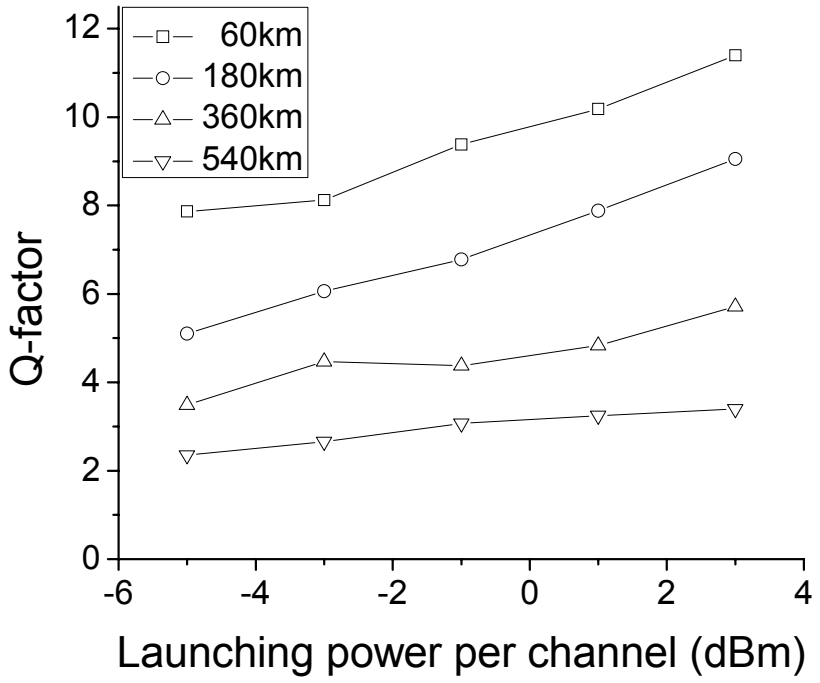

Figure 2-9: Q-factor of the channel 1 after transmission vs. launching power

2.3 References

[1] J. P. Turkiewicz *et al.*, "Do we need 1310 nm transmission in modern networks?" *ECOC'2006*, paper We3.P.153, 2006.

[2] T. Sakamoto *et al.*, "1300 nm-band WDM transmission employing PDFAs," *OATA'1999*, paper SN2, pp.250-253, 1999.

[3] T. N. Nielson *et al.*, "10-Gbit/s repeaterless transmission at 1.3μm with 55.1-dB power budget using Raman post- and preamplifier," *OFC'1998*, paper TuI4, pp.52-53, 1998.

[4] L. F. Tiemeijer, "High performance MQW laser amplifiers for transmission systems operating in the 1310 nm window at bitrates of 10 Gbit/s and beyond," *ECOC'1995*, paper Tu.B.2.1, pp.259–266, 1995.

[5] P. I. Kuindersma *et al.*, "10 Gbit/s RZ transmission at 1309 nm over 420 km using a chain of multiple quantum well semiconductor optical amplifier modules at 38 km intervals," *ECOC'1996*, paper TuD.2.1, pp.165-168, 1996.

[6] J. J. E. Reid *et al.*, "An international field trial at 1.3 μm using an 800 km cascade of semiconductor optical amplifiers," *ECOC'1998*, pp.567-568, 1998.

[7] J. G. L. Jennen *et al.*, "4 × 10 Gbit/s NRZ transmission over 80 km of standard single mode fiber using semiconductor optical amplifiers," *ECOC'1998*, pp.235-236, 1998.

[8] C. Xu *et al.*, "Differential phase-shift keying for high spectral efficiency optical transmissions," *IEEE J. Sel. Topics Quantum Electron.*, vol.10, pp.281-293, 2004.

[9] G. Onishchukov *et al.*, "Differential binary phase-shift keying transmission using cascaded semiconductor optical amplifiers," *CLEO'1999*, paper P1.97, pp.513-514, 1999.

[10]R. A. Linke *et al.*, "High-capacity coherent lightwave systems," *J. Lightwave Technol.*, vol.6, pp.1750-1769, 1988.

[11]J. M. Kahn *et al.*, "4 Gbit/s PSK homodyne transmission system using phase-locked semiconductor lasers," *IEEE Photon. Technol. Lett.*, vol.2, pp.285-287, 1990.

[12]A. H. Gnauck *et al.*, "2.5 Tb/s (64 × 42.7 Gb/s) transmission over 40 × 100 km NZDSF using RZ-DPSK format and all-Raman-amplified spans," *OFC'2002*, PD paper FC-2, 2002.

[13]C. Rasnussen *et al.*, "DWDM 40 G transmission over trans-Pacific distance (10000 km) using CSRZ-DPSK, enhanced FEC and all-Raman amplified 100 km ultrawave fiber spans," *OFC'2003*, 2003.

[14]B. Zhu *et al.*, "6.4 Tb/s (160 × 42.7 Gb/s) transmission with 0.8 bits/s/Hz spectral efficiency over 32 × 100 km of fiber using CSRZ-DPSK format," *OFC'2003*, 2003.

[15]L. F. Tiemeijer *et al.*, "Progress in 1.3 μm polarization insensitive multiple quantum well laser amplifers," *OATA'1994*, pp.34-36, 1994.

[16]L. F. Tiemeiier *et al.*, "27-dB gain unidirectional 1300-nm polarization-insensitive multiple quantum well laser amplifier module," *IEEE Photon. Technol. Lett.*, vol.6, pp.1430-1432, 1994.

[17]G. N. van den Hoven *et al.*, "High performance semiconductor optical amplifiers," *OAA'1997*, paper TuC1, pp.108-111, 1997.

[18]G. Onishchukov *et al.*, “10 Gbit/s transmission over 1500 km with semiconductor optical amplifiers,” *Electron. Lett.*, vol.34, pp.1597-1598, 1998.

[19]J. J. E. Reid *et al.*, “High bitrate 1.3 μm optical transmission in the field using cascaded semiconductor optical amplifiers,” *ECOC’1997*, pp.83-86, 1997.

[20]F. T. Tiemeijer *et al.*, “High-output-power (+15 dBm) unidirectional 1310-nm multiple-quantum-well booster amplifier module,” *IEEE Photon. Technol. Lett.*, vol.7, pp.1519-1521, 1995.

[21]H. de Waardt *et al.*, “89 km 10 Gbit/s 1310 nm repeaterless transmission experiments using direct laser modulation and two SL-MQW laser preamplifiers with low polarization sensitivity,” *IEEE Photon. Technol. Lett.*, vol.6, pp.645-647, 1994.

[22]H. de Waardt *et al.*, “2 × 10 Gbit/s WDM 1310 nm optical transmission over 63.5-km standard single-mode fiber using optical preamplifiers,” *IEEE Photon. Technol. Lett.*, vol.7, pp.104-107, 1995.

[23]G. P. Agrawal, *Nonlinear Fiber Optics*, Academic Press, 1995.

[24]K. Inoue *et al.*, “Wavelength conversion experiment using fiber four-wave mixing,” *IEEE Photon. Technol. Lett.*, vol.4, pp.69-72, 1992.

[25]J. Zhou *et al.*, “Efficiency of broadband four-wave mixing wavelength conversion using semiconductor traveling-wave amplifiers,” *IEEE Photon. Technol. Lett.*, vol.6, pp.50-52, 1994.

3. STUDY ON QUANTUM DOT-SEMICONDUCTOR OPTICAL AMPLIFIERS

3.1 Introduction

Quantum dot (QD) devices have attracted great attention in recent years because of their high differential gain and fast relaxation into the active state from barrier and wetting layer (WL) [1]. QD-SOA can potentially offer many advantages over its bulk and quantum well (QW) counterparts, resulting primarily from three-dimensional quantum confinement of electrons and holes in quantum dots. Ultra-fast gain recovery time on the order of 100 fs has been observed in QD-SOAs, which makes it ideal for ultra-fast signal processing [2]. Recently, QD-SOAs with high gain, high saturation power, and low noise figure over an ultrawide gain spectrum of 120 nm have been developed as a cost-effective alternative to EDFAs for optical transmission [3].

As is with the electrical modulation response of QD lasers [4, 5], the optical modulation response of QD-SOAs is important because it is directly related to the gain fluctuation and, through the linewidth enhancement factor (LEF) or chirp factor α_H [6], the nonlinear phase noise, which in turn determines the performance of transmission systems for phase-modulated signal such as DPSK using SOAs for optical amplification or regeneration [7]. In this chapter we present a QD-SOA model for carrier relaxation and excitation among QD energy states and WL, taking into account overall charge neutrality for the whole device. The DC characteristics of QD-

SOA are studied first followed by an analysis of small signal AC modulation characteristics. The effective carrier lifetime and saturation output power are derived. Finally the optical modulation response and nonlinear phase fluctuation in saturated QD-SOAs are calculated.

3.2 Theory of QD-SOA

3.2.1 Rate Equation Model for QD-SOA

The QDs are assumed to have two discrete energy states, i.e. ground state (GS) and excited state (ES), and a continuum state (CS), which is an ensemble of dense excited states in each dot. Different dots are interconnected through a two-dimensional WL. Our model ignores barrier dynamics and assumes the electrons are injected directly into the WL, then captured by the CS and finally relaxed into the ES and GS. The corresponding rate equations describing the change in carrier (electron) densities in the WL (N_w), CS (N_c), ES (N_2), and GS (N_1), which are all normalized to the active region volume, can be written as [2], [8]-[11]:

$$\frac{\partial N_w}{\partial t} = \frac{J}{eL_w} - \frac{N_w(1-f_c)}{\tau_{wc}} + \frac{N_c(1-f_w)}{\tau_{cw}} - \frac{N_w}{\tau_{wR}} \tag{3-1}$$

$$\frac{\partial N_c}{\partial t} = \frac{N_w(1-f_c)}{\tau_{wc}} - \frac{N_c(1-f_w)}{\tau_{cw}} + \frac{N_2(1-f_c)}{\tau_{2c}} - \frac{N_c(1-f_2)}{\tau_{c2}} + \frac{N_1(1-f_c)}{\tau_{1c}} - \frac{N_c(1-f_1)}{\tau_{c1}} \tag{3-2}$$

$$\frac{\partial N_2}{\partial t} = \frac{N_c(1-f_2)}{\tau_{c2}} - \frac{N_2(1-f_c)}{\tau_{2c}} + \frac{N_1(1-f_2)}{\tau_{12}} - \frac{N_2(1-f_1)}{\tau_{21}} \tag{3-3}$$

$$\frac{\partial N_1}{\partial t} = \frac{N_c(1-f_1)}{\tau_{c1}} - \frac{N_1(1-f_c)}{\tau_{1c}} + \frac{N_2(1-f_1)}{\tau_{21}} - \frac{N_1(1-f_2)}{\tau_{12}} - \frac{N_1 h_1}{\tau_{1R}} - \frac{gP}{\sigma\hbar\omega} \tag{3-4}$$

where J is the injection current density, e is the electron charge, L_w is the thickness of the WL, $\hbar\omega$ is the photon energy corresponding to the GS transition, P is the optical power, σ is the cross-section of the active region. Electron occupation probabilities f_w, f_c, f_2, and f_1 correspond to the WL, CS, ES, and GS, respectively, and are related to electron densities by

$$N_w = 2D_w\tilde{N}_Q f_w,\ N_c = 2D_c\tilde{N}_Q f_c,\ N_2 = 2D_2\tilde{N}_Q f_2,\ N_1 = 2D_1\tilde{N}_Q f_1 \tag{3-5}$$

where D_w, D_c, D_2, and D_1 are the degeneracies of the corresponding electron states. The factor of two is from electron spin. The effective volume density of the QDs is $\tilde{N}_Q$, given by $\tilde{N}_Q = N_Q / L_w$, where N_Q is the surface density of QDs. The modal gain in GS is g, given by $g = g_{\max}(f_1 + h_1 - 1)$, where $g_{\max}$ is the maximum modal gain, which depends on the confinement factor of each QD, the surface density of QDs, the number of QD layers, etc. The hole occupation probability in the GS of the valence band of QDs is h_1. The electron spontaneous recombination lifetimes in the WL and the GS are τ_{wR} and τ_{1R}, respectively. The electron capture time from the WL to the CS is τ_{wc} and described by

$$\tau_{wc} = \frac{\tau_{wc0}}{1 + C_{wc} f_w} \tag{3-6}$$

where τ_{wc0} is the electron capture time solely associated with the phonon-assisted process, C_{wc} is the dimensionless ratio of the Auger-assisted coefficient to the phonon-assisted coefficient in the capture process. The electron escape time from the CS to the WL is τ_{cw} and can be

expressed, under the condition of thermal equilibrium, by

$$\tau_{cw} = \tau_{wc} \exp\left(\frac{\Delta E_{wc}^{c}}{kT}\right) \tag{3-7}$$

where ΔE_{wc}^{c} is the energy separation between the WL bandedge and the CS in the conduction band of QDs, kT is the thermal energy at room temperature. The same relationship is applied to the intra-dot relaxations and excitations thereby the intra-dot relaxation and excitation times in Equation 3-2 to 3-4 can be expressed as

$$\tau_{ij} = \frac{\tau_{ij0}}{1 + C_{ij} f_w}, \quad \tau_{ji} = \frac{D_j}{D_i} \exp\left(\frac{\Delta E_{ij}^{c}}{kT}\right) \tau_{ij}, \quad i = c, 2;\ j = 2, 1;\ i \neq j \tag{3-8}$$

where τ_{ij0} is the phonon-dominated relaxation time and C_{ij} is the dimensionless ratio of the Auger-assisted coefficient to the phonon-assisted coefficient in the relaxation processes, ΔE_{ij}^{c} is the energy separation between the *i*th state and the *j*th state in the conduction band of QDs. Assuming 'k-conservation' in the interband transition, ΔE_{ij}^{c} can be written by

$$\Delta E_{ij}^{c} = \frac{m_h^*}{m_e^*} \Delta E_{ij}^{v}, \quad i, j = w, c, 2, 1 \text{ and } i \neq j \tag{3-9}$$

where ΔE_{ij}^{v} is the energy separation between the corresponding hole states in the valence band of QDs, m_e^* and m_h^* are the effective masses of electron and hole, respectively.

3.2.2 Overall Charge Neutrality of QD-SOA

The overall charge neutrality of QD-SOA can be described by

$$D_1 f_1 + D_2 f_2 + D_c f_c + D_w f_w = D_1 h_1 + D_2 h_2 + D_c h_c + D_w h_w \tag{3-10}$$

where h_w, h_c, and h_2 are the hole occupation probabilities in the WL bandedge, CS, and ES in the valance band of QDs, respectively. Due to the larger effective mass of holes and the resulting small separation between energy levels, holes can be assumed to be in equilibrium all the time over the entire valence band. The hole occupation probabilities satisfy the Fermi-Dirac distribution and can be written as

$$h_i = \frac{1}{1+\exp\left[-\left(\frac{E_i^v - E_f^v}{kT}\right)\right]}, \quad i = w, c, 2, 1 \tag{3-11}$$

where E_i^v is the hole energy level and E_f^v is the quasi-Fermi level of the valence band. The hole occupation probabilities at upper levels can be further expressed as that in the ground state

$$h_i = \frac{1}{1+\exp\left(\frac{\Delta E_{i1}^v}{kT}\right)\left(h_1^{-1}-1\right)}, \quad i = w, c, 2 \tag{3-12}$$

where ΔE_{i1}^v is the energy separation between the bandedge of the WL, CS or ES, and the GS in the valence band. It is also assumed in Equation 3-10 that the electron states in the conduction band and corresponding hole states in the valence band have identical degeneracies assuming '*k*-

conservation' in the transition.

3.2.3 Steady-State Solution

For a continuous wave (CW) incident on the QD-SOA, Equation 3-1 to 3-4 can be solved by setting the left-hand side to zero. At a given optical power $\overline{P}$ and employing Equation 3-10 and 3-12, the electron occupation probability ($\overline{f}_1$) and hole occupation probability ($\overline{h}_1$) in the GS can be solved. Knowing $\overline{f}_1$ and $\overline{h}_1$, the upper level electron occupation probabilities and modal gain can be written as

$$\overline{f}_w = \frac{\tau_{wR}}{D_w \tau_{1R}} \left[I_0 - D_1 \overline{f}_1 \overline{h}_1 - \frac{1}{2}(\overline{f}_1 + \overline{h}_1 - 1) \frac{\overline{P}}{P_{sat0}} \right] \tag{3-13}$$

$$\overline{f}_c = \frac{D_w \overline{f}_w \left(\frac{1}{\tau_{wR}} + \frac{1}{\tau_{wc}} \right) - \frac{I_0}{\tau_{1R}}}{\frac{D_w \overline{f}_w}{\tau_{wc}} + \frac{D_c (1 - \overline{f}_w)}{\tau_{cw}}} \tag{3-14}$$

$$\overline{f}_2 = \frac{\frac{D_c \overline{f}_c}{\tau_{c2}} + \frac{D_1 \overline{f}_1}{\tau_{12}}}{\frac{D_c \overline{f}_c}{\tau_{c2}} + \frac{D_1 \overline{f}_1}{\tau_{12}} + \frac{D_2 (1 - \overline{f}_c)}{\tau_{2c}} + \frac{D_2 (1 - \overline{f}_1)}{\tau_{21}}} \tag{3-15}$$

$$\overline{g} = g_{\max} (\overline{f}_1 + \overline{h}_1 - 1) \tag{3-16}$$

where I_0 is the normalized injection current to the amplifier, given by

$$I_0 = \frac{\tau_{1R}}{2eN_Q} J \tag{3-17}$$

P_{sat0} is an intrinsic parameter related to the saturation output power of the amplifier and can be expressed as

$$P_{sat0} = \frac{\hbar\omega}{\tau_{1R}} \frac{\sigma \tilde{N}_Q}{g_{\max}} \tag{3-18}$$

In a traveling-wave QD-SOA, the evolution of optical power ($\overline{P}$) can be described by [12]

$$\frac{\partial \overline{P}}{\partial z} - \frac{1}{v_g} \frac{\partial \overline{P}}{\partial t} = \left(g - \alpha_{\text{int}} \right) \overline{P} \tag{3-19}$$

where v_g is the group velocity and α_{int} is the internal loss coefficient. Based on the above equation and the steady-state solutions, the optical power and carrier densities along the longitudinal SOA can be calculated numerically through iterations.

3.2.4 Small-Signal Analysis

The small-signal dynamics of QD-SOA is now investigated through a perturbation analysis. To do so, the power, carrier occupation probabilities, and modal gain are assumed to be of the form

$$\begin{aligned} &P = \overline{P} + \Delta P,\ f_w = \overline{f}_w + \Delta f_w,\ f_c = \overline{f}_c + \Delta f_c,\ f_2 = \overline{f}_2 + \Delta f_2, \\ &f_1 = \overline{f}_1 + \Delta f_1,\ \ h_1 = \overline{h}_1 + \Delta h_1,\ \ g = \overline{g} + \Delta g \end{aligned} \tag{3-20}$$

where $\overline{P}$, $\overline{f}_w$, $\overline{f}_c$, $\overline{f}_2$, $\overline{f}_1$, $\overline{h}_1$, and $\overline{g}$ are steady-state solutions to Equation 3-1 to 3-4 and 3-10. Substituting Equation 3-20 into Equation 3-1 to 3-4 and 3-10 and neglecting higher order

terms, the perturbation terms satisfy the following linear differential equations

$$\frac{d}{dt}\begin{pmatrix}\Delta f_w\\ \Delta f_c\\ \Delta f_2\\ \Delta f_1\end{pmatrix}=\begin{pmatrix}c_{ww} & c_{wc} & c_{w2} & c_{w1}\\ c_{cw} & c_{cc} & c_{c2} & c_{c1}\\ c_{2w} & c_{2c} & c_{22} & c_{21}\\ c_{1w} & c_{1c} & c_{12} & c_{11}\end{pmatrix}\begin{pmatrix}\Delta f_w\\ \Delta f_c\\ \Delta f_2\\ \Delta f_1\end{pmatrix}+\begin{pmatrix}0\\ 0\\ 0\\ -\dfrac{\bar{g}}{2g_{\max}\tau_{1R}}\dfrac{\Delta P}{P_{sat0}}\end{pmatrix} \tag{3-21}$$

where each element of the 4 × 4 matrix (C) is a function of the steady-state solutions. The solutions to Equation 3-21 have the form

$$\begin{pmatrix}\Delta f_w\\ \Delta f_c\\ \Delta f_2\\ \Delta f_1\end{pmatrix}=A_w\begin{pmatrix}z_{ww}\\ z_{cw}\\ z_{2w}\\ z_{1w}\end{pmatrix}e^{\lambda_w t}+A_c\begin{pmatrix}z_{wc}\\ z_{cc}\\ z_{2c}\\ z_{1c}\end{pmatrix}e^{\lambda_c t}+A_2\begin{pmatrix}z_{w2}\\ z_{c2}\\ z_{22}\\ z_{12}\end{pmatrix}e^{\lambda_2 t}+A_1\begin{pmatrix}z_{w1}\\ z_{c1}\\ z_{21}\\ z_{11}\end{pmatrix}e^{\lambda_1 t}+\begin{pmatrix}p_w(t)\\ p_c(t)\\ p_2(t)\\ p_1(t)\end{pmatrix} \tag{3-22}$$

The first four terms on the right side of Equation 3-22 denote the general solution and the transient process, in which λ_w, λ_c, λ_2 and λ_1 are the eigenvalues of C corresponding to normalized eigenvectors of $Z_i=\left(z_{wi},z_{ci},z_{2i},z_{1i}\right)^T$, i = w, c, 2, 1; A_w, A_c, A_2, and A_1 are the coefficients determined by the initial conditions. The last term in Equation 3-22 represents the particular solution to Equation 3-21 and describes fluctuations of the carrier densities and modal gain after a long observing time. It can be expressed as

$$\begin{pmatrix}p_w(t)\\ p_c(t)\\ p_2(t)\\ p_1(t)\end{pmatrix}=\begin{pmatrix}z_{ww}e^{\lambda_w t} & z_{wc}e^{\lambda_c t} & z_{w2}e^{\lambda_2 t} & z_{w1}e^{\lambda_1 t}\\ z_{cw}e^{\lambda_w t} & z_{cc}e^{\lambda_c t} & z_{c2}e^{\lambda_2 t} & z_{c1}e^{\lambda_1 t}\\ z_{2w}e^{\lambda_w t} & z_{2c}e^{\lambda_c t} & z_{22}e^{\lambda_2 t} & z_{21}e^{\lambda_1 t}\\ z_{1w}e^{\lambda_w t} & z_{1c}e^{\lambda_c t} & z_{12}e^{\lambda_2 t} & z_{11}e^{\lambda_1 t}\end{pmatrix}\begin{pmatrix}s_w(t)\\ s_c(t)\\ s_2(t)\\ s_1(t)\end{pmatrix} \tag{3-23}$$

where $S(t)=\left(s_w(t)\ s_c(t)\ s_2(t)\ s_1(t)\right)^T$ satisfies

$$\frac{d}{dt}\begin{pmatrix} s_w(t) \\ s_c(t) \\ s_2(t) \\ s_1(t) \end{pmatrix} = \begin{pmatrix} v_{ww}e^{-\lambda_w t} & v_{wc}e^{-\lambda_w t} & v_{w2}e^{-\lambda_w t} & v_{w1}e^{-\lambda_w t} \\ v_{cw}e^{-\lambda_c t} & v_{cc}e^{-\lambda_c t} & v_{c2}e^{-\lambda_c t} & v_{c1}e^{-\lambda_c t} \\ v_{2w}e^{-\lambda_2 t} & v_{2c}e^{-\lambda_2 t} & v_{22}e^{-\lambda_2 t} & v_{21}e^{-\lambda_2 t} \\ v_{1w}e^{-\lambda_1 t} & v_{1c}e^{-\lambda_1 t} & v_{12}e^{-\lambda_1 t} & v_{11}e^{-\lambda_1 t} \end{pmatrix} \begin{pmatrix} 0 \\ 0 \\ 0 \\ -\dfrac{\bar{g}}{2g_{\max}\tau_{1R}}\dfrac{\Delta P}{P_{sat0}} \end{pmatrix} \tag{3-24}$$

where $V=\left(Z_w, Z_c, Z_2, Z_1\right)^{-1}$. The above equation can be solved analytically in the frequency domain assuming $\Delta P(z,t)=\Delta P(z)e^{j\omega t}$. Ignoring the transient process, the relative gain fluctuation is associated with the relative power fluctuation at an arbitrary position of a QD-SOA through

$$\frac{\Delta g(z,\omega)}{\bar{g}(z)} = F(z,\omega)\frac{\Delta P(z)}{\bar{P}(z)} \tag{3-25}$$

Here $F(z,\omega)$ exactly shows the optical modulation response of the QD-SOA and can be expressed by

$$F(z,\omega) = -\left(\frac{X_w\tau_w}{1+j\omega\tau_w}+\frac{X_c\tau_c}{1+j\omega\tau_c}+\frac{X_2\tau_2}{1+j\omega\tau_2}+\frac{X_1\tau_1}{1+j\omega\tau_1}\right)\cdot\frac{1}{2\tau_{1R}}\frac{\bar{P}(z)}{P_{sat0}} \tag{3-26}$$

where

$$X_i = \left[\alpha_w z_{wi}+\alpha_c z_{ci}+\alpha_2 z_{2i}+(1+\alpha_1)z_{1i}\right]v_{i1},\quad i=\text{w, c, 2, 1} \tag{3-27}$$

$$\alpha_j = \frac{D_j}{D_w H_w + D_c H_c + D_2 H_2 + D_1 H_1},\quad j=\text{w, c, 2, 1} \tag{3-28}$$

and

$$H_w = \frac{\exp(\Delta E_{w1}^v / kT)}{\left[\bar{h}_1 + \exp(\Delta E_{w1}^v / kT)(1-\bar{h}_1)\right]^2} \tag{3-29}$$

$$H_c = \frac{\exp(\Delta E_{c1}^v / kT)}{\left[\bar{h}_1 + \exp(\Delta E_{c1}^v / kT)(1-\bar{h}_1)\right]^2} \tag{3-30}$$

$$H_2 = \frac{\exp(\Delta E_{21}^v / kT)}{\left[\bar{h}_1 + \exp(\Delta E_{21}^v / kT)(1-\bar{h}_1)\right]^2} \tag{3-31}$$

$$H_1 = 1 \tag{3-32}$$

The minus sign on the right side of Equation 3-26 indeed reflects the gain saturation of QD-SOA, i.e., the increasing power will lead to the decreasing gain. It is clearly seen that the optical modulation response of the QD-SOA is composed of four low-pass frequency responses, which have characteristic times of τ_w, τ_c, τ_2, and τ_1, corresponding to the contributions from WL, CS, ES, and GS, respectively, where $\tau_i = -\lambda_i^{-1}$, $i =$ w, c, 2, 1. The contribution of each term to the total modulation response is weighed by the corresponding coefficient (X_i, $i =$ w, c ,2, 1 and $\sum_i X_i \approx 1$). Now applying the small signal analysis to Equation 3-19, one can write the propagation equation of the power fluctuation as

$$\frac{\partial \Delta P}{\partial z} - \frac{j\omega}{v_g}\Delta P = (\bar{g} - \alpha_{\text{int}})\Delta P + \bar{P}\Delta g \tag{3-33}$$

Solving Equation 3-25 and 3-33 analytically, the position-dependent gain fluctuation is given by

$$\frac{\Delta g(z,\omega)}{\bar{g}(z)} = F(z,\omega)\exp\left\{\int_0^z F(z',\omega)\bar{g}(z')dz'\right\} e^{j\omega\frac{z}{v_g}} \frac{\Delta P(0)}{\bar{P}(0)} \tag{3-34}$$

where $\Delta P(0)/\bar{P}(0)$ is the relative power fluctuation at the input of QD-SOA and $\bar{g}(z)$ is the position-dependent modal gain in steady-state.

3.2.5 Nonlinear Phase Fluctuation (Noise) through Saturated QD-SOA

It is known that carrier density or gain in SOA introduces a nonlinear phase shift $\phi(\tau)$ to the light wave, which is directly related to the gain $g(z,\tau)$ through [13]

$$\phi(\tau) = -\frac{1}{2}\alpha_H \int_0^L g(z,\tau)dz \tag{3-35}$$

where α_H is the LEF or chirp factor at GS transition wavelength, $g(z,\tau)$ is the time- and position-dependent modal gain and $\tau = t - z/v_g$. In the saturation regime of QD-SOA, if the input optical power varies with time, e.g., from signal-ASE beat noise, $g(z,\tau)$ and $\phi(\tau)$ will also contain a time-varying component. The nonlinear phase fluctuation or noise through saturated QD-SOA can be described by

$$\Delta\phi_{NL}(\tau) = -\frac{1}{2}\alpha_H \int_0^L \Delta g(z,\tau)dz \tag{3-36}$$

And the frequency-dependent nonlinear phase fluctuation can be further written as

$$\Delta\phi_{NL}(\omega) = -\frac{1}{2}\alpha_H \int_0^L \Delta g(z,\omega) e^{-j\omega\frac{z}{v_g}} dz \tag{3-37}$$

3.3 Simulations

In order to study the gain dynamics and optical modulation response of QD-SOAs, Equation 3-1 to 3-4, 3-10 and 3-19 are solved numerically. The parameters used in simulation are [2],[5],[8]-[10],[14]: L = 3 mm (length of the waveguide), L_w = 200 nm, W = 10 μm (strip width of the waveguide); $N_Q = 5 \times 10^{10}$ cm^{-2}, $g_{\max} = 19$ cm^{-1}, $\alpha_{in} = 3$ cm^{-1}; $D_1 = 1$, $D_2 = 3$, $D_c = 10$, $D_w = 250$; $\tau_{wc0} = 1$ ps, $\tau_{c20} = \tau_{c10} = \tau_{210} = 10$ ps, $\tau_{1R} = 1$ ns; $C_{wc} = 0.25$, $C_{c2} = C_{21} = 50$, $C_{c1} = 15$; $m_e^* = 0.026\, m_0$, $m_h^* = 0.0742\, m_0$, where m_0 is the electron mass. As in [2], [14], we take the interband transition energies of the excited state, continuum state and bandedge of the wetting layer as $\hbar\omega$ + 70 meV, $\hbar\omega$ + 150 meV and $\hbar\omega$ + 180 meV, respectively, where $\hbar\omega$ is the photon energy corresponding to the ground state transition.

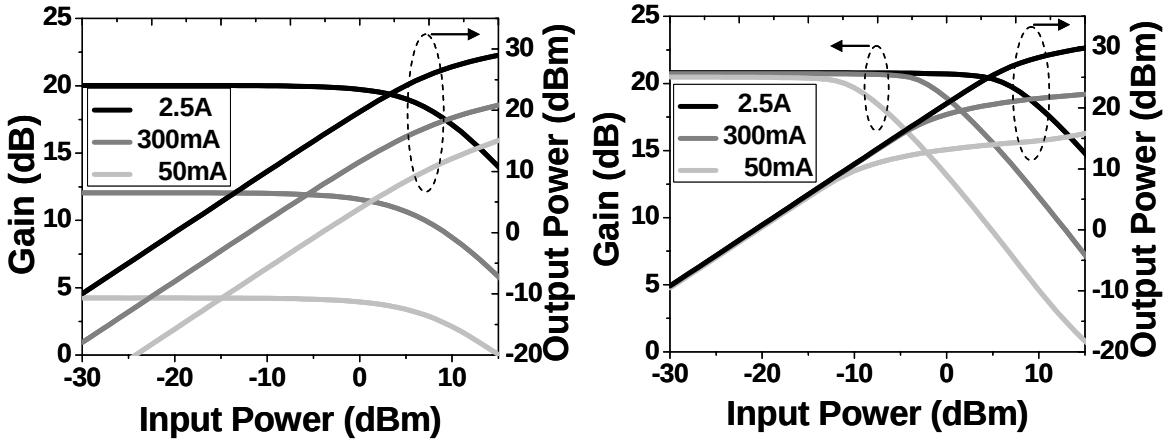

(a) (b)

Figure 3-1: Optical gain and output power of QD-SOAs as functions of input power with (a) charge neutrality for whole device; (b) charge neutrality in GS only

Figure 3-1(a) shows the dependence of the gain and the output power of QD-SOA on the input power at different injection currents when charge neutrality for whole device is assumed. Taking into account the Auger recombination, the electron spontaneous recombination lifetimes in the WL (τ_{wR}) are 1 ns, 0.8 ns, and 0.4 ns, respectively, at injection current of 50 mA, 300 mA, and 2.5 A. It is clearly shown that the small signal gain or the unsaturated gain increases significantly from 4.2 dB at 50 mA to 20 dB at 2.5 A. It is noted that the SOA gain is proportional to the population inversion in GS, i.e. $f_1 + h_1 - 1$. The small unsaturated gain at low injection current is attributed to low hole occupation in GS (h_1) resulting in low population inversion because of the thermal equilibrium among the closely spaced hole states. The similar condition has already been studied for quantum-dot lasers, which usually operate at low injection current, and it is proved that the population inversion and gain of QD lasers can be enhanced by

p-doping the dots [15]. For comparison, Figure 3-1(b) shows the dependence of the gain and the output power of QD-SOA on the input power at the same injection current levels while charge neutrality is only assumed in GS, i.e. $f_1 = h_1$. It is clearly seen in Figure 3-1(b) that this simple assumption overestimates the unsaturated gain at low injection level [16] and only becomes valid for QD-SOAs with high injection current. Hence the overall charge neutrality of QD-SOA is adopted in the following studies of gain dynamics. In Figure 3-1(a), the optical gain starts to saturate as the optical power increases because of the carrier depletion in the QDs. The saturation output power increases as the injection current increases due to the increase of the carrier densities in the WL as well as QDs. However, it is eventually limited by the density of dots and the finite carrier capture and relaxation times. The injection currents of I = 50 mA and I = 2.5 A corresponding to current densities of 0.17 kA·cm^{-2} and 8.3 kA·cm^{-2}, respectively, are adopted in the following simulations to represent low and high injection levels into the QD-SOA. The corresponding saturation output powers are 13.5 dBm and 27.2 dBm, respectively.

3.3.1 Low Current Injection Level

Figure 2 shows the evolution of the optical power of a CW signal and the carrier densities in QDs and WL along the normalized SOA length at the injection current of 50 mA. The optical input power is 12.2 dBm leading to a gain of 1.2 dB, which is 3 dB lower than the unsaturated gain. It is seen in Figure 3-2 that hole occupation probability in GS (h_1) is small due to the low injection current, which leads to a weak population inversion of carriers in GS and small modal

gain of SOA. The carriers in QDs are depleted gradually and signal power increases linearly when the signal propagates along the SOA.

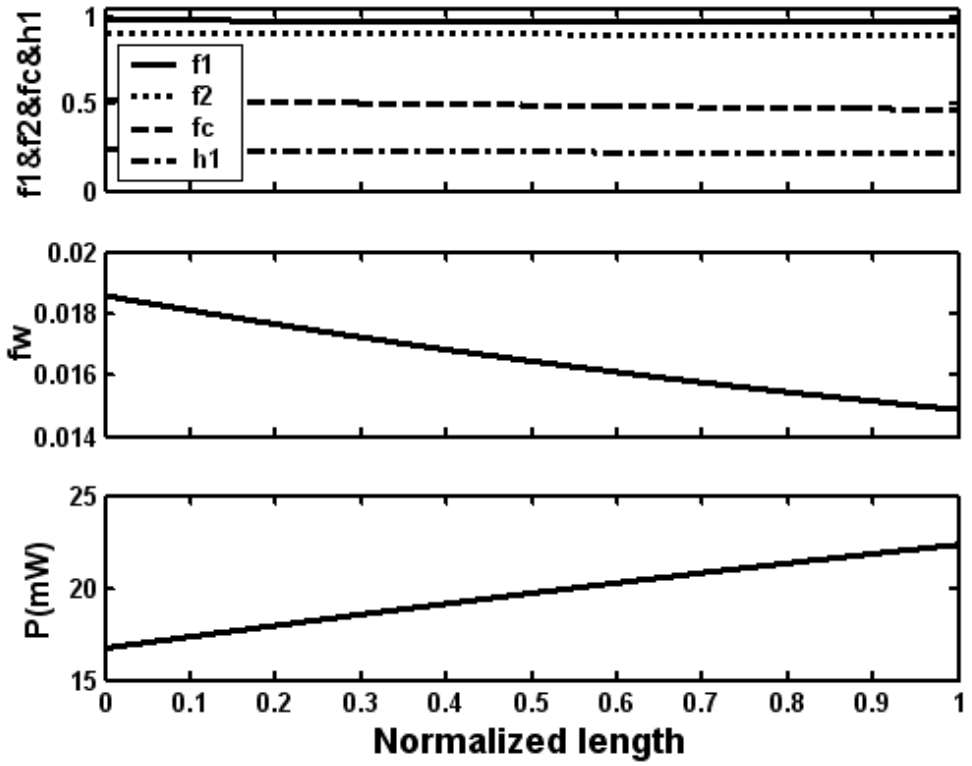

Figure 3-2: Electron occupation probability in GS (f_1), ES (f_2), CS (f_c) and hole occupation probability in GS (h_1) (top); electron occupation probability in WL (f_w) (middle) and optical power (bottom) as a function of the normalized QD-SOA length at I = 50 mA and $\bar{P}(0)$ = 12.2 dBm

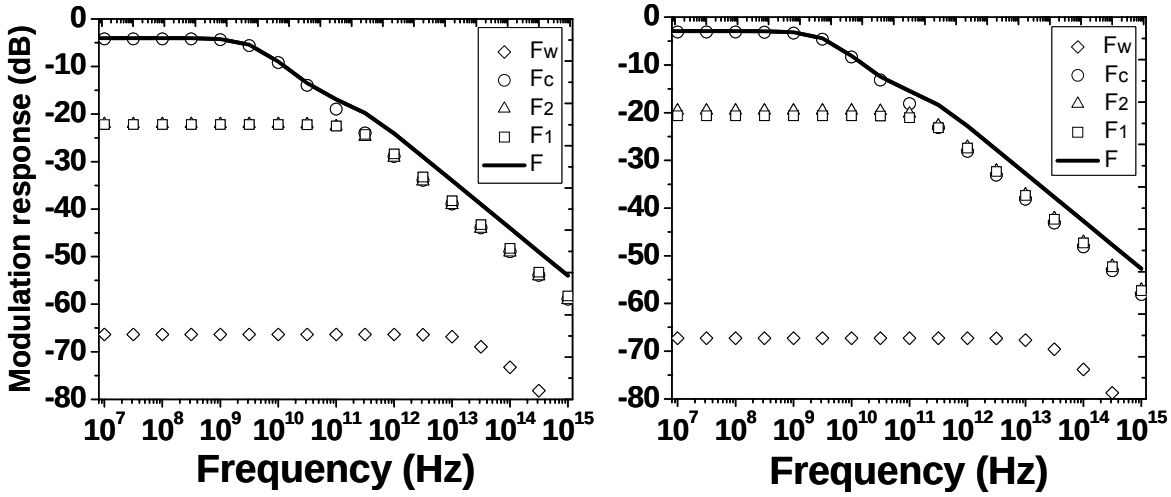

(a) (b)

Figure 3-3: Optical modulation response of QD-SOA at I = 50 mA and (a) $\overline{P}(0)$ = 12.2 dBm; (b) $\overline{P}(L)$ = 13.4 dBm. The contributions to the total modulation response (solid line) due to WL, CS, ES and GS are represented by diamond, circle, triangle and square, respectively

The optical modulation response described by Equation 3-26 is plotted as a function of modulation frequency in Figure 3-3. The total modulation response (solid line) is composed of four low-pass frequency responses, which are the contributions to the dynamics due to WL, CS, ES, and GS, respectively. At the input of the QD-SOA, shown in Figure 3-3(a), the calculated characteristic times corresponding to the contributions from WL, CS, ES and GS are 7.7 fs, 47.6 ps, 0.80 ps and 0.64 ps, respectively. It is clearly shown that the total modulation response of the QD-SOA is dominated by the low-pass frequency response of the continuum state and the effective characteristic time or gain recovery time of the QD-SOA is 47.6 ps. Similarly, the optical modulation at the output of the QD-SOA, shown in Figure 3-3(b), is also dominated by

the CS low-pass frequency response and the gain recovery time of QD-SOA is 50.4 ps. The slow modulation response or gain recovery is attributed to the insufficient carriers supplied into the QDs because of the small injection current. Therefore the gain dynamics of the QD-SOA is dominated by the carrier density pulsation (CDP), which also limits the modulation speed of the bulk and QW SOAs [17]. Similar gain dynamics of QD-SOAs under low injection current as bulk- or QW-SOAs such as data pattern effect has been shown in [9].

3.3.2 High Current Injection Level

In Figure 3-4, the evolution of the carrier densities and the optical power are studied again at higher injection current of 2.5 A. The input power of 10.2 dBm is incident onto QD-SOA to have a gain of 17 dB with the same gain suppression as that in Figure 3-2. Both electrons and holes in QDs are fully populated at the input of the SOA because of the weak stimulated emission and high injection current. Thus the signal experiences high gain and signal power increases exponentially. As the power increases, the electrons in GS are depleted first because of stimulated emission then the electrons in higher energy states and WL are depleted subsequently due to the refilling into the lower energy states. Meanwhile the holes in GS of the dots experience faster depletion than the electrons, which further weakens population inversion in GS and the QD-SOA enters the saturation regime eventually.

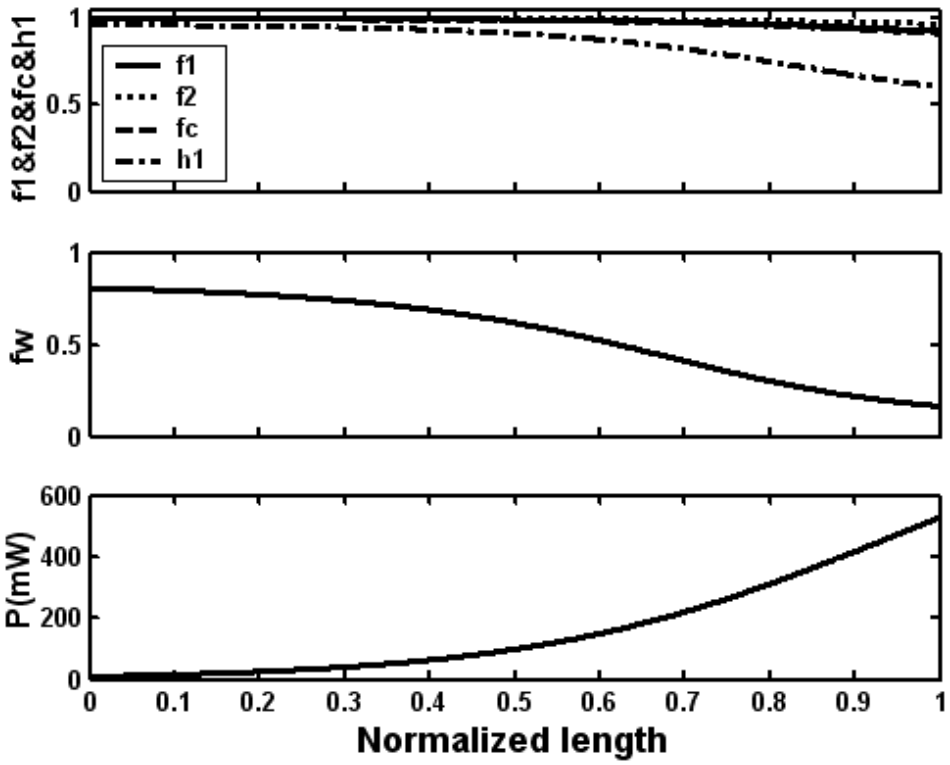

Figure 3-4: Electron occupation probability in GS (f_1), ES (f_2), CS (f_c) and hole occupation probability in GS (h_1) (top); electron occupation probability in WL (f_w) (middle) and optical power (bottom) as a function of the normalized QD-SOA length at $I = 2.5$ A and $\overline{P}(0) = 10.2$ dBm

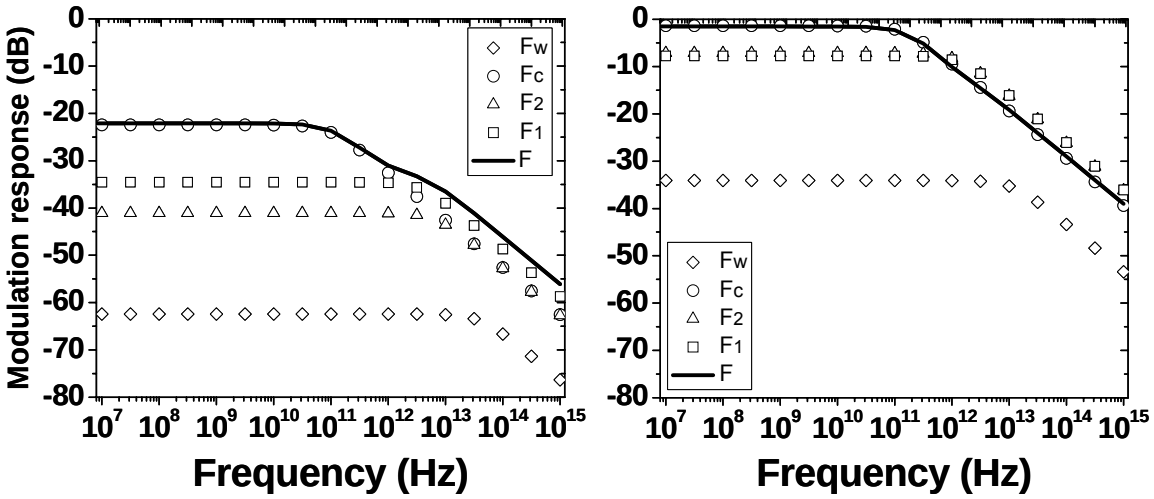

(a) (b)

Figure 3-5: Optical modulation response of QD-SOA at I = 2.5 A and (a) $\bar{P}(0)$ = 10.2 dBm; (b) $\bar{P}(L)$ = 27.2 dBm. The contributions to the total modulation response (solid line) due to WL, CS, ES and GS are represented by diamond, circle, triangle and square, respectively

Figure 3-5 shows the optical modulation response at the input and output of the QD-SOA when the driving current is 2.5A and the average input power is 10.2 dBm. The optical modulation response in Figure 3-5(b) is stronger than that in Figure 3-5(a) because of the higher optical power and stronger gain saturation at the output. It is observed from Figure 3-3 and Figure 3-5 that the optical modulation response of QD-SOA, defined as the relative gain fluctuation to the relative power fluctuation, is always governed by the frequency response of CS, which is characterized by τ_c in Equation 3-26. Hence Equation 3-26 can be approximated by

$$F(z,\omega) \approx -\frac{X_c \tau_c}{1+j\omega\tau_c} \frac{1}{2\tau_{1R}} \frac{\bar{P}(z)}{P_{sat0}} \tag{3-38}$$

Analogous to bulk- and QW-SOAs, the effective gain recovery time and saturation output power of QD-SOA can be written as

$$\tau_{eff,c} \approx \tau_c, \quad P_{sat} \approx \frac{\hbar\omega}{X_c \tau_c} \frac{\sigma \tilde{N}_Q}{g_{\max}} \tag{3-39}$$

The calculated effective gain recovery time is 1.6 ps at the input of the QD-SOA (Figure 3-5(a)), which is dominated by the intra-dot relaxation. The calculated gain recovery time at the output of the QD-SOA in Figure 3-5(b) is 1.0 ps. This faster gain recovery at the output of the QD-SOA is due to stronger stimulated emission. Faster gain recovery of ~0.1 ps can be achieved at higher optical power, which is consistent with the experimental measurement in [18].

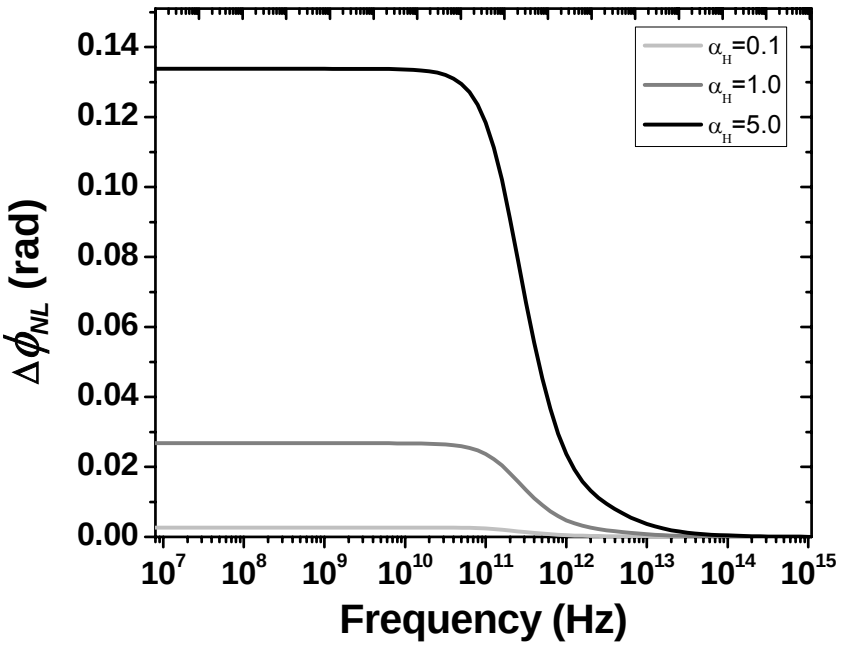

Figure 3-6: Frequency response of the accumulated nonlinear phase fluctuation through the saturated QD-SOA. I=2.5A, $\overline{P}(0)$=10.2dBm and $\Delta\overline{P}(0)/\overline{P}(0) = 0.1$

Based on Equation 3-34 and 3-37, the dependence of the total nonlinear phase fluctuation introduced by the saturated QD-SOA on the small-signal modulation frequency is calculated and plotted in Figure 3-6 for different LEFs. Apparently, the frequency response of nonlinear phase fluctuation through QD-SOA shows similar low-pass features as the optical modulation response of QD-SOA, described by Equation 3-26. The nonlinear phase fluctuation is proportional to the LEF of QD-SOA, which can be from as small as 0.1 to more than 10, depending on the injection current, temperature, photon energy, etc.[19]-[21]. At the LEF of 5.0, shown in Figure 3-6, the amplitude of the accumulated nonlinear phase fluctuation is up to 0.133 radian (0.266 radian or 15.2 degrees in terms of peak-to-peak) for small modulation slower than 40 GHz, which is detrimental to the phase-modulated signals in optical communications operating at 10 Gbit/s or 40 Gbit/s and using QD-SOAs for optical amplifications.

3.4 Discussions and Conclusions

The gain dynamics and optical modulation response in saturated QD-SOAs taking into account the overall charge neutrality have been studied both analytically and numerically. Based on the steady-state solution to and small-signal analysis of the rate equation model, the optical modulation response of QD-SOAs is analyzed semi-analytically, which features a low-pass filtering. Similarly as in bulk- and QW-SOAs, the gain recovery time and saturation output power of QD-SOAs are derived. Compared to the conventional SOAs, QD-SOAs have more

complicated gain dynamics due to stronger couplings among the WL, CS, ES, and GS. The characteristic times are not only dependent on the transition time and carrier lifetime, but also dependent on the carrier densities in WL and CS. Hence the current injection level plays an important role in gain saturation and dynamics of QD-SOAs. When the injection current (density) is low, the WL is not fully occupied and therefore it is not able to refill the lower states promptly after the carriers in lower states are depleted by the strong stimulated emission. The gain recovery time is eventually limited by the carrier lifetime and CDP is dominant. In this case, QD-SOAs show similar performance as bulk- or QW-SOAs, i.e. small saturation power and slow gain recovery [8]. However, at high injection current (density), the WL remains full as carrier reservoir to the lower states and the population in GS is fully inverted because of the higher quasi-Fermi level. The gain recovery is mainly determined by the downward intra-dot relaxation. In this case, the QD-SOAs outperform conventional SOAs with higher saturation power and ultrafast gain recovery. Regarding the application of QD-SOAs in optical transmission systems operating at 10 Gbit/s or 40 Gbit/s, the intensity-modulated signals such as on-off keying (OOK) can be amplified or regenerated without pattern effect due to the ultrafast gain recovery when the QD-SOAs are highly injected; However, for phase-modulated signals such as DPSK, QD-SOAs will introduce the nonlinear phase fluctuations or noise through the SOA chirp and gain saturation.

3.5 References

[1] M. Sugawara *et al.*, "Recent progress of self-assembled quantum-dot optical devices for optical telecommunication: Temperature-insensitive 10 Gb/s directly modulated lasers and 40 Gb/s signal-regenrative amplifiers," *OFC'*2006, paper OTuD6, 2006.

[2] M. Sugawara *et al.*, "Quantum-dot semiconductor optical amplifiers for high-bit-rate signal processing up to 160 Gb/s and a new scheme of 3R regenerators," *Meas. Sci. Technol.*, vol. 13, pp.1683-1691, 2002.

[3] T. Akiyama *et al.*, "An ultrawide-band (120 nm) semiconductor optical amplifier having an extremely high penalty-free output power of 23dBm realized with quantum-dot active layers," *OFC'2004*, paper.PDP12, 2004.

[4] D. Klotzkin and P. Bhattacharya, "Temperature dependence of dynamic and DC characteristics of quantum-well and quantum-dot lasers: a comparative study," *IEEE J. Lightwave Technol.*, vol. 17, pp.1634-1642, 1999.

[5] D. G. Deppe and D. L. Huffaker, "Quantum dimensionality, entropy, and the modulation response of quantum dot lasers," *Appl. Phys. Lett*., vol. 77, pp.3325-3327, 2000.

[6] C. H. Henry, "Theory of the linewidth of semiconductor lasers," *IEEE J. Quantum Electron*., vol. 18, pp.259-264, 1982.

[7] G. Onishchukov *et al.*, "Differential binary phase-shift keying transmission using cascaded semiconductor optical amplifiers ," in *Proc. CLEO/Pacific Rim Conf.*, pp.513-514, 1999.

[8] T. W. Berg *et al.*, "Ultrafast gain recovery and modulation limitations in self-assembled quantum-dot devices," *IEEE Photon. Technol. Lett*, vol. 13, pp.541-543, 2001.

[9] X. Li and G. Li, "Comments on "Theoretical analysis of gain recovery time and chirp in QD-SOA"," *IEEE Photon. Technol. Lett.*, vol. 18, pp.2434-2435, 2006.

[10] T. W. Berg and J. Mørk, "Saturation and noise properties of quantum-dot optical amplifiers," *IEEE J. Quantum Electron.*, vol. 40, pp.1527-1539, 2004.

[11] J. Xiao and Y. Huang, "Numerical analysis of gain saturation, noise figure, and carrier distribution for quantum-dot semiconductor-optical amplifiers," *IEEE J. Quantum Electron*., vol. 44, pp.448-455, 2008.

[12] G. P. Agrawal and N. A. Olsson, "Self-phase modulation and spectral broadening of optical pulses in semiconductor laser amplifiers," *IEEE J. Quantum Electron.*, vol. 25, pp.2297-2306, 1989.

[13] X. Wei and L. Zhang, "Analysis of the phase noise in saturated SOAs for DPSK applications," *IEEE J. Quantum Electron.*, vol. 41, pp.554-561, 2005.

[14] M. Sugawara *et al.*, "Quantum-dot semiconductor optical amplifiers for high bit-rate signal processing over 40 Gbit/s," *Jpn. J. Appl. Phys*., vol. 40, pp.L488-L491, 2001.

[15] D. G. Deppe *et al.*, "Modulation characteristics of quantum-dot lasers: the influence of p-typed doping and the electronic density of states on obtaining high speed," *IEEE J. Quantum Electron*., vol. 38, pp.1587-1593, 2002.

[16]Z. Bakonyi *et al.*, “High-gain quantum-dot semiconductor optical amplifier for 1300 nm,” *IEEE J. Quantum Electron*., vol. 39, pp.1409-1414, 2003.

[17]J. Mørk *et al.*, “The modulation response of a semiconductor laser amplifier,” *IEEE J. Select. Topics Quantum Electron.*, vol. 5, pp.851-860, 1999.

[18]P. Borri *et al.*, “Spectral hole-burning and carrier-heating dynamics in InGaAs quantum-dot amplifiers,” *IEEE J. Select. Topics Quantum Electron.*, vol. 6, pp.544-551, 2000.

[19]T. C. Newell *et al.*, “Gain and linewidth enhancement factor in InAs quantum-dot laser diodes,” *IEEE Photon. Technol. Lett*., vol. 11, pp. 1527–1529, 1999.

[20]S. Schneider *et al.*, “Linewidth enhancement factor in InGaAs quantum-dot amplifiers,”*IEEE J. Quantum Electron*., vol. 40, pp.1423-1429, 2004.

[21]J. M. Vázquez *et al.*, “Linewidth Enhancement Factor of Quantum-Dot Optical Amplifiers,” *IEEE J. Quantum Electron*., vol. 42, pp.986-993, 2006.

4. ELECTRONIC POST-COMPENSATION OF SOA IMPAIRMENTS

4.1 Introduction

The SOA has attracted much attention as a potential substitute for the EDFA for optical transmission due to its low-cost, compactness and ultrawide gain spectrum. It is also the only mature technology for providing amplification in the 1310 nm transmission window. A few transmission experiments using SOAs have been demonstrated using both OOK and DPSK in the 1310 nm and 1550 nm windows [1-4]. The performance in such systems was mainly limited by the ASE noise and nonlinear impairments of the SOA. When the signal power or launching power is low, the systems suffer from the rapid degradation of the signal-to-noise ratio (SNR) at the receiver due to accumulated ASE of SOAs along the link. When the signal power is high, SOAs will be saturated and the signals will suffer from the data pattern effect or SGM, SPM and inter-channel crosstalk effects such as XGM and FWM through SOAs in WDM. In order to maximize the SNR of the received signals while maintaining systems performance, SOA nonlinearities need to be compensated.

This chapter is organized as follows: The principle of SOA impairment compensation (IC) was proposed first based on the backward propagation method; The single SOA IC for intensity-modulated signal was then demonstrated to remove the data pattern effect; Next an

electronic post-compensation for SOA impairments, the first time to my knowledge, was demonstrated experimentally in a non-return-to-zero (NRZ) transmission system. The chapter was concluded in the end.

4.2 Principle of SOA Impairment Compensation

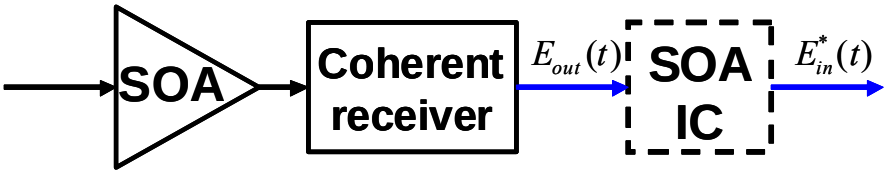

Figure 4-1: Diagram of a single SOA impairment compensation. Optical path: black line; Electrical path: blue line

Figure 4-1 shows the schematic diagram of a single SOA IC. The intensity $P(z,\tau)$, phase $\phi(z,\tau)$ and gain $g(z,\tau)$ of the signal along the SOA can be described by [5]

$$\frac{\partial P}{\partial z} = (g - \alpha_{\text{int}})P \tag{4-1}$$

$$\frac{\partial \phi}{\partial z} = -\frac{1}{2}\alpha_H g \tag{4-2}$$

$$\frac{\partial g}{\partial t} = \frac{g_0 - g}{\tau_c} - \frac{gP}{E_{sat}} \tag{4-3}$$

where α_{int}, α_H, g_0, τ_c, E_{sat} are the internal loss, linewidth enhancement factor, small-signal gain coefficient, spontaneous carrier lifetime, and saturation energy of the SOA, respectively. $E_{out}(t)$ is the measured output electrical field of the SOA after coherent detection. The proposed

IC scheme is based on propagating the distorted signal backward in a virtual SOA in the digital domain by replacing $\partial / \partial z$ with $\partial / \partial(-z)$ in Equation 4-1 to 4-3, which is equivalent to reverse the signs of gain and loss as follows:

$$\frac{\partial P}{\partial z} = (g^{'} - \alpha_{\text{int}}^{'})P \tag{4-4}$$

$$\frac{\partial \phi}{\partial z} = -\frac{1}{2}\alpha_H g^{'} \tag{4-5}$$

$$\frac{\partial g^{'}}{\partial t} = \frac{g_0^{'} - g^{'}}{\tau_c} - \frac{g^{'}P}{E_{sat}} \tag{4-6}$$

where $g^{'} = -g$, $\alpha_{\text{int}}^{'} = -\alpha_{\text{int}}$, $g_0^{'} = -g_0$. Integrating Equation 4-6 over the SOA length (L) and making use of Equation 4-4 to eliminate the product $g^{'}P$ by ignoring $\alpha_{\text{int}}^{'}$ and the spatial dependence of the carrier lifetime τ_c along the SOA, the overall dynamics for $g^{'}$ in the SOA IC can be obtained as follows,

$$\left(1 + \tau_c \frac{d}{dt}\right) h^{'}(t) = h_0^{'} - \frac{P_{out}(t)}{P_{sat}}\left(\exp[h^{'}(t)] - 1\right) \tag{4-7}$$

where $h^{'}(t) = \int_0^L g^{'}(z,t)dz$ and $h_0^{'} = -g_0 L = -\ln G_0$; G_0 is the small signal gain of the SOA. $P_{sat} = E_{sat} / \tau_c$ is the saturation output power of the SOA. $P_{out}(t) = \left|E_{out}(t)\right|^2$ is the output signal intensity of the physical SOA and the input for the SOA IC. Solving Equation 4-4, 4-5 and 4-7, the electric field of the signal after impairment compensation can be written as

$$E_{in}^{*}(t) = E_{out}(t) \cdot \exp\left[\frac{(1 - i\alpha_H)h^{'}(t)}{2}\right] \tag{4-8}$$

Table 4-1: Parameters Values Used for Simulated SOA

Symbol	Description	Value
I	Injection current	0.12 A
L	SOA length	500×10^{-6} m
w	Active layer width	3.0×10^{-6} m
d	Active layer thickness	80×10^{-9} m
Γ	Optical confinement	0.15
α	Internal loss	40×10^{2} m^{-1}
A_g	Differential gain coefficient	2.78×10^{-20} m^2
N_0	Carrier density at transparency	1.4×10^{24} m^{-3}
α_H	Linewidth enhancement factor	5.0
A	Linear recombination constant	1.43×10^{8} s^{-1}
B	Bimolecular recombination constant	1.0×10^{-16} m^3/s
C	Auger recombination constant	3.0×10^{-41} m^6/s
N_{in}	Initial carrier density	3.0×10^{24} m^{-3}

To demonstrate the feasibility of the SOA IC scheme, an optical 10 Gsym/s 16 QAM signal transmission through a saturated SOA with SOA IC was simulated. The 16QAM transmitter and SOA were simulated using the VPI*TransmissionMaker*. The SOA module was based on the *Transmission Line Model* (TLM) and the parameter values are listed in Table 1. The simulated SOA has a small signal gain of 21.8 dB and a saturation output power of 9.8 dBm at the injection current of 120 mA. ASE noise of the SOA was ignored for simplification. SOA IC was implemented by solving Equation 4-7 numerically using the 4^{th} order Runge-Kutta method.

Figure 4-2(a) and Figure 4-2(b) show the constellations of the 16QAM signal before and after the saturated SOA and the corresponding average signal powers are -9 dBm and 9.8 dBm, respectively. The constellation in Figure 4-2(b) rotates due to the SPM effect through the SOA and the radial and angular spreads in each cluster of the constellation arise from the data pattern effect due to gain saturation of the SOA. Figure 4-2(c) indicates that both the SPM effect and the data pattern effect are compensated effectively with SOA IC.

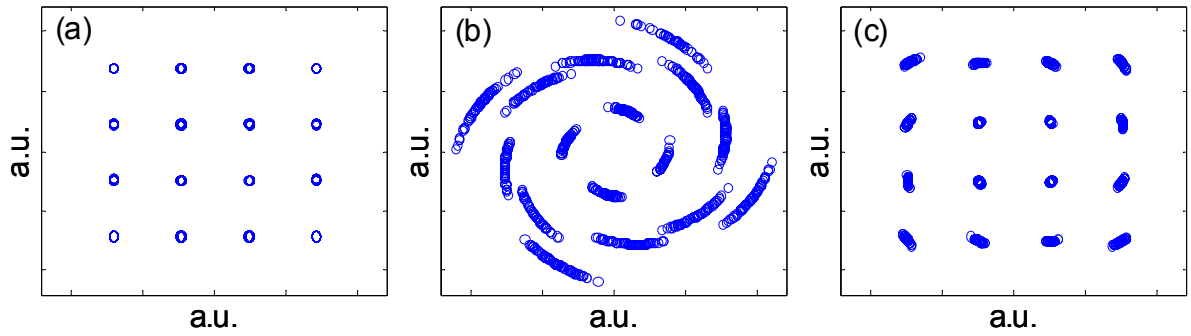

Figure 4-2: Constellation of 16QAM signal a) before SOA; b) after SOA without IC; c) after SOA with IC

The proposed SOA IC scheme here is universal for any modulation format with coherent detection. However coherent detection might not be required in an intensity-modulation system where only SOA IC is needed or the SOA nonlinearities are dominant and signal is not distorted from fiber, which is the case in the following experiments.

4.3 Impairment Compensation for Single SOA

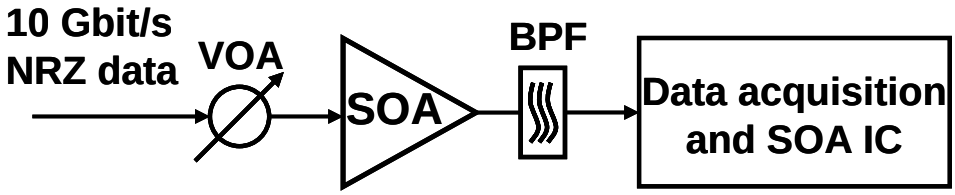

Figure 4-3: Experimental setup for a single SOA IC. VOA: variable optical attenuator; BPF: band-pass filter

Figure 4-3 shows the experimental setup to compensate single SOA impairments for intensity-modulated signal. The 10 Gbit/s NRZ signal was generated by externally modulating a distributed feedback (DFB) laser with pseudorandom binary sequence (PRBS) data from a pulse pattern generator. The variable optical attenuator (VOA) was used to control the input signal power into the bulk SOA, whose gain and output signal power versus input signal power is shown in Figure 4-4. At the injection current of 120 mA, the SOA had a small signal gain of 23 dB (shown as the dashline in Figure 4-4) and 3-dB saturation output power of 6 dBm. An optical band-pass filter with 3-dB bandwidth of 7 nm was used to remove the extra ASE noise after the SOA. At different input signal power levels, the powers of the NRZ signals before photodetection were measured by an optical powermeter and the intensities of the NRZ signals were acquired by an Agilent high-speed sampling oscilloscope.

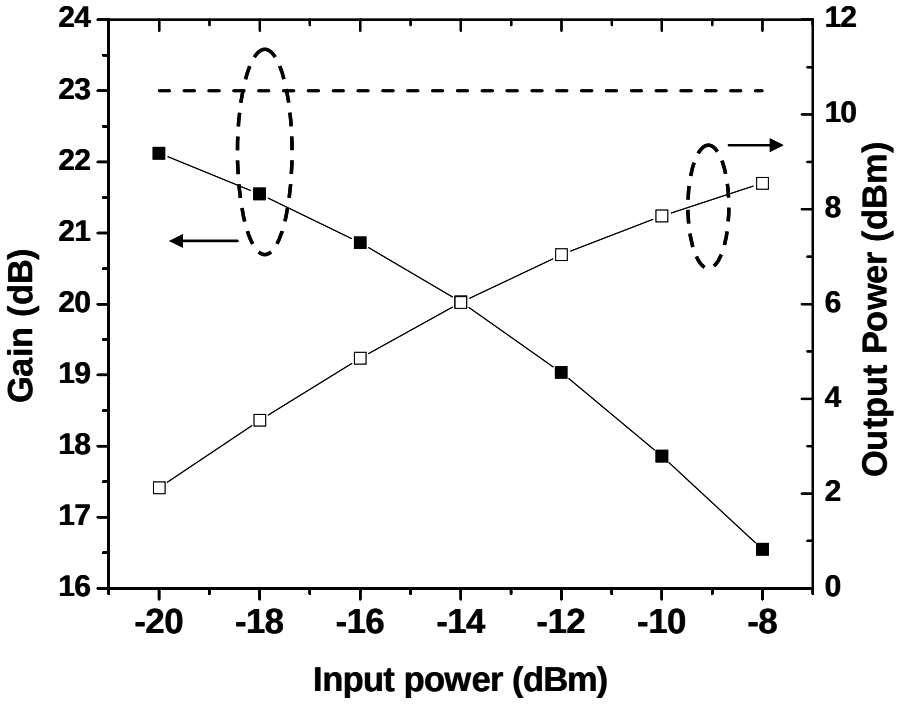

Figure 4-4: Measured output power and SOA gain vs. input power

Instead of coherent detection, direct detection was used in the experiment before SOA IC because the signal intensity instead of phase is required to solve Equation 4-7 and the phase information of the signal after SOA IC is not needed to detect the intensity-modulated signal. Due to the SPM effect through the saturated SOA, the spectra of the received signals are broadened therefore the 10 Gbit/s NRZ signals were sampled at 27 GSa/s to avoid digital aliasing. The signals were then up-sampled to 40 GSa/s or 4 Sa/bit in digital domain to guarantee the temporal resolution for SOA IC. The SOA IC was implemented in software domain by solving the Equation 4-7 using the 4^{th} order Runge-Kutta algorithm, where the measured saturation output power (P_{sat}) and the small signal gain (G_0) of the SOA were used. At each

input signal power level, the effective carrier life time (τ_c) in Equation 4-7 was optimized through global search by maximizing the Q-factor of the NRZ signal after SOA IC, shown in Figure 4-5. It is clearly shown that the optimized τ_c for SOA IC is 349 ps when the input signal power to the SOA is -10 dBm and the calculated Q-factor of the NRZ signal after SOA IC is 22.45 dB. Figure 4-6 shows the optimized carrier life time for SOA IC at different input signal power. The optimized carrier lifetime for SOA IC decreases from 509 ps to 297 ps, which corresponds to acceleration of the average carrier lifetime or gain recovery time in the physical SOA when the input signal power is increased from -20 dBm to -8 dBm.

Figure 4-7(a) shows the eye-diagrams of the NRZ signal before the SOA, i.e., at back-to-back. The NRZ signal had an average power of -10 dBm and signal eye was clearly opened. The calculated Q-factor is 23.4 dB. At the output of the SOA, the NRZ signal was amplified and the measured average power was 7.86 dBm. However the signal eye was almost closed due to the strong data pattern effect through the saturated SOA and the calculated Q-factor was reduced to 13.2 dB, shown in Figure 4-7(b). It is clearly shown in Figure 4-7(c) that no data pattern effect was observed in the NRZ signal after SOA IC because the SOA nonlinearities were compensated effectively. The calculated Q-factor of the NRZ signal is enhanced to 22.8 dB.

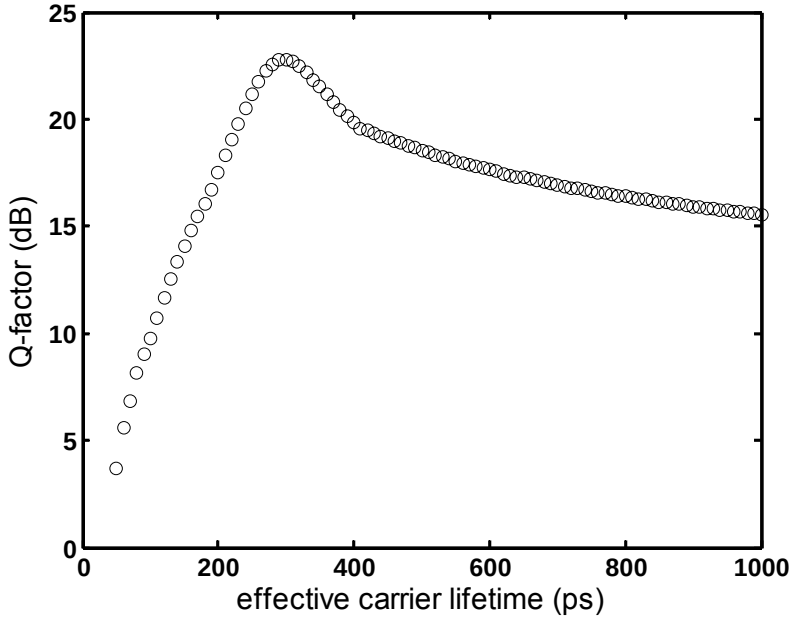

Figure 4-5: Q-factor of the NRZ signal after SOA IC vs. effective carrier lifetime

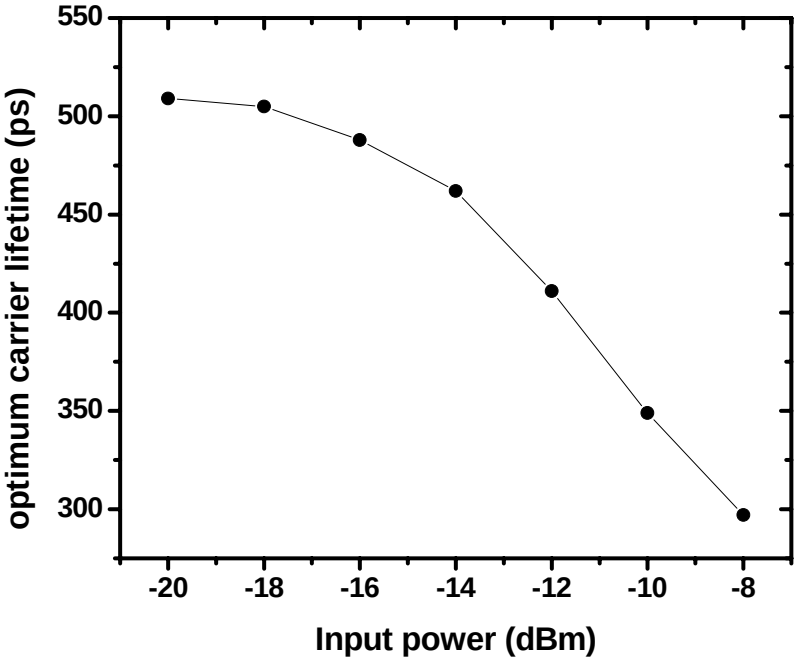

Figure 4-6: Optimized effective carrier lifetime for SOA IC vs. input power of the NRZ signal

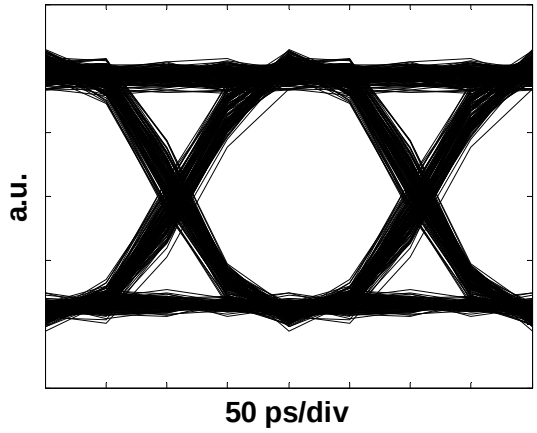

(a)

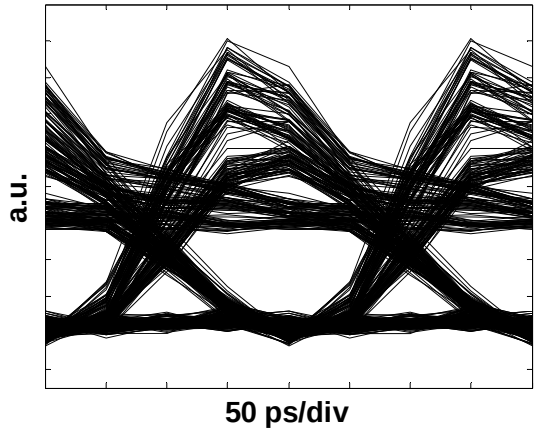

(b)

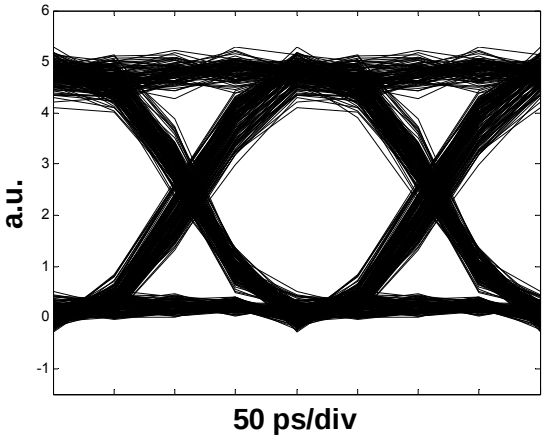

(c)

Figure 4-7: Eye diagrams of the NRZ signal a) before SOA; b) after SOA without SOA IC; c) after SOA with SOA IC

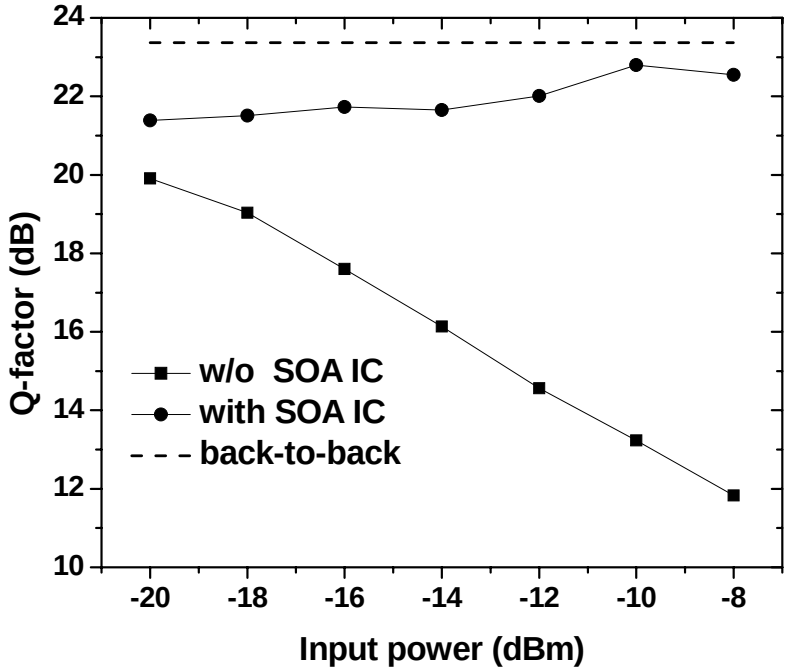

Figure 4-8: Q-factor of the NRZ signal vs. input signal power

Figure 4-8 shows the dependence of the calculated Q-factor of the NRZ signal on the input power to SOA. Without SOA IC, the Q-factor of the NRZ signal after SOA decreases when the input power is increased because the signal suffers more from SOA nonlinearities and data pattern effect. At the low input power e.g. -20 dBm, the Q-factor improvement e.g. 1.5 dB from SOA IC is not significant because the SOA is working in the unsaturated or slightly saturated region and therefore the signal is not distorted much from the SOA nonlinearities. Moreover, the SOA IC is less effective at the low input power because more ASE noise is present in the signal, which has random nature and cannot be compensated through SOA IC. Nevertheless when the input power is high and SOA is deeply saturated, the Q-factor of the NRZ signal is improved

significantly by SOA IC and the less ASE noise in the signal makes the SOA IC more effective. The improvement is up to 10.7 dB when the input power is as high as -8 dBm. The maximum Q-factor of the NRZ signal after the SOA IC is 22.8 dB at the input power of -10 dBm. The 0.6 dB difference in Q-factor, compared to the back-to-back (23.4 dB, shown in dash line), is due to the presence of the ASE in the signal after SOA, which is the fundamental limit for SOA impairment compensation. The Q-factor of the signal after SOA IC starts decreasing when the input power is more than -10 dBm because the NRZ signal experiences more spectral broadening through the highly saturated SOA and hence the sampling rate of 27 GSa/s is not sufficient to avoid the digital aliasing.

4.4 Transmission Experiment of OOK Signal with SOA IC

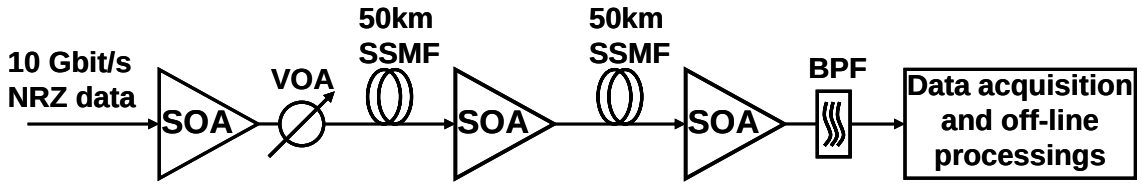

Figure 4-9: Experimental setup of 1310 nm transmission with SOA IC. VOA: variable optical attenuator; BPF: band-pass filter

Figure 4-9 shows the experimental setup for a 1310 nm NRZ transmission experiment over 100 km SSMF with electronic post-compensation for SOA impairments. A 10 Gbit/s NRZ signal was generated by externally modulating a 1310 nm DFB laser with 2^{15}-1 PRBS data from a pulse pattern generator. The first bulk SOA having a small signal gain of 23.5 dB and a saturation

output power of 12 dBm at the injection current of 180 mA worked as a power booster. The variable optical attenuator was used to control the launching power into fiber. The transmission link was composed of two spans of 50 km SSMFs, each of which was followed by a bulk SOA to compensate the fiber loss. The measured fiber losses at 1310 nm were 17.4 dB and 18.4 dB, respectively. At an injection current of 120 mA, these two SOAs had small signal gains of 24 dB and 23.5 dB and saturation output powers of 10 dBm and 7 dBm, respectively. An optical band-pass filter with a 3-dB bandwidth of 7 nm was used to remove the ASE noise before photodetection. At each launching power, the signal powers throughout the transmission link were monitored by an optical powermeter to obtain the SOAs gain. The intensities of the received NRZ signals were acquired by an Agilent high-speed sampling oscilloscope after photodetection. The SOA IC was implemented off-line in the software domain. Direct detection, instead of coherent detection, was used before SOA IC here because the intensity-modulated signal were not distorted from fiber due to negligible chromatic dispersion of SSMF at 1310 nm and thus signal phase was not necessary for SOA IC.

Due to spectral broadening mainly through the SOAs from SPM, the received NRZ data were measured and sampled by the sampling oscilloscope at 27 GSa/s. In off-line processing for SOA IC, the data were first up-sampled to 40 GSa/s or 4 Sa/bit for higher temporal resolution. An ideal noiseless amplifier was assumed between two adjacent SOAs to compensate fiber loss. For each SOA IC, Equation 4-7 was solved numerically using the 4^{th} order Runge-Kutta method with measured small signal gain and saturation output power of the SOA. At each launching

power, the carrier lifetimes of the three SOAs were optimized through global search by maximizing the eye opening after IC.

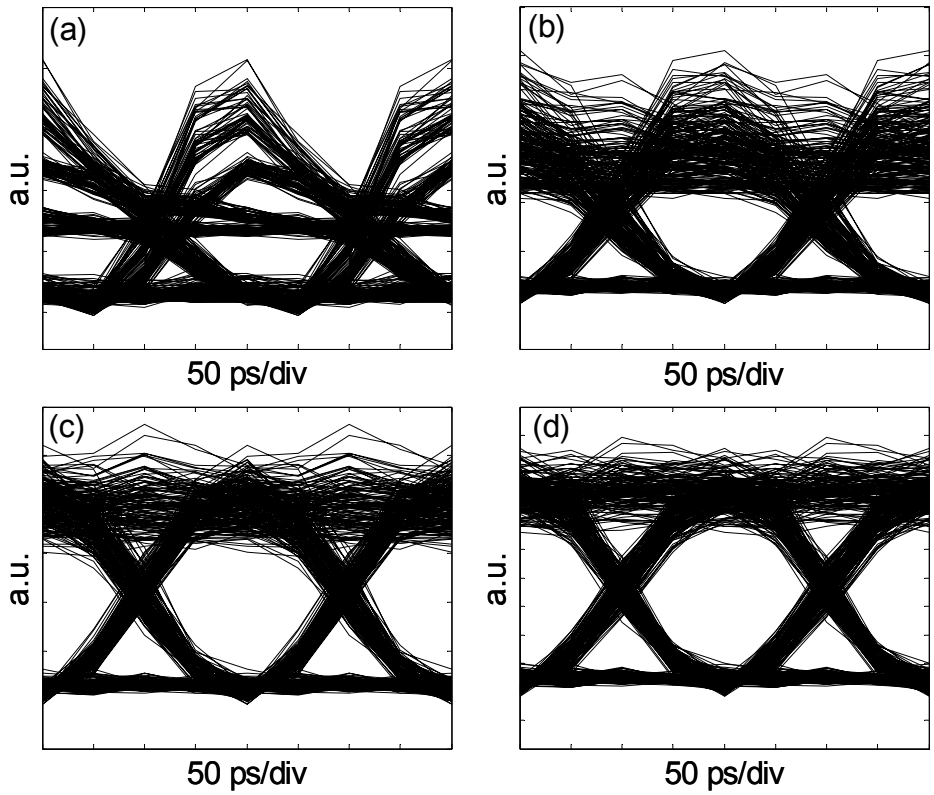

Figure 4-10: Eye diagrams of a) the received NRZ signal and the signal after IC for b) one SOA; c) two SOAs; d) three SOAs

After IC for each SOA, the eye-diagram of the compensated signal was plotted. Figure 4-10(a) shows the eye-diagram of the received NRZ signal after transmission over 100 km SSMF when the launching power into fiber was 5 dBm. Strong pattern effect can be observed due to the accumulated SOA impairments. The eye was almost closed. Some of the pattern effect was compensated after IC for the preamplifying SOA, as shown in Figure 4-10(b). The SOA

impairments were further compensated after IC for the in-line SOA, as shown in Figure 4-10(c). After IC for the power boostering SOA, as shown in Figure 4-10(d), only negligible pattern effect remained in the signal. The optimized carrier lifetimes in IC for the three SOAs were 150 ps, 321 ps and 339 ps, respectively.

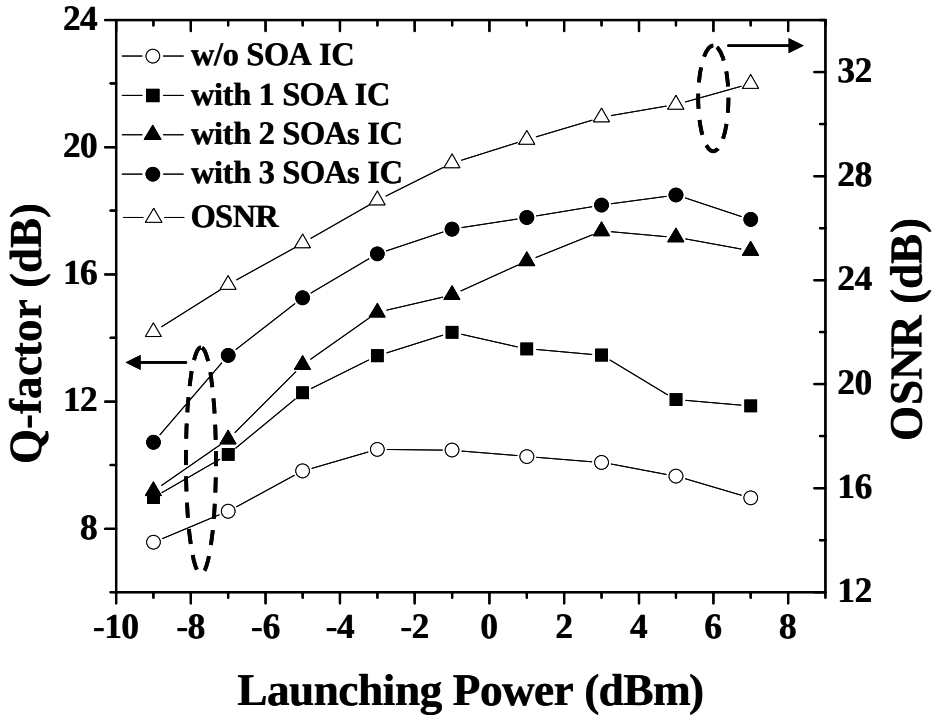

Figure 4-11: Q-factor and OSNR vs. launching power

The dependence of OSNR of the received signal in the optical bandwidth of 0.1 nm and the calculated Q-factor on the optical launching power was shown in Figure 4-11. The received NRZ signals suffer from the accumulated ASE noise at low launching powers and SOAs nonlinearities at high launching powers, respectively. The optimum launching power was about -

2 dBm with the Q-factor of 10.5 dB without IC. The optimum launching power and the corresponding Q-factor were both increased after each SOA IC. After IC for all three SOAs, the optimum launching power was increased to 5 dBm with the Q-factor of 18.5 dB. Compared to the Q-factor of the signal at back-to-back (22.9 dB), the 4.4 dB difference is mainly due to the presence of the accumulated ASE noise in the received signals, which cannot be compensated. The performance can be further improved by using optical filters after each SOA to remove the excess ASE noise.

4.5 Discussions and Conclusions

In conclusion, an electronic post-compensation scheme for SOA impairments has been proposed. Transmission of OOK signal incorporating SOA IC has been demonstrated experimentally over 150 km SSMF and three SOAs. The optimum launching power was increased by 7 dB and the Q-factor of the received NRZ signal was improved by 8 dB with SOA IC. The proposed SOA IC scheme is universal for any modulation format with coherent detection. The 4^{th} order Runge-Kutta algorithm for SOA IC is realized by multiplications, summations and exponential calculations thus SOA IC can be implemented in digital domain by DSP in application-specific integrated circuit (ASIC) chips with multiply-accumulate (MAC) units and lookup tables. The digital processing speed of 40 Gb/s was used in the experiments to make the SOA IC effective. However, the DSP speed may be reduced by using parallel processing. Coherent detection might

not be necessary under some circumstances such as in the demonstrated experiments. However, when fiber dispersion is present, signals will be distorted through the interactions of fiber nonlinearities and dispersion therefore signal phase is required through coherent detection to compensate the impairments in fiber and SOAs simultaneously. The detailed fiber impairment compensation will be depicted in the next chapter. Furthermore, in WDM systems, the full rate equation model for SOAs and the coupled wave equations need to be used. The full knowledge of the exact bit sequences of the WDM channels is required to compensate inter-channel effects such as XGM and FWM through SOAs effectively.

Recently maximum likelihood sequence estimation (*MLSE*) has been employed to increase tolerance to SOA nonlinearities [6]. This method requires a Viterbi decoding procedure whose computation requirement increases exponentially with the accumulated SOA impairments and becomes unacceptable for high spectral efficiency modulation formats such as QAM. For example, the calculations required for decoding one symbol of a 16QAM signal using a Viterbi decoder with a channel memory of 3 symbols involve 61440 comparisons, 4096 summations and 65536 look-ups. Moreover, it cannot mitigate inter-channel nonlinearities through SOAs. However the number of calculations in the SOA IC scheme described here is independent of channel memory and the modulation format, and increases linearly with the number of SOAs. For IC of a single SOA in the transmission experiment, the calculations for each symbol of the received signal include merely 64 multiplications, 78 summations, and 20 look-ups.

4.6 References

[1] P. I. Kuindersma *et al.*, "10 Gbit/s RZ transmission at 1309 nm over 420 km using a chain of multiple quantum well semiconductor optical amplifier modules at 38 km intervals," *ECOC'*1996, paper TuD.2.1, pp.165-168,1996.

[2] G. Onishchukov *et al.*,"Differential binary phase-shift keying transmission using cascaded semiconductor optical amplifiers," in *Proc. CLEO®/Pacific Rim* 1999, pp.513-514,1999.

[3] L. H. Spiekman *et al.*, "8 × 10 Gb/s DWDM transmission over 240 km of standard fiber using a cascade of semiconductor optical amplifiers," *IEEE Photon. Tech. Lett.*, vol.12, pp.1082-1084, 2000.

[4] Z. Li *et al.*, "1050-km WDM transmission of 8 × 10.709 Gb/s DPSK signal using cascaded in-line semiconductor optical amplifiers," *IEEE Photon. Tech. Lett.*, vol.16, pp.1760-1762, 2004.

[5] G. P. Agrawal and N. A. Olsson, "Self-phase modulation and spectral broadening of optical pulses in semiconductor laser amplifiers," *IEEE J. Quantum Electron.*, vol.25, pp.2297-2306, 1989.

[6] J. D. Downie and J. Hurley, "Performance of an MLSE-EDC receiver with SOA-induced nonlinear impairments," *IEEE Photon. Tech. Lett.*, vol.20, pp.1326-1328, 2008.

5. ELECTRONIC POST-COMPENSATION OF FIBER IMPARIMENTS

5.1 Introduction

The degree to which fiber impairments are compensated determines the transmission capacity of fiber optic transmission systems. DCF is commonly used to compensate chromatic dispersion [1]. WDM systems suffer from both intra- and inter-channel nonlinearities such as XPM and FWM. These effects can be suppressed using dispersion management [2, 3]. Thorough compensation of nonlinear impairments in fiber has become the next logical step in increasing capacity of WDM systems. A few optical nonlinearity compensation schemes have been demonstrated such as lumped compensation of self-phase modulation [4] and optical phase conjugation for the compensation of both chromatic dispersion and Kerr nonlinearity in fibers [5].

Electronic dispersion compensation (EDC) and electronic nonlinearity compensation (ENLC) have received significant attention in recent years. Several electronic pre-compensation schemes have been demonstrated to compensate chromatic dispersion or nonlinearity in single-channel or WDM system [6-9]. These schemes pre-distort the transmitted signals using arbitrary waveform generators. Pre-distortion is calculated using optical phase conjugation or backward propagation, i.e., the signal is distorted by virtual fiber while compensated through the real fiber

transmission. Post-compensation using coherent detection and DSP has been shown to be very effective in chromatic dispersion compensation [10] and intra-channel nonlinearity compensation [11]. Post-compensation offers great flexibility since adaptive compensation can be incorporated in this scheme.

This chapter is organized as follows. The principle of the universal post-compensation for fiber dispersion and nonlinearity compensation is first described based on backward propagation. Then an approach for real-time implementation of backward propagation using coherent detection and DSP is proposed. Finally the simulation for simultaneous compensation of fiber dispersion and nonlinearity in a WDM system is demonstrated.

5.2 Post-Compensation Based on Backward Propagation

The schematic diagram of a WDM transmission system with post-compensation of fiber impairments is shown in Figure 5-1. The post-compensation is performed in the digital domain after coherent detection. The WDM signals (total number of channel is C) are transmitted over multiple amplified fiber spans. After transmission, the received signals are mixed in a 90° optical hybrid with a set of local oscillators (LOs), of which C LOs are aligned at the center of the WDM channels. Additional LOs on both sides are aligned with other FWM components outside the WDM signals. The in-phase and quadrature components of each WDM channel are obtained by balanced photodetectors. Analog-to-digital (A/D) conversion is followed by DSP to achieve post-compensation and data recovery.

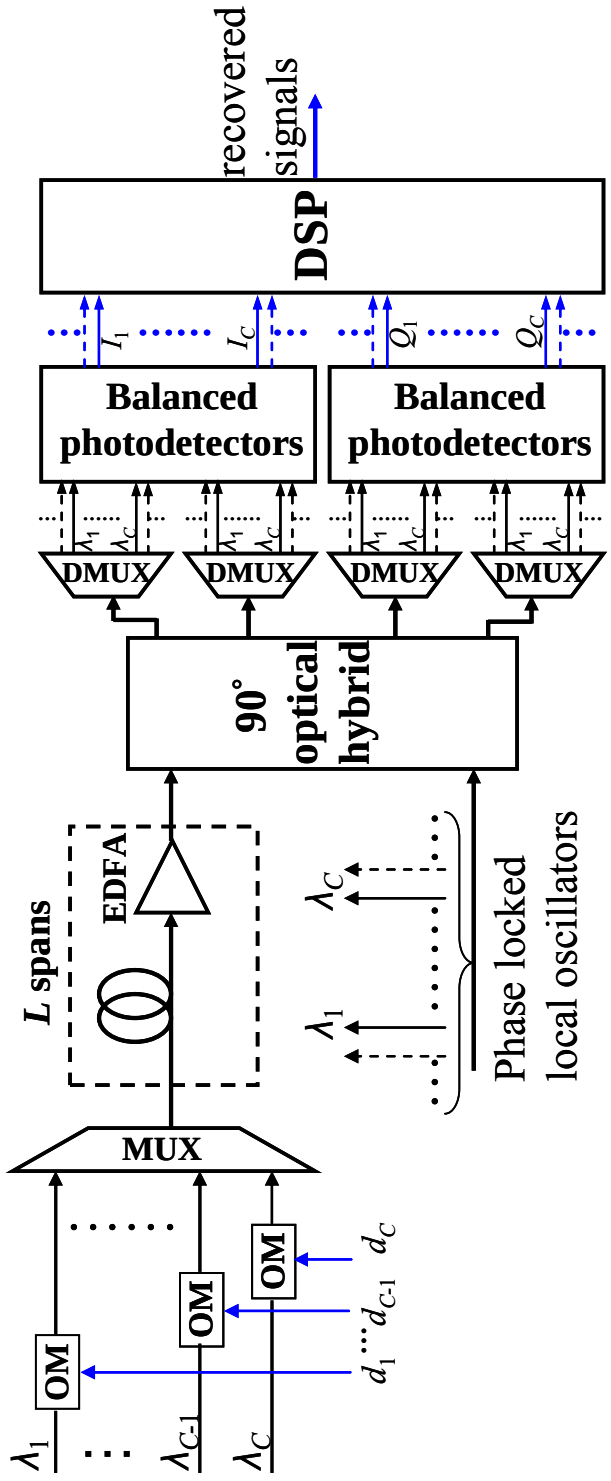

Figure 5-1: WDM system with fiber dispersion and nonlinearity compensation using coherent detection and DSP. Optical path: black line; Electrical path: blue line; OM: optical modulator; EDFA: Erbium-doped fiber amplifier

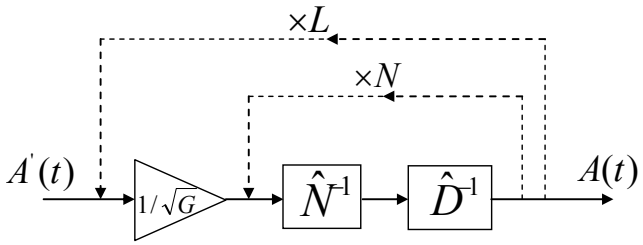

Figure 5-2: Diagram of backward propagation for a multi-span fiber link. *L*: span number; *N*: step number per span

The backward propagation compensation scheme for a multi-span fiber link is shown in Figure 5-2. G is the optical gain of the linear optical amplifiers in the fiber link, $A'(t)$ and $A(t)$ are the electric fields of the received signal and the compensated signal, respectively. The nonlinear Schrödinger equation (*NLSE*) governing the backward propagation in each span can be written in the form $\frac{\partial A}{\partial z} = \left(\hat{N}^{-1} + \hat{D}^{-1}\right) A$, where $\hat{N}^{-1}$ and $\hat{D}^{-1}$ are inverse nonlinear and differential operators, respectively, and given by [12]:

$$\hat{N}^{-1} = i\gamma' \left|A\right|^2, \quad \hat{D}^{-1} = -\frac{i\beta_2'}{2}\frac{\partial^2}{\partial T^2} + \frac{\beta_3'}{6}\frac{\partial^3}{\partial T^3} - \frac{\alpha'}{2} \tag{5-1}$$

where γ', β_2', β_3' and α' are fiber nonlinear, first- and second-order chromatic dispersion, and loss coefficient. When these parameters are chosen to be exactly the negative of the values for transmission fiber, nonlinearity and dispersion could be compensated through backward propagation. Equation 5-1 is most commonly solved using the split-step Fourier method. In this approach, each span of fiber is divided into N sections and $\hat{N}^{-1}$ and $\hat{D}^{-1}$ are implemented iteratively. To facilitate real-time implementation, the dispersion or differential operator ($\hat{D}^{-1}$)

can be realized using a finite impulse response (FIR) filter instead of Fourier transform, which has been shown to achieve acceptable accuracy [13].

5.3 DSP Implementation for Backward Propagation

To implement backward propagation in the digital domain in real time, two technological constraints must be addressed. First, backward propagation requires the optical field at the end of the transmission fiber be sampled with sufficient temporal resolution. Second, the limit of DSP speed requires parallelization of the post-compensation to cover the entire spectrum of interest.

In the proposed approach, each WDM channel is translated to the baseband using coherent detection. The LOs for all WDM channels must be phase-locked for the post-compensation to function properly. Each complex field (at baseband) is sampled at two samples per symbol. In the method proposed here, the received signal corresponding to all WDM channels is considered as a whole for backward propagation, rather than on a channel by channel basis. The baseband signals are up-sampled in the digital domain to ensure sufficient temporal resolution for backward propagation. Details of up-sampling and parallel implementation are discussed using a 10 Gbaud/s WDM system with channel spacing of 20 GHz as an example.

5.3.1 Signal Up-sampling

Parallel composition of this signal from the obtained 20 Gsa/s baseband streams is achieved as follows. Designating the sampling rate of each A/D converter as F_s, a set of N_c

coherent receivers may cover a total bandwidth of $N_c \cdot F_s$. Up-sampling to a bandwidth of $M \cdot F_s$ (M is an integer and $M > N_c$) can be achieved in the digital domain using the following generalized formula:

$$r_n = r\left(t = \frac{n}{M \cdot F_s}\right) = \sum_{i=0}^{N_c-1} s_{i,k(n)} \cdot e^{j \cdot 2 \cdot \pi \cdot \frac{i - \frac{N_c - 1}{2}}{M}} \tag{5-2}$$

where $s_{i,k}$ is the sample at time $t = k / F_s$ of the ith frequency band and $k(n) = \lfloor n / M \rfloor \cdot M / F_s$, where $\lfloor x \rfloor$ stands for the nearest integer smaller than or equal to x. The above formula effectively zero-pads the spectrum to obtain up-sampling. Note that each re-sampled data point is calculated independently, making this spectral stitching technique highly compatible with parallel implementation. If the DSP speed is 10 GHz, 32 streams of 10 Gsa/s are required to cover the 320 GHz total spectrum. Recall that sampling is at 20 GHz so two identical sets of resampling modules, operating independently, should be used for up-sampling. To align the outputs from the two up-sampling modules, the output from the first module may be delayed by 50 ps.

5.3.2 Parallel Implementation for Backward Propagation

Figure 5-3 illustrates the block diagram of parallel implementation for backward propagation, showing the feasibility of real-time operations. $N_s = L \times N$ is the total step number in the backward propagation. The processing rate of DSP is R_P. In simulation, R_P is assumed to be 10 GHz, same as the symbol rate. However, the processing rate can be reduced using time-

division DEMUX technique, which requires more processing units but helps the real-time operation at a lower rate [14].

After up-sampling, N_b sampling points are generated in parallel and output simultaneously in N_b branches for every period T, where $N_b = M \cdot F_s / R_P$ is the number of parallel processing branches, and $T = 1/R_P$ is the clock cycle in each branch. One-symbol delay latches for some branches are used to obtain additional outputs for the parallel implementation of the following FIR filter. The number of additional outputs is $N_t - 1$, where N_t is the FIR filter length or tap number. $A_{k,i}$ is the *k*th sampling point in the *i*th symbol and is processed in the *k*th branch. Sampled data from all the branches are then sent into a number of cascaded modules to realize backward propagation using the split-step FIR method [13]. Each module performs one step in the backward propagation, compensating loss, dispersion and nonlinearity of a small segment of fiber. The number of modules equals to the step number. Each step contains N_b sub-units to perform backward propagation for each branch respectively. M_k is the sub-unit in the *k*th branch of each step. $A_{k,i}(n)$ is the output of the *k*th branch in the *n*th step and *i* is the symbol index.

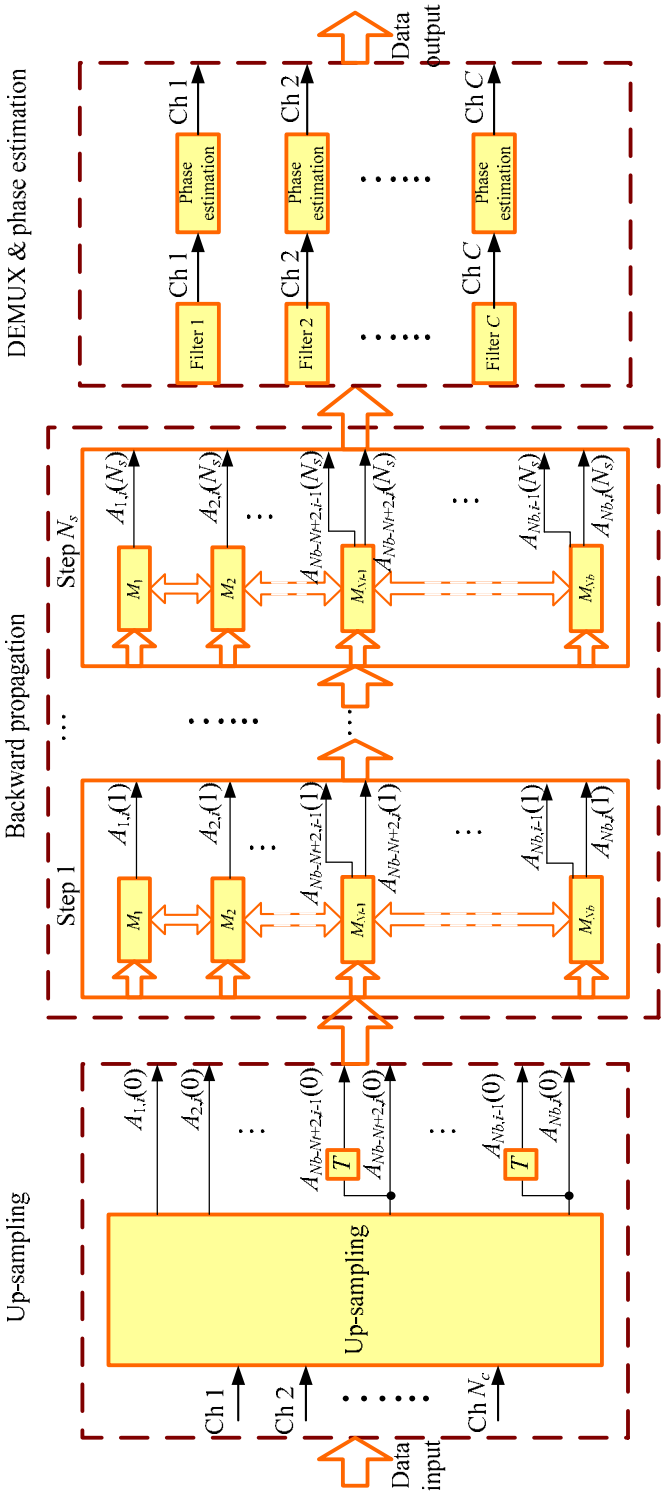

Figure 5-3: Block diagram of parallel implementation for backward propagation using DSP technique. The hollow arrows represent multiple inputs or outputs and the solid arrows represent single input or output

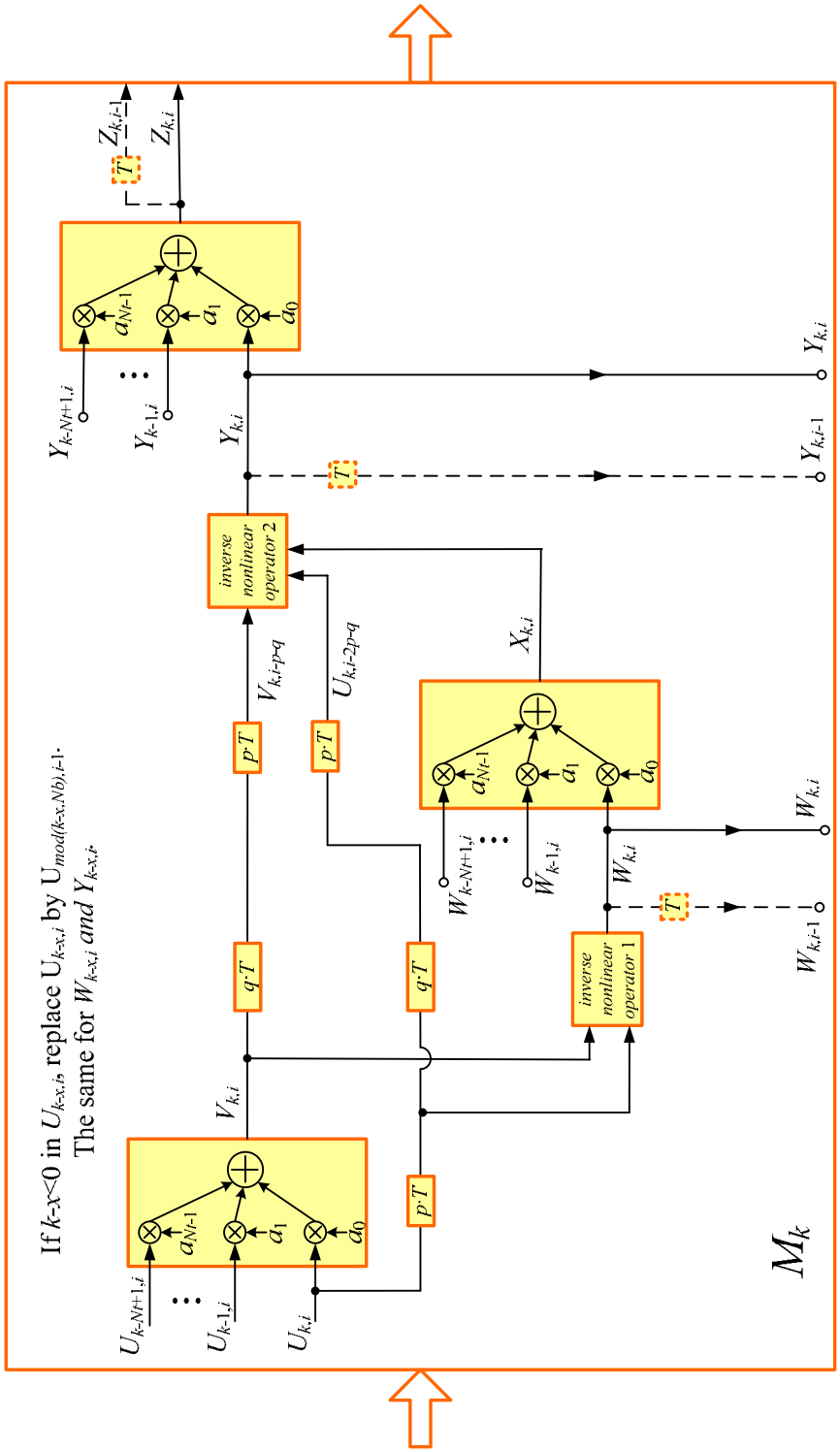

Figure 5-4: Block diagram of the sub-unit M_k in the kth branch in backward propagation. The inputs and outputs terminated by a circle may interface with other branches. The dashed lines only apply to some modules. $p{\cdot}T$ is the delay of FIR filter, and $q{\cdot}T$ is the delay of *inverse nonlinear operator 1*

The block diagram of the sub-unit is shown in Figure 5-4. The coefficients of the FIR filter used for dispersion compensation are designated by a_i, where $i \in 0..N_t - 1$. The inputs and outputs from Figure 5-3 are renamed to simplify the illustrations. The sub-unit is designed according to the symmetric split-step scheme with two iterations when solving the *NLSE* [12]

$$A(z+h,T) \approx \exp\left(\frac{h}{2}\hat{D}^{-1}\right)\exp\left(\int_z^{z+h}\hat{N}^{-1}(z')dz'\right)\exp\left(\frac{h}{2}\hat{D}^{-1}\right)A(z,t) \tag{5-3}$$

To improve the accuracy for the split-step FIR method, the trapezoidal rule was used in the simulation to calculate the nonlinearity and approximate the integral by

$$\int_z^{z+h}\hat{N}^{-1}(z')dz' \approx \frac{h}{2}[\hat{N}^{-1}(z)+\hat{N}^{-1}(z+h)] \tag{5-4}$$

It is necessary to follow an iterative procedure initiated by replacing $\hat{N}^{-1}(z+h)$ using $\hat{N}^{-1}(z)$, then use Equation 5-3 to estimate $A(z+h,T)$ which in turn is used to calculate the new value of $\hat{N}^{-1}(z+h)$. As shown in Figure 5-4, three FIR filters are used for dispersion and loss compensation and two inverse nonlinear operators for nonlinearity compensation in a sub-unit. The *inverse nonlinear operator* 1 performs $\exp\left\{h\hat{N}^{-1}(z)/2\right\}$ and the *inverse nonlinear operator* 2 performs $\exp\left\{h(\hat{N}^{-1}(z)+\hat{N}^{-1}(z+h))/2\right\}$. $Y_{k,i}$ is the output of the first stage and $Z_{k,i}$ is the output of the second stage. The FIR filter is implemented in a parallel configuration, which has multiple inputs instead of one input combined with a series of delay latches. Therefore, each unit operates at a speed of R_P although the overall bandwidth is $N_b \cdot R_P$ [7]. Since the FIR filters

need multiple inputs, all the branches have to interface with adjacent ones. This is represented by the ports terminated with a circle in Figure 5-4. Similar to the up-sampling module, each of the $N_t - 1$ sub-units (from the ($N_b - N_t + 2$)*th* to the (N_b)*th*) has two outputs to the next step, while the other sub-units only have one output. The additional outputs in the $N_t - 1$ sub-unit are required for the inputs of the FIR filters in the next step. Also, additional interfaces with adjacent branches are needed in these $N_t - 1$ sub-units. All the additional outputs and modules required in some sub-units are indicated by the dashed lines in Figure 5-3. Since each module processes only signals that are already available, the scheme can be carried out in real time.

After backward propagation, the desired WDM channel signal is down-converted to the baseband and then chosen by a low-pass FIR filter. After filtering, the signal in each channel is resampled to one sample per symbol and phase estimation is performed to recover the data.

The computation efficiency and latency of this DSP processing scheme should be investigated. Most operations are required by the backward propagation because of the recursive processes for long-haul transmission. Ignoring the computation and latency caused by up-sampling and DEMUX & phase estimation, the number of required multiply-accumulate (*MAC*) units is

$$N_{MAC} = N_s \times N_b \times (12 \times N_t + 9) \tag{5-5}$$

The total number of *MAC*s is calculated as follows. Each FIR filter requires $4 \times N_t$ multiplications and $4 \times N_t - 2$ summations; *inverse nonlinear operator* 1 requires 7

multiplications and 3 summations; *inverse nonlinear operator* 2 requires 9 multiplications and 5 summations. The latency of the backward propagation scheme is

$$T_L = N_s \times (3 \times \lceil \log_2 N_t \rceil + 21) \times \frac{T}{2} \tag{5-6}$$

where $\lceil x \rceil$ stands for the nearest integer greater than or equal to x. A look-up table is used for the calculation of e^{jx}. The latency is calculated as follows. It is assumed that the look-up table requires one clock cycle (T) and each multiplication or summation requires half of clock cycle ($T/2$). Each FIR filter requires $(\lceil \log_2 N_t \rceil + 2) \times (T/2)$; *inverse nonlinear operator* 1 and *inverse nonlinear operator* 2 require $7 \times (T/2)$ and $8 \times (T/2)$, respectively.

5.4 Simulations

In the numerical simulations, the WDM system consists of 10 × 10 Gbit/s binary phase-shift keying (BPSK) channels distributed around 1550 nm with a channel spacing of 20 GHz. The BPSK signals are generated by driving phase modulators with de-correlated 10 Gbit/s NRZ PRBS data. The forward transmission of WDM signals over dispersion-shifted fiber (DSF) is simulated using the VPITransmissionMaker. The fiber loss, dispersion, dispersion slope, and nonlinearity at 1550 nm are 0.2 dB/km, 0 ps/km/nm, 0.04 ps/km/nm^2, and 1.8 /W/km, respectively. The EDFAs are set to power mode with noise figure of 5 dB. Both transmitter lasers and LOs have linewidth of 2 MHz. The initial relative phases of the transmitter lasers are

set to zero without loss of generality. The optical demultiplexers have a 3-dB bandwidth of 19 GHz and the photodetectors have an electrical bandwidth of 9 GHz.

Using coherent detection, each 20 GHz band is translated to baseband and sampled at 20 GSa/s and thus the total sampling rate of the 10 WDM channels plus two extra FWM channels is 240 GSa/s. The inclusion of two extra FWM channels, adjacent to the WDM channels, is necessary for nonlinearity compensation. Then the signal is up-sampled to a total bandwidth of 320 GHz. The DSP speed is assumed to be 10 GHz. So F_s = 20 GHz, N_c = 12, M = 16, N_b = 32, and T = 100 ps.

Using the symmetric split-step scheme for backward propagation, the step number in each DSF span is reduced to 50, corresponding to 2 km of DSF. The FIR filter used for dispersion compensation is 33 taps long. The filter coefficients are extracted by an inverse Fourier transform of the DSF frequency response. The low-pass FIR filter used after backward propagation for demultiplexing has a 3-dB bandwidth of 10 GHz.

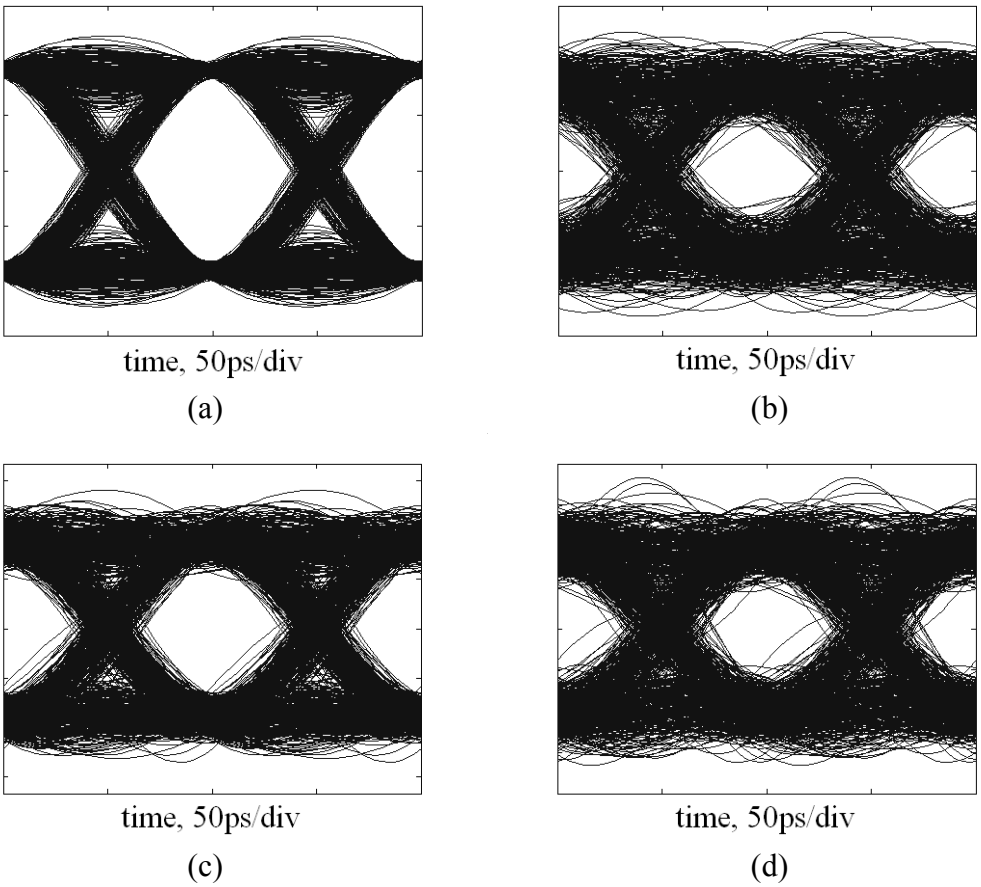

Figure 5-5: Eye diagrams of the 5th WDM channel: (a) at back-to-back, (b) after 500 km transmission over DSF without ENLC, (c) after 500 km transmission over DSF with ENLC, (d) after 800 km transmission over DSF with ENLC

The back-to-back electrical eye-diagram of the 5th WDM channel is shown in Figure 5-5(a). The rails on eyes are from linear crosstalk due to small channel spacing. Figure 5-5(b) and (c) show the eye diagrams of the received signals after 500 km transmission over DSF without and with ENLC, respectively. The *Q*-factor of the eye diagram in Figure 5-5(b) is about 6. It is clearly seen that the eye diagram in Figure 5-5(c) are more open because of nonlinearity compensation. Figure 5-5(d) shows the eye diagram ($Q \approx 6$) after 800 km transmission over DSF with ENLC.

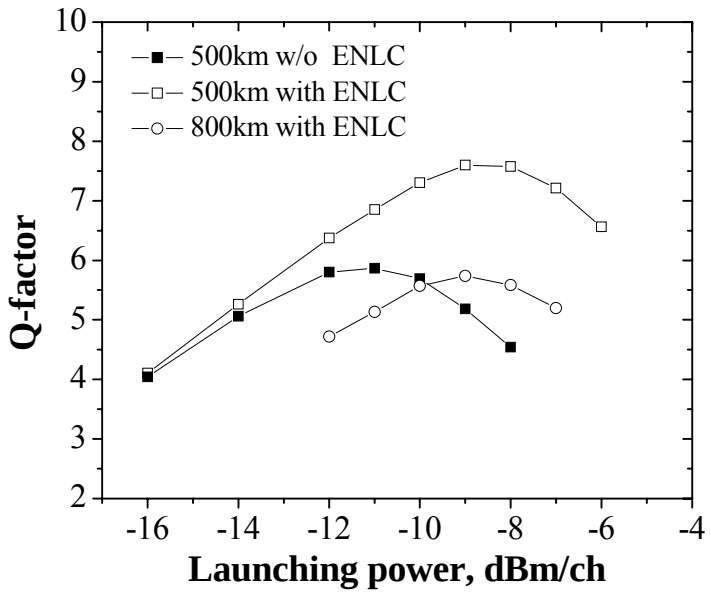

Figure 5-6: Calculated *Q*-factor of the 5th WDM channel vs. the average launching power

Figure 5-6 shows the dependence of the *Q*-factor of the 5th WDM channel on the average launching power. After transmission of 500 km DSF the optimum launching power is increased from -11 dBm to -9 dBm due to nonlinearity compensation. When the launching power is more than -9 dBm, the performance of ENLC is limited by the ASE noise from the optical amplifiers along the fiber chain. After transmission of 800 km DSF and with ENLC, the *Q*-factor is similar to that after 500 km transmission but without ENLC, indicating that the transmission distance with digital nonlinearity compensation is increased by 60%. It is noted that the degradation of the *Q*-factor in long-haul transmission is also from the numerical errors in the backward propagation calculations. The system performance could be further improved by optimizing the FIR filter used for dispersion compensation.

5.5 Discussions and Conclusions

In conclusion, a method for universal digital post-compensation for all fiber impairments in WDM transmission is proposed. Post-compensation is accomplished through backward propagation in the digital domain. The split-step FIR method and a parallel architecture have been designed to facilitate real-time implementation. The numerical simulations indicate that 2 samples per symbol hardware sampling and up-sampling in the digital domain are sufficient to achieve significant nonlinearity compensation. Simulation of WDM transmission in DSF of 10 channel BPSK signals shows a 60% increase in transmission distance using nonlinearity compensation. Similar results for standard single-mode fiber transmission were achieved with FIR filter length 3 times larger than that used for DSF transmission.

The number of required computations is of utmost importance in the eventual realization of the post-compensation method. Taking the parameters used in our simulations for a 10 channel WDM system with a channel spacing of 20 GHz, for 8 transmission spans of 100 km DSF, the required computation and latency are 5.184×10^6 *MACs* and 0.78 μs, respectively. The average number of *MACs* required for each channel is 5.184×10^5. It should be noted that this overall computation and latency is realized using fixed step size. It is expected that employing variable step size [15] would reduce the number of operations by a factor of 4-5, bringing the average required *MACs* and processing speed per channel to within about one order of magnitude of the state of art field-programmable gate arrays (FPGAs). Block processing of the incoming

samples coupled with fast Fourier transform implementation allows dispersion compensation in the frequency domain [16]. This may lead to further decrease in the number of operations and better compensation at longer transmission distances. Furthermore, when high-order modulation formats such as QAM with multi-bit/symbol spectral efficiency are used, the required *MACs* per symbol should remain about the same and thus the required *MACs* per bit should decrease proportionally with spectral efficiency. The channel spacing can be further reduced to be equal to the symbol rate using the orthogonal WDM approach that we have demonstrated recently [17]. The combination of high spectral efficiency and narrow channel spacing can potentially reduce the number of operations per bit by another order of magnitude.

In the simulation, the phases of the LOs in coherent detection are assumed to be locked to each other. While this requirement is necessary for pre-compensation schemes, it is not absolutely necessary for post-compensation. The relative phase drift between the LOs can be monitored and factored into post-compensation using heterodyning between the LOs. Parallel polarization of the WDM channels along the entire link has been assumed in the simulations for simplicity. Due to its random nature, polarization mode dispersion (PMD) will be another limiting factor on the effectiveness of ENLC; however, this would only occur in high-symbol rate (e.g. 40 G symbol/s) systems.

5.6 References

[1] A. M. Vengsarkar and W. A. Reed, "Dispersion-compensating single mode fiber: Efficient designs for first- and second-order compensation," *Opt. Lett.*, vol.18, pp.924-926, 1993.

[2] C. Kurtzke, "Suppression of fiber nonlinearities by appropriate dispersion management," *IEEE Photon. Technol. Lett.*, vol.5, pp.1250-1253, 1993.

[3] K. Nakajima *et al.*, "Design of dispersion managed fiber and its FWM suppression performance," *OFC'1999,* paper ThG3, 1999.

[4] X. Liu *et al.*, "Improving transmission performance in differential phase-shift-keyed systems by use of lumped nonlinear phase-shift compensation," *Opt. Lett.*, vol.27, pp.1616-1618, 2002.

[5] S. Watanabe and M. Shirasaki, "Exact compensation for both chromatic dispersion and Kerr effect in a transmission fiber using optical phase conjugation," *IEEE J. Lightwave Technol.*, vol.14, pp.243-248, 1996.

[6] R. I. Killey *et al.*, "Electronic dispersion compensation by signal predistortion using digital processing and a dual-drive Mach-Zehnder modulator," *IEEE Photon. Technol. Lett.*, vol.17, pp.714-716, 2005 .

[7] S. L. Woodward *et al.*, "Demonstration of an electronic dispersion compensation in a 100-km 10-Gb/s ring network," *IEEE Photon. Technol. Lett.*, vol.15, pp.867-869, 2003.

[8] K. Roberts *et al.*, "Electronic precompensation of optical nonlinearity," *IEEE Photon. Technol. Lett.*, vol.18, pp.403-405, 2006.

[9] E. Yamazaki *et al.*, "Compensation of interchannel crosstalk induced by optical fiber nonlinearity in carrier phase-locked WDM system," *IEEE Photon. Technol. Lett.*, vol.19, pp.9-11, 2007.

[10] M. G. Taylor, "Coherent detection method using DSP for demodulation of signal and subsequent equalization of propagation impairments," *IEEE Photon. Technol. Lett.*, vol.16, pp.674-676, 2004.

[11] K. Kikuchi, "Phase-diversity homodyne detection of multilevel optical modulation with digital carrier phase estimation," *IEEE J. Sel. Topics Quantum Electron.*, vol.12, pp.563-570, 2006.

[12] G. P. Agrawal, *Nonlinear Fiber Optics*, Academic, 2001.

[13] X. Li *et al.*, "A broad-band digital filtering approach for time-domain simulation of pulse propagation in optical fiber," *IEEE J. Lightwave Technol.*, vol.23, pp.864-875, 2005.

[14] R. Noé, "Phase noise tolerant synchronous QPSK receiver concept with digital I&Q baseband processing," in *Proceedings of Opto-Electronics and Communications Conf.*, pp.818-819, 2004.

[15] O. V. Sinkin *et al.*, "Optimization of the step-size fourier method in modeling optical-fiber communications systems," *IEEE J. Lightwave Technol.*, vol.21, pp.61-68, 2003.

[16]H. Sari *et al.*, “Frequency domain equalization of mobile radio and terrestrial broadcast channels,” in *Proceedings of IEEE Global Telecomm. Conf.*, pp.1-5, 1994.

[17]G. Goldfarb *et al.*, “Orthogonal wavelength-division multiplexing using coherent detection,” *IEEE Photon. Technol. Lett.*, vol.19, pp.2015-2017, 2007.

6. ELECTRONIC JOINT SOA AND FIBER IMPAIRMENT COMPENSATION

6.1 Introduction

In transmission systems using SOAs for optical amplification, high signal (launching) power is required to counter the rapid degradation of the SNR at the receiver due to the ASE noise of SOAs along the link. However SOAs will be operated in the saturation region and the signals will suffer from SOA impairments including the data pattern effect, SGM, SPM, and inter-channel crosstalk effects such as XGM and FWM through SOAs in WDM. In addition, the signals will also be distorted by fiber impairments such as chromatic dispersion and Kerr nonlinear effect. In order to maximize the SNR of the received signals while maintaining systems performance, both SOA and fiber impairments need to be compensated.

In Chapter 4 and 5, SOA impairment compensation (IC) and fiber IC are proposed and demonstrated, respectively. Both of them are based on digital backward propagation method. It is noted that only direct detection is used and SOA IC is implemented in the transmission experiment of OOK signal in Chapter 4. This is because 1) OOK signal is intensity-modulated and thus signal phase is not required for detection; 2) The SSMF has negligible dispersion around 1310 nm and consequently the intensity or waveform of OOK signal is not distorted by

fiber. However, for advanced modulation formats involve phase modulation or in transmission windows with large fiber dispersion, coherent detection must be used and fiber impairments need to be compensated as well. Due to the common nature of backward propagation in SOA and fiber ICs, an electronic post-compensation scheme for joint SOA and fiber impairments is proposed in this chapter. A transmission experiment of both amplitude- and phase-modulated signal with joint SOA and fiber ICs is demonstrated using coherent detection and off-line processing.

6.2 Principle of Joint SOA and Fiber Impairment Compensation

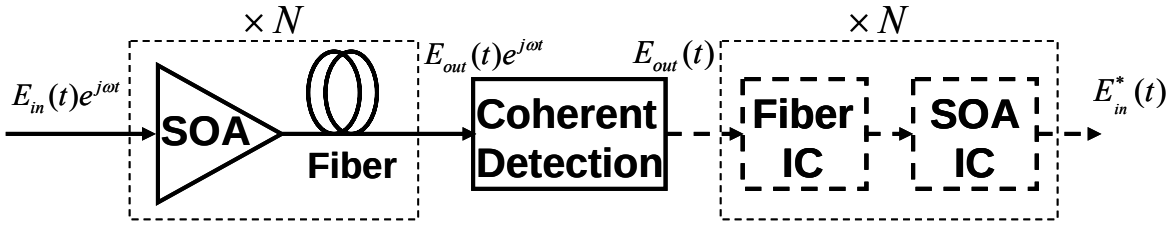

Figure 6-1: Fiber-optic transmission using SOAs and electronic post-compensation of SOA and fiber impairments

Figure 6-1 shows the schematic diagram of an N span fiber-optic transmission system using SOAs and electronic fiber and SOA ICs. At the end of the transmission link, the received optical signal $E_{out}(t)e^{j\omega t}$ is first converted to the base-band signal $E_{out}(t)$ by coherent detection then fiber IC and SOA IC are implemented in electrical domain in the reverse order to the their forward propagation. Both SOA IC and fiber IC are based on backward propagation method as

described in Chapter 4 and Chapter 5, respectively. The *NLSE* governing the backward propagation in each fiber IC can be written by [5]

$$\frac{\partial A}{\partial z}+\frac{i\beta_2^{'}}{2}\frac{\partial^2 A}{\partial t^2}-\frac{\beta_3^{'}}{6}\frac{\partial^3 A}{\partial t^3}+\frac{\alpha^{'}}{2}A=i\gamma^{'}\left|A\right|^2 A \tag{6-1}$$

where $A(z,t)$ is the electrical field of the optical signal, $\gamma^{'}$, $\beta_2^{'}$, $\beta_3^{'}$ and $\alpha^{'}$ are the nonlinear, first- and second-order chromatic dispersion, and loss coefficient that have exactly the negative of the values for the real transmission fiber. Equation 6-1 can be solved numerically using split-step Fourier method or split-step FIR method. Assuming the electrical field of the output signal of the fiber IC and the input signal of the SOA IC is $A_{in}(t)$, the dynamic equation for backward propagation in the SOA IC can be described by

$$\left(1+\tau_c\frac{d}{dt}\right)h^{'}(t)=h_0^{'}-\frac{P_{in}(t)}{P_{sat}}\left(\exp[h^{'}(t)]-1\right) \tag{6-2}$$

where $P_{in}(t)=\left|A_{in}(t)\right|^2$, $h^{'}(t)=-\ln G(t)$, $h_0^{'}=-\ln G_0$. $G(t)$ and G_0 are the time-dependent gain and the small signal gain of the physical SOA to be compensated, respectively. The minus signs ensure that the linear and nonlinear effects are reverse to those in the SOA, leading to impairment compensation. P_{sat} is the saturation power of the SOA and τ_c is the average carrier lifetime, which is dependent on the average input signal power. Solving Equation 6-2, the electrical field of the output signal of SOA IC $A_{out}(t)$ can be expressed by

$$A_{out}(t) = A_{in}(t) \cdot \exp\left[\frac{(1 - i\alpha_H)h'(t)}{2}\right] \tag{6-3}$$

where α_H is the linewidth enhancement factor or chirp factor of the SOA.

6.3 Transmission Experiment of APSK signal with SOA and Fiber IC

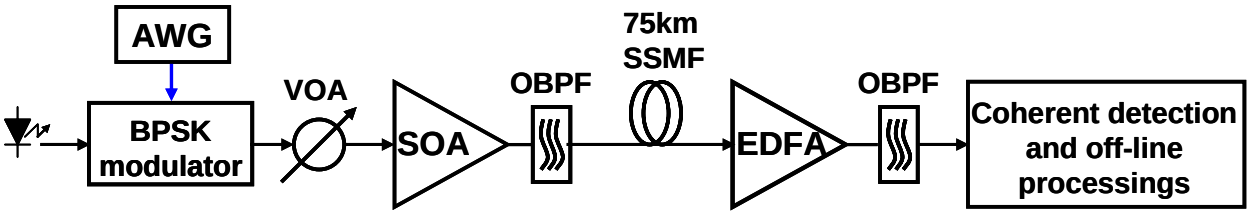

Figure 6-2: Experimental setup of 4-APSK transmission with joint SOA and fiber impairment compensation. AWG: arbitrary waveform generator; VOA: variable optical attenuator; OBPF: optical band-pass filter; SSMF: standard single-mode fiber

Figure 6-2 shows the experimental setup for a four-level amplitude and phase-shift keying (4-APSK) transmission experiment over 75 km standard single-mode fiber (SSMF). A 2.5 Gbaud/s optical 4-APSK signal was generated by externally modulating a 1550 nm DFB laser with a 4-APSK electrical signal from an arbitrary waveform generator. The binary phase-shift keying (BPSK) modulator was biased as null point and the electrical signal has a V_{pp} of ~ $2V_{\pi}$. The 4-APSK optical signal has two amplitude levels (1, 3) and two phase levels (0, π). A 1550 nm low-tensile-strained bulk SOA worked as a power booster, followed by an optical band-pass filter (OBPF) to remove the ASE noise. At the injection current of 120 mA, the SOA had a small

signal gain of 23.5 dB and 3-dB saturation output power of 4.0 dBm. The OBPF had a 3-dB bandwidth of 1 nm and insertion loss of 1.4 dB. A variable optical attenuator was used to control the power into the SOA which is also the launching power into fiber. The measured loss of the 75 km SSMF was 17.7 dB. An EDFA worked in power mode as a preamplifier, followed by another 1-nm OBPF to remove the extra ASE noise before coherent detection. The coherent receiver consists of an optical local oscillator, a 90 degree optical hybrid, photodetectors, and electrical preamplifiers. At different input powers to the SOA, both in-phase and quadrature components of the received optical signals were sampled and recorded at 20 GSa/s or 8 Sa/Symbol by a real-time sampling oscilloscope after coherent detection. The signal powers at the output of the SOA and end of the fiber were measured respectively by an optical power meter.

The fiber and SOA ICs were finally implemented off-line in the software domain. In the reverse order to the forward transmission, the fiber IC was first implemented by solving Equation 6-1 numerically using the split-step Fourier method. Then the SOA IC was implemented by solving Equation 6-2 numerically using the 4^{th} order Runge-Kutta method. At each input power to SOA, both carrier lifetimes and chirp factor of the SOA were optimized through global search by maximizing the Q-factor of the signals after clock recovery and phase estimation.

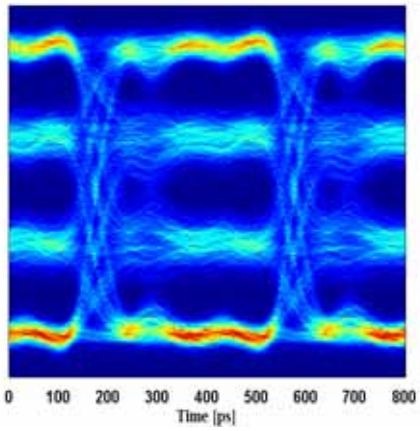

(a)

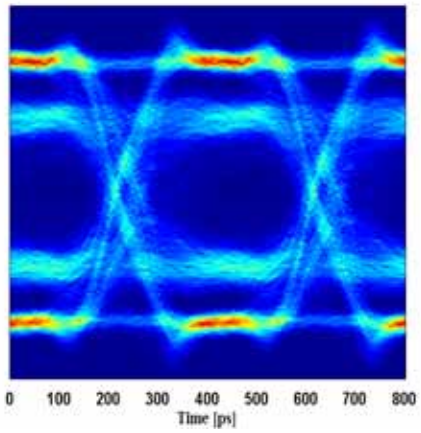

(b)

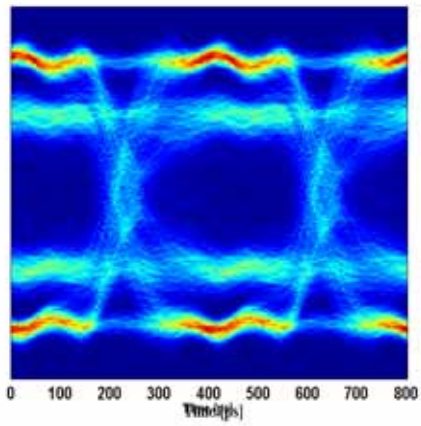

(c)

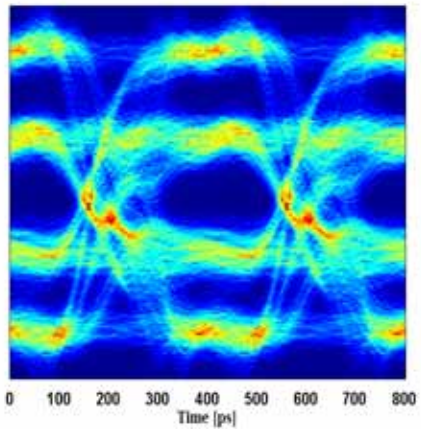

(d)

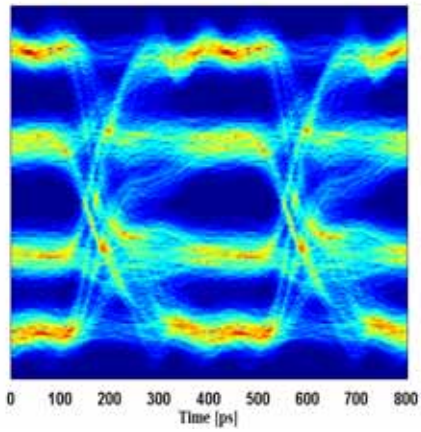

(e)

Figure 6-3: Eye diagram of the 4-APSK signal a) at back-to-back; b) after SOA and 75 km SSMF without fiber and SOA ICs; after SOA and 75 km SSMF c) with only fiber IC; d) with only SOA IC; e) with both fiber and SOA ICs

Figure 6-3(a) shows the eye diagram of the back-to-back 4-APSK signal after coherent detection and phase estimation. More significant amplitude fluctuations can be observed on the two levels in the middle due to the larger modulation slope of the BPSK modulator. The calculated Q-factor (average of the Q-factors of the three eyes) is 11.5 dB. Figure 6-3(b) shows the eye diagram of the received signal without impairment compensation when the input power to SOA is -18 dBm and the launching power into SSMF is 1.8 dBm. Two eye openings were compressed relative to the middle eye due to SOA gain saturation. The eye diagram of the received signal after fiber IC is shown in Figure 6-3(c). No significant improvement was observed from fiber IC compared to the signal in Figure 6-3(b) due to the small fiber dispersion (~24 ps) compared to the symbol period (400 ps) and the negligible fiber nonlinearity compared to the SOA nonlinearity. However fiber IC is still necessary before SOA IC. Figure 6-3(d) shows the eye-diagram of the received signal with only SOA IC with the calculated Q-factor of 10.1 dB. With both fiber and SOA ICs, the calculated Q-factor was increased to 10.8 dB and four amplitude levels are clearly seen in Figure 6-3(e).

The dependence of the calculated Q-factor of the 4-APSK signal after fiber and SOA ICs on the input power to the SOA is shown in Figure 6-4(a). The signals suffer from ASE noise of SOA at low input powers and fiber and SOA nonlinearities at high input powers, respectively. The optimum power into SOA is -18 dBm with the Q-factor of 10.8 dB. Compared to the Q-factor of the signal at back-to-back (11.5 dB), the 0.7 dB penalty is due to the presence of the accumulated ASE noise in the received signals, which can not be compensated. Figure 6-4(b)

shows the optimized carrier lifetimes and chirp factors used for SOA IC in Equation 6-2 and 6-3 at different input powers. It is noted that all the optimized carrier lifetimes and chirp factors are in the range of 80 ps − 200 ps and 4 − 7, respectively, which are the typical numbers of the conventional bulk SOAs.

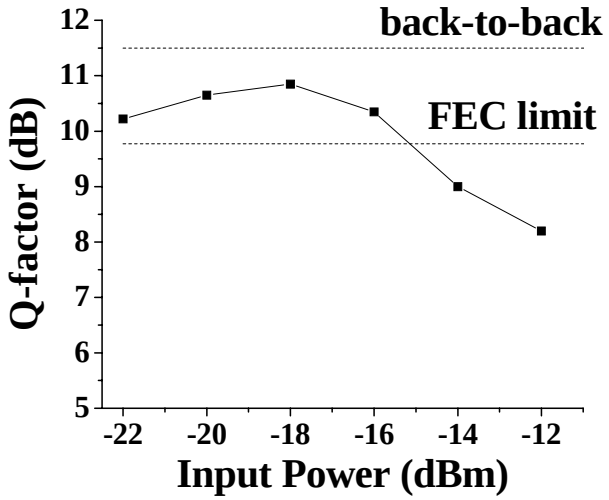

(a)

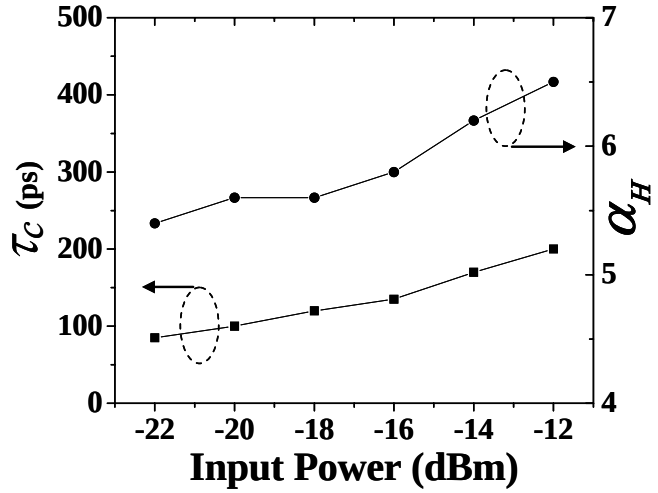

(b)

Figure 6-4: a) Q-factor and b) optimized τ_c and α_H vs. input power to SOA

7. FUTURE WORK

7.1 WDM Transmission with Joint SOA and Fiber IC

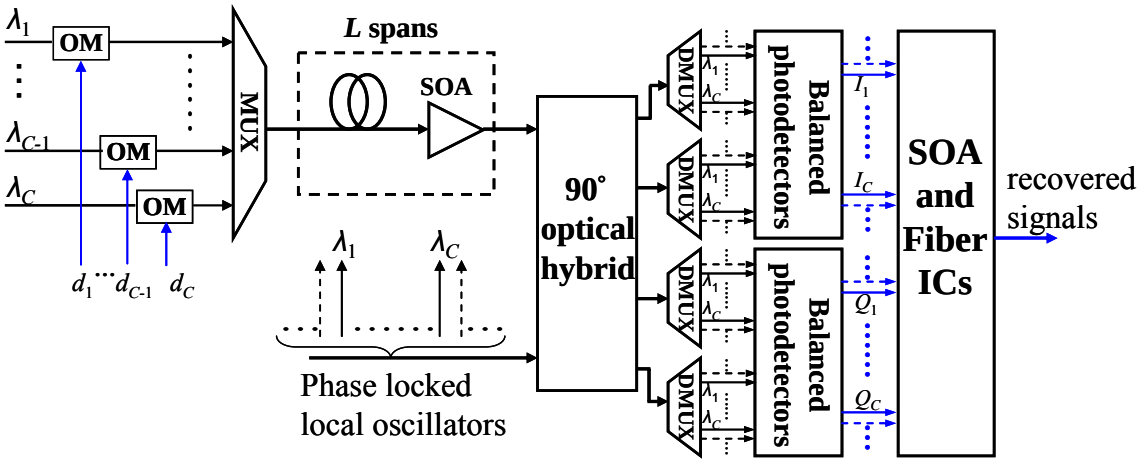

Figure 7-1: WDM transmission with joint SOA and fiber IC. OM: optical modulator; Optical path: black line; Electrical path: blue line

Figure 7-1 shows a WDM transmission system using SOAs and with joint SOA and fiber IC. It is noted here that the full rate equation model for SOAs and the coupled wave equations need to be used for SOA IC in WDM system and the full knowledge of the exact bit sequences of the WDM channels is required to compensate inter-channel effects such as XGM and FWM through SOAs. The effectiveness of the joint SOA and fiber IC will be investigated by numerical simulations in the future.

7.2 Parallel DSP Implementation of SOA IC

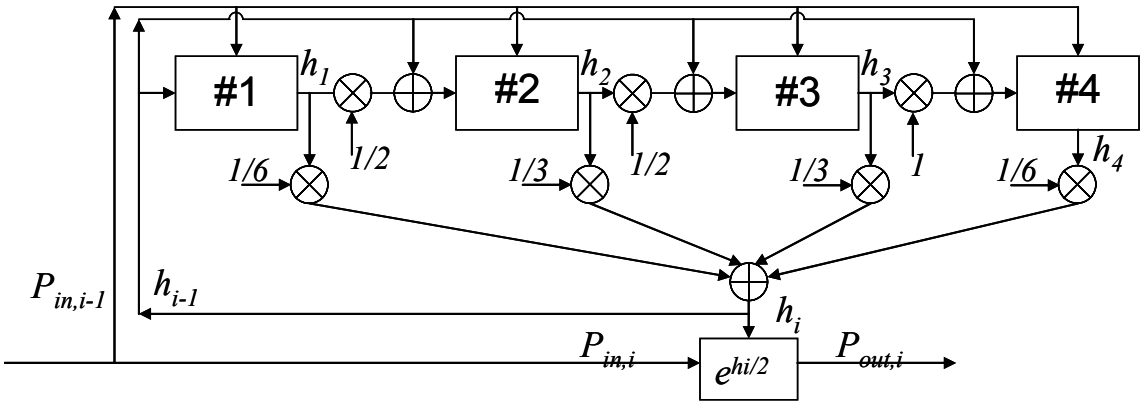

Figure 7-2: The function diagram of the 4th order Runge-Kutta method for SOA IC

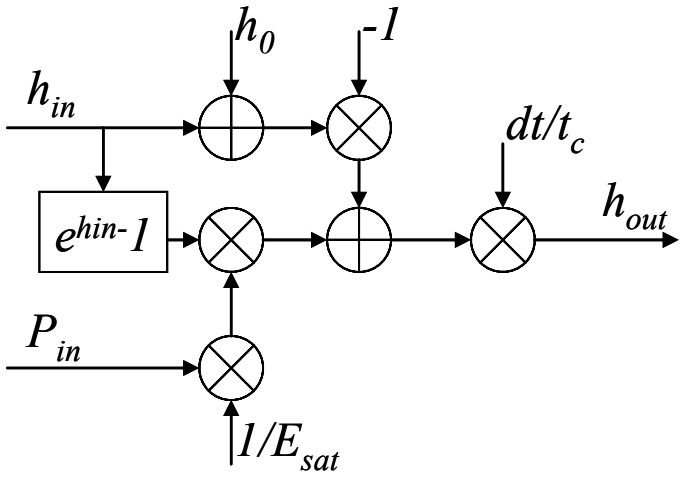

Figure 7-3: The function diagram of #1…#4 in Figure 7-2

Figure 7-2 and 7-3 show the implementations of the 4th order Runge-Kutta (R-K) method used for SOA IC from the function's point of view. On one hand, SOA IC can be decomposed into basic multiplications, summations and exponential calculations and thus implemented in digital

domain accordingly using DSP in application-specific integrated circuit (ASIC) chips with *MAC* units and lookup tables. On the other hand, the sampling rate and processing speed of the DSP in the experiments are assumed to be 40 GSa/s to assure effective SOA IC of the 10 GSym/s signal. However, the 4^{th} order R-K method is based on the sequential computations. In order to relax the requirement for the processing speed, parallel implementations of the SOA IC or the 4^{th} order R-K method need to be investigated.